



Ben-Gurion University of the Negev  
The Department of Geological and Environmental Sciences

**Estimation of Historical Seismic Ground-Motions  
Using Back Analysis of Structural Failures in  
Archaeological Sites**

Thesis Submitted in Partial Fulfillment of the Requirements for the M.Sc Degree in  
the Faculty of Natural Sciences

**By Ronnie Kamai**

April 24, 2006

כ"ו בניסן, תשס"ו

## **Abstract**

This thesis presents a new method for seismic risk evaluation, in which earthquake-induced structural failures in archaeological sites are back-analyzed using analytical and numerical solutions.

Both pseudo-static and fully dynamic analyses were performed after an accurate block system was generated with adequate boundary conditions and material properties. The generated block system was subjected to either pseudo-static inertia forces or dynamic loading functions, as direct input. The response of the structures was studied up to the point of incipient failure, in a mechanism similar to the one observed in the field.

The dynamic analyses were performed using the numerical 2D-Discontinuous Deformation Analysis (2D-DDA) (Shi, 1993), a state of the art method in terms of development and application, among the implicit DEM methods (Jing, 2003). The DDA method was validated with respect to analytical solutions for various problems and was proven accurate. Two validations were performed in this study for calibration purposes: 1) The well studied case of a block on an inclined plane (MacLaughlin and Doolin, 2005) was re-studied and a much greater accuracy was obtained for the dynamic case with respect to previous publications, and 2) The dynamic displacement of the foundation of a structure was simulated by inducing time-dependant displacements into the foundation block and studying the response of the overlying block. DDA results were found to be sensitive mainly to interface friction and to the dynamic parameters of the loading function (amplitude and frequency).

Three archaeological sites in Israel were investigated using the new method, and results were presented in terms of displacement evolution of selected structural elements in the studied masonry structure.

While pseudo-static results were found irrelevant and highly un-satisfactory, sensitivity analyses of numerical results provided quantitative constraints on historical ground-motion parameters in

## Abstract

the studied sites; in all three sites the failure that was observed in the field was duplicated very successfully by 2-D DDA. The obtained values for acceleration amplitude, although higher than expected by Israel building code #413 (Shapira, 2002), are within the order of 0.5 - 1g, well within reason for very strong earthquakes that destroyed the three ancient towns.

Finally, it is shown that individual block displacement data as well as the general deformed mesh configuration provide important insight into the evolution of structural damage with time, and the over-all response of masonry structures to earthquake-induced shaking.

## **Acknowledgements**

Prof. Yossi Hatzor is thanked for his much appreciated mentoring, personal involvement, and unlimited support throughout the way.

Dr. Shmulik Marco is thanked for his supervision and thoughtful remarks.

Prof. Yehuda Eyal and Dr. Itai Leviathan are thanked for critical review of the thesis.

Dr. Avner A. Arzi, Prof. Oren Vilnay and Dr. Itai Leviathan are thanked for suggestions and stimulating discussions.

Dr. Gen-hua Shi is thanked for providing us with his latest version of DDA (2003). Dr. Yuli Zaslavsky from the Geophysical Institute of Israel is thanked for providing us with the deconvoluted displacement record of the Nuweiba 1995 earthquake. Dr. Tsvika Tsuk from Israel Nature and Parks Authority and Dr. Tali Gini of Israel Authority of Antiquities are thanked for supervising block sampling and measurements in the field.

Finally I thank my husband, Tamir, for always having an enlightening suggestion, remark, or idea to inspire me.

## Table of Contents

<b>Abstract</b> .....	1
<b>Acknowledgements</b> .....	3
<b>1 Introduction</b> .....	12
1.1 Seismic Hazard .....	12
1.2 Paleoseismology .....	13
1.3 Research Objectives.....	16
<b>2 Theoretical Background</b> .....	18
2.1 Analytical Solutions.....	18
2.1.1 Block on a plane – pseudo static solution.....	18
2.1.2 Block on an incline – dynamic solution.....	21
2.1.3 Block response to induced displacements in the foundation – dynamic solution.....	23
2.1.4 The masonry arch.....	25
2.2 Numerical Solutions.....	32
2.2.1 Background.....	32
2.2.2 Basic concepts of DDA.....	34
<b>3 Experimental</b> .....	39
3.1 Mechanical properties of intact rocks.....	39
3.2 Shear strength of interfaces.....	40
3.3 Summary.....	44
<b>4 DDA validation</b> .....	45
4.1 Block on an Incline .....	45
4.1.1 Gravitation only .....	45
4.1.2 Dynamic loading.....	47
4.2 Block response to induced displacements in the foundation .....	51
4.3 Summary and Conclusions: .....	56
<b>5 Case studies</b> .....	58
5.1 Masonry Arch - results from Mamshit.....	58
5.1.1 Background.....	58
5.1.2 Analytical solution.....	60
5.1.3 Numerical solution.....	63
5.1.4 Summary.....	76
5.2 A block sliding on a plane - results from Avdat.....	78

5.2.1	Background.....	78
5.2.2	Analytical solution.....	81
5.2.3	Numerical solution.....	83
5.2.4	Summary.....	91
5.3	Masonry arch – results from Nimrod Fortress.....	92
5.3.1	Background.....	92
5.3.2	Numerical solution.....	95
5.3.3	Summary.....	106
<b>6</b>	<b>Discussion and Conclusions</b> .....	<b>108</b>
6.1	Discussion - seismological implications of results.....	108
6.2	Limitations and advantages of the new method.....	113
6.2.1	Limitations.....	113
6.2.2	Advantages.....	114
6.3	Site – Specific conclusions:.....	115
6.3.1	Mamshit.....	115
6.3.2	Avdat.....	116
6.3.3	Nimrod Fortress.....	116
6.4	Pseudo-Static vs. Dynamic Analysis.....	117
6.5	Recommendations for further research.....	118
	<b>Appendixes</b> .....	<b>120</b>
	Appendix 1 – Matlab model for validation of induced displacement.....	120
	Appendix 2.1 – Mapping of the structure at Mamshit.....	121
	Appendix 2.2 – Mapping of the structure at Avdat.....	122
	Appendix 2.3 – Mapping of the structure at Nimrod Fortress.....	123
	Appendix 3.1 – DDA runs for Mamshit.....	124
	Appendix 3.2 – DDA runs for Avdat.....	126
	Appendix 3.3 – DDA runs for Nimrod Fortress.....	128
	<b>References</b> .....	<b>130</b>

## Table of Figures

Figure 1.1. The seismic risk map of Israel. The map presents the seismic coefficient $Z$ as predicted by Israel building code #413. $Z$ is the expected Horizontal Peak Ground Acceleration (H-PGA) with a 10% probability for occurring at least once in 50 years. (Shapira, 2002).....	14
Figure 1.2. Location map of studied sites. The three investigated sites – Avdat, Mamshit, and Nimrod fortress are marked, and their vicinity to the DST can be seen. ....	17
Figure 2.1. Schematic presentation of the forces acting on a block in a masonry wall. The shaded block is analyzed, $T_1$ and $T_2$ are the frictional forces resisting to the sliding movement, and $F$ is the driving force.....	19
Figure 2.2. An example of the displacement-based solution, also known as “Newmark type” solution. The displacement in the lower figure results from the double integration of the acceleration function in the upper figure between $t_1$ and $t_2$ - beyond the yield acceleration ( $k_y$ in this figure) (Goodman and Seed, 1966).....	21
Figure 2.3. Schematic presentation of the forces acting on a single block lying on an incline. The activating force is a horizontal time-based sinusoidal acceleration. The resisting frictional force is constant; the friction angle does not change after motion begins. ....	22
Figure 2.4. Schematic presentation of the case of an upper block (2), lying on the foundation block (1) which is subjected to a dynamic displacement input function. ....	23
Figure 2.5. Structural terms for the masonry arch .....	25
Figure 2.6. The thrust line :(a) The thrust line is comfortably contained within the arch, (b) The thinnest possible arch, in which the thrust line touches the edge at 5 points, (c) The arch is on the point of collapse, by formation of 5 hinges, where the thrust line touched the edge in 2.6.b. (Heyman, 1982) .....	27
Figure 2.7. A semicircular arch with: (a) The least possible value for abutment thrust, $H_{min}$ (b) The greatest possible value for abutment thrust, $H_{max}$ . (Heyman, 1982).....	28
Figure 2.8. Lower horizontal limit thrust (Blasi and Foraboschi, 1994) .....	29
Figure 2.9. Upper horizontal limit thrust (Blasi and Foraboschi, 1994).....	30
Figure 3.1. <b>A.</b> Ultra-sonic wave test device at RMLN, BGU, used to obtain dynamic elastic parameters <b>B.</b> Point load test, used to obtain the uniaxial compressive strength of the material. ....	40
Figure 3.2. <b>A.</b> The servo-controlled direct shear system, the sample is ready to enter the load frame, <b>B.</b> A sample from Avdat after a test, the surface roughness is noticed by the white points, first to be sheared.....	41

Figure 3.3. Results for a direct shear test on a sample from Avdat, under three different normal stresses. ....	42
Figure 3.4. Results of the direct-shear tests on the Avdat samples, shear stress plotted versus normal stress. Even though the true behavior of the failure envelopes is not necessarily linear, a linear trend yields the following results: $\mu=0.57$ , $\phi=30^\circ$ for the peak shear strength and $\mu=0.53$ , $\phi=28^\circ$ for the residual strength. ....	42
Figure 3.5. Results for a direct shear test on a sample from Mamshit, under three different normal stresses. ....	43
Figure 3.6. Results of the direct-shear tests on the Mamshit samples, dynamic friction coefficient plotted versus normal stress. ....	43
Figure 4.1. The model used for DDA validation of a block sliding on an incline.....	46
Figure 4.2. Block displacement vs. time for the case of a block on an incline – gravitational loading only. Comparison between analytical (lines) and DDA (symbols) solutions.....	47
Figure 4.3. The model used in DDA for the dynamic validation of a block sliding on an incline. The driving forces act directly on the sliding block; the inclined block is fixed in place. ....	49
Figure 4.4. The input acceleration function used for the dynamic validation of a block sliding on an incline. $A=0.5$ , $f=1/\pi$ . ....	49
Figure 4.5. Block displacement versus time, for the dynamic case of a block on an incline, $\alpha=\phi=20$ . Comparison between analytical (solid line) and DDA (symbols) solutions.....	50
Figure 4.6. Block displacement versus time, for the dynamic case of a block on an incline, $\alpha<\phi$ . Comparison between analytical (solid line) and DDA (symbols) solutions.....	50
Figure 4.7. The input displacement function used for the dynamic validation of a block on a displaced block. $D=0.5$ , $f=1$ . ....	52
Figure 4.8. Three DDA block systems, examined for mode of failure. The number of the block is indicated on its right side. Model 3, with block 2 being the most slender, was found to obtain best agreement with the analytical solution. ....	53
Figure 4.9. Response of Block 2 to displacement input of $D=0.5\text{m}$ , $f=1\text{Hz}$ . Comparison between three DDA models (model 1 as triangles, model 2 as circles, and model 3 as rectangles), and two sets of numerical parameters (empty symbols – $g_1=0.0075$ , $g_2=0.002$ . full symbols – $g_1=0.025$ , $g_2=0.005$ ). ....	53
Figure 4.10. Response of Block 2 to displacement input of $f=1\text{Hz}$ . Comparison between analytical (line) and DDA (symbols) solutions for different amplitudes of motion. ....	54

Figure 4.11. Response of Block 2 to displacement input of $D=0.02\text{m}$ . Comparison between analytical (line) and DDA (symbols) solutions for different frequencies of motion. ....	55
Figure 4.12. Response of Block 2 to displacement input of $D=0.5\text{m}$ , $f=1\text{Hz}$ . Comparison between analytical (line) and DDA (symbols) solutions for different friction coefficients.....	56
Figure 5.1. General plan of the city of Mamshit (Negev, 1988a). The black arrow points to building IX. ....	59
Figure 5.2. Detailed map of the eastern church (Negev, 1988a). The black arrow points to the location of the deformed arch in building IX.....	59
Figure 5.3. The deformed arch at Mamshit. <b>A.</b> The arch is embedded in a very heterogenic wall. <b>B.</b> The Keystone has slid 4cm downwards while the rest of the arch remained intact. ....	60
Figure 5.4. $H_{\min}$ versus $\theta$ . The maximum point is the minimum horizontal thrust at stability, and the associated angle of the hinge at the haunch for the lower collapse mechanism. ....	62
Figure 5.5. $H_{\max}$ versus $\theta$ . The minimum point is the maximum horizontal thrust at stability, and the associated angle of the hinge at the haunch for the upper collapse mechanism. ....	62
Figure 5.6. The DDA model for the free standing arch. Measurement, loading and fixed points assigned to the mesh are marked. ....	63
Figure 5.7. Simulation results for the free standing arch. <b>A.</b> $f=1\text{Hz}$ , $D=0.013\text{m}$ (equivalent to 0.05g). Keystone slides down 4.7cm after 4.5sec, adjacent stones remain in place. <b>B.</b> $f=2.5\text{Hz}$ , $D=0.005\text{m}$ (equivalent to 0.126g). Keystone slides down 4.5cm after 2.5sec. adjacent stones undergo downward sliding of up to 1cm. Points a, b, and c are an open hinge- outwards as in a and b, or inwards as in c.....	65
Figure 5.8. The first mesh configuration for the heterogeneous wall of the embedded arch; a combination of a statistical net with manually-inserted lines. <b>A.</b> A 10 meters wide, 3 meters high block system. <b>B.</b> After 10 seconds, vertical joints open. <b>C.</b> A 10 meters wide, 5 meters high block system. <b>D.</b> After 10 seconds, vertical joints open, and the arch is distorted.....	67
Figure 5.9. <b>A.</b> Simulation of the surrounding heterogeneous wall as one soft block, $E=1\text{MPa}$ . <b>B.</b> After 2 seconds, the surrounding block extends and the arch remains intact. <b>C.</b> A statistical net with bigger and softer blocks. <b>D.</b> After 2 seconds, the wall disassembles. ....	68
Figure 5.10. The final mesh configuration for the embedded arch. The uniform masonry wall rests on two blocks: the lower is fixed by assignment of three fixed points (squares), and the overlying block can be subjected to time-dependant displacements. The height of the wall above the arch is $h$ . the lines intersecting the arch blocks represent material lines, and a measurement point (circle) is assigned at the keystone.....	68

Figure 5.11. Keystone vertical displacement vs. time - influence of loading mechanism. $A=0.32g$ ( $D=8cm$ ), $f=1Hz$ .....	69
Figure 5.12. Response of the Mamshit block system to an earthquake with $A=0.32g$ ( $D=8cm$ ), $f=1Hz$ . A. displacement mode B. quake mode.....	70
Figure 5.13. The Nuweiba 1995 record, after de-convolution to rock response. The red rectangle marks the 10 seconds that were used for the analysis of the Mamshit block system, 15-25 sec.	71
Figure 5.14. A synthetic sinusoidal acceleration record, used for analysis on the Mamshit block system. $A=0.5g$ , $f=1Hz$ .....	71
Figure 5.15. Keystone vertical displacement vs. time - influence of overburden ( $h$ ). $A=0.5g$ , $f=1.5Hz$ . .....	72
Figure 5.16. Keystone vertical displacement vs. time - influence of wall stiffness. $E_{arch}=17GPa$ , $A=0.5g$ , $f=1.5Hz$ .....	72
Figure 5.17. Keystone vertical displacement vs. time - influence of numerical damping ( $k01$ ). $A=0.5g$ , $f=1.5Hz$ . Zero damping is not presented, since it resulted in complete destruction of the block system.....	73
Figure 5.18. Keystone vertical displacement vs. time - influence of amplitude. $f=1Hz$ .....	74
Figure 5.19. Keystone vertical displacement vs. time - influence of frequency. $A=0.5g$ .....	75
Figure 5.20. The result of the dynamic block system response under an earthquake with $A=0.5g$ and $f=1Hz$ . The accumulating downwards displacement of the keystone is 3.11 cm. ....	77
Figure 5.21. A sketch-plan of the city of Avdat, after Woolley and Lawrence, 1914 (Negev, 1997), The black arrow at the top points at the southern Roman tower. ....	80
Figure 5.22. The Roman tower in Avdat, a view of the western wall. The displaced blocks are numbered for reference. ....	80
Figure 5.23. The displaced blocks, two additional points of view. Block numbers refer to Figure 5.22.....	81
Figure 5.24. A schematic presentation of the 5 block case: six frictional surfaces (marked as $S_i$ ) are formed by the stepped shape of the composed block. The North-South dimension of the block is marked as $L_i$ and the East-West dimension is $d_i$ . The weight on the frictional surfaces is calculated from the column of rock mass above the surface. ....	82
Figure 5.25. The northern wall of the roman tower at Avdat. The five corner blocks are marked and their displacement direction is displayed with an arrow.....	83
Figure 5.26. The DDA block system for the tower at Avdat. Five fixed points (squares) are assigned to the confining block, and five measurement points (circles) are assigned corner blocks. Points $b$ , $c$ and $d$ are blocks 1,2 and 3 respectively.....	84

Figure 5.27. A simulation without a confining wall predicts the exact height of displaced blocks as is observed in the field. The graphical output implies that preferred displacement will occur at the doorway level.  $A=1.5g, f=5\text{Hz}$ . ..... 85

Figure 5.28. Horizontal displacement of all 5 measurement points, point *a* being the lower one and point4 the upper one, points *b, c* and *d* correlate to blocks 1, 2 and 3 from Figure 5.22.  $D_{h\_av}$  is the average horizontal displacement of the five measurement points.  $A=1g, f=3\text{Hz}$ ..... 86

Figure 5.29. Average horizontal displacement ( $D_h$ ) of the five measurement points vs. time - influence of amplitude.  $f= 2\text{Hz}$ . ..... 86

Figure 5.30. Average horizontal displacement ( $D_h$ ) of the five measurement points vs. time - influence of amplitude.  $f= 5\text{Hz}$ . ..... 87

Figure 5.31. Average horizontal displacement ( $D_h$ ) of the five measurement points vs. time - influence of additional vertical acceleration.  $A_h=1g, f=5\text{Hz}$ . ..... 88

Figure 5.32. Average horizontal displacement ( $D_h$ ) of the five measurement points vs. time - influence of frequency.  $A = 1g$ ..... 88

Figure 5.33. Graphical output of a simulation with  $A_h= 1g, A_v=0, f=3\text{Hz}$ .  $D_{h\_av_{max}}=8\text{cm}$ . ..... 90

Figure 5.34. Graphical output of a simulation with  $A_h=1.5g, A_v=0, f= 5\text{Hz}$ .  $D_{h\_av_{max}}=14\text{cm}$ . ..... 90

Figure 5.35. General plan of the Nimrod fortress (Hartal, 2001). ..... 93

Figure 5.36. Schematic reconstruction of the gate tower (Hartal, 2001); **A.** Reconstruction outline of enlarged tower with original tower enclosed in it. **B.** Second phase of the tower. The black arrow points to the original gate. .... 93

Figure 5.37. Evidence of the earthquake at the gate tower; **A.** The same stone has slid downwards out of three parallel arches at the main gate arch. **B.** A similar deformation is noticed at a passage-way parallel to the gate arch. **C.** The adjacent arch facing to the east was not deformed. **D.** Location of the passage-way, 10 meters west (left) of the main gate..... 94

Figure 5.38. The final DDA block system for the arch at Nimrod Fortress. four fixed points (squares) are assigned to the confining block, and five measurement points (circles) are assigned to the top arch blocks. The height of the wall above the arch is *h*. the lines intersecting the arch blocks represent material lines..... 96

Figure 5.39. Convention for arch blocks – K for keystone, A and B for the first and second block from the keystone respectively, and R or L to indicate right or left. .... 96

Figure 5.40. Spatial displacement of the 5 blocks over 40 seconds with  $A=1g, f=1\text{Hz}$ . Each symbol represents 2 seconds. **A.** measured displacements **B.** normalized displacements. .... 98

Figure 5.41. Spatial displacement of the 5 blocks over 40 seconds with  $A=1g, f=2\text{Hz}$ . Each symbol represents 2 seconds. **A.** measured displacements **B.** normalized displacements. .... 99

Figure 5.42. Graphical output of a simulation with  $A=1g, f=1Hz$ . ..... 100

Figure 5.43. Graphical output of a simulation with  $A=1g, f=2Hz$ . ..... 100

Figure 5.44. Relative normalized spatial displacement of Block  $A_r$  - influence of amplitude.  $f= 2Hz$ .  
..... 101

Figure 5.45. Relative normalized spatial displacement of Block  $A_r$  - influence of frequency.  $A = 1g$ .  
..... 102

Figure 5.46. Relative normalized spatial displacement of Block  $A_r$  - influence of wall stiffness. .... 102

Figure 5.47. Relative normalized spatial displacement of Block  $A_r$  - influence of overburden.  $t =10$   
sec,  $A=1.5g, f=3Hz$ ..... 103

Figure 5.48. Normalized spatial displacement of the 5 blocks over 10 seconds with  $A=1.5g, f=3Hz$   
and  $h=0$ . ..... 104

Figure 5.49. Graphical output of a simulation with  $A=1.5g, f=3Hz$  and  $h=0$ .  $t =10$  sec..... 104

Figure 5.50. Normalized displacement of stone  $A_r$  in the direction of the displacement vector over  
time ( $d = \sqrt{u^2 + v^2}$ ). After approximately 70 seconds the displacement stops and the structural  
deformation is ‘locked’ ..... 105

Figure 5.51. Corner chipping is seen in many of the rocks at the gate tower – an energy dissipation  
mechanism which can not be imitated with DDA. .... 107

Figure 6.1 The suggested response spectrum in Israel building code #413 (1998). The spectral  
amplification coefficient ( $R_a$ ) is plotted against the natural period (T) of the structure. All three  
structures in this study are founded on bedrock, thus behaving according to the  $S_1$  curve. The  
maximum structural amplification reaches 2.5 times the bedrock PGA. .... 112

# 1 Introduction

## 1.1 Seismic Hazard

Seismic activity in Israel is considered low to moderate (Arieh and Rabinowitz, 1989; Shapira, 1983), yet there are indications for at least 110 historic earthquakes in a magnitude range of  $6.7 < M_L < 8.3$  ( $M_L$  – local magnitude) which have affected the area and caused widespread destruction over the past 2500 years, 42 of which have originated along the Dead-Sea fault system (Ben-Menahem, 1991). In a world of intensified urbanization and rapid increase in population density, assessment of earthquake hazard and its application to existing building codes has become crucially important.

Figure 1.1 presents the seismic coefficient  $Z$  as predicted by Israel building code #413.  $Z$  is the expected Horizontal Peak Ground Acceleration (H-PGA) with a 10% probability for occurring at least once in 50 years. PGA is commonly used in earthquake engineering, although it bears no information on frequency of vibration, duration of ground motion, or the geological and geotechnical properties of the investigated site (Shapira, 1983; Shapira and Fernandez, 1989). The probability for a ground acceleration  $Z$  to be exceeded within a certain time span is typically estimated using empirical attenuation equations developed for a specific area. Attenuation equations describe the dissipation of seismic energy as a function of distance from the epicenter, and present a relationship between peak ground acceleration (PGA), Magnitude ( $M$ ), and distance ( $r$ ) to the epicenter of the earthquake.

Earthquake risk assessment in Israel is based on attenuation equations adopted from other places in the world, primarily California, due to scarce local strong-motion data, which can not provide an adequate and consistent basis for a reasonable derivation of relationships (Shapira and Fernandez, 1989; Shapira, 2002). The scarcity in strong-motion data in our area is a result of the relatively young seismic network and the moderate seismic activity.

In this research we develop an alternative method for obtaining strong ground-motion data: by back analysis of structural failures in archaeological sites. The results will provide constraints on PGA estimates, generated by the existing seismological strong motion catalogue in Israel.

## 1.2 Paleoseismology

The seismic network in Israel has been recording data for less than 100 years. A much wider time window has recently become available due to extensive paleoseismological research in Israel, which provides important parameters for seismicity evaluation of a specific area or fault, including earthquake return periods, characteristic earthquake, and maximum earthquake magnitude.

The seismicity of the main faults in Israel and adjacent regions has been studied using various methods and data bases:

Four thousand years of historical documentation and archaeological ruins allow derivation of a detailed catalogue of historical earthquakes, using mainly intensity scales and estimations of intensity-magnitude-distance relationships (Amiran et al., 1994; Ben-Menahem, 1991). An extensive catalogue enables division of a fault to active segments and definition of seismicity parameters for each segment (Ben-Menahem, 1991).

Recent dating of speleothems collapse in the Soreq cave near Jerusalem (Kagan et al., 2002) and of disrupted layers in lacustrine sediments at the shore of the Dead Sea (Enzel et al., 2000; Kentor et al., 2001; Marco et al., 1996; Migowski et al., 2004) show a possible correlation with each other and with the historic record of strong earthquakes ( $M_L > 5.5$ ). The geological record in both sites opens a 70,000 years time-window, and enables definition of recurrence intervals of seismic activity along the Dead Sea Transform (DST).

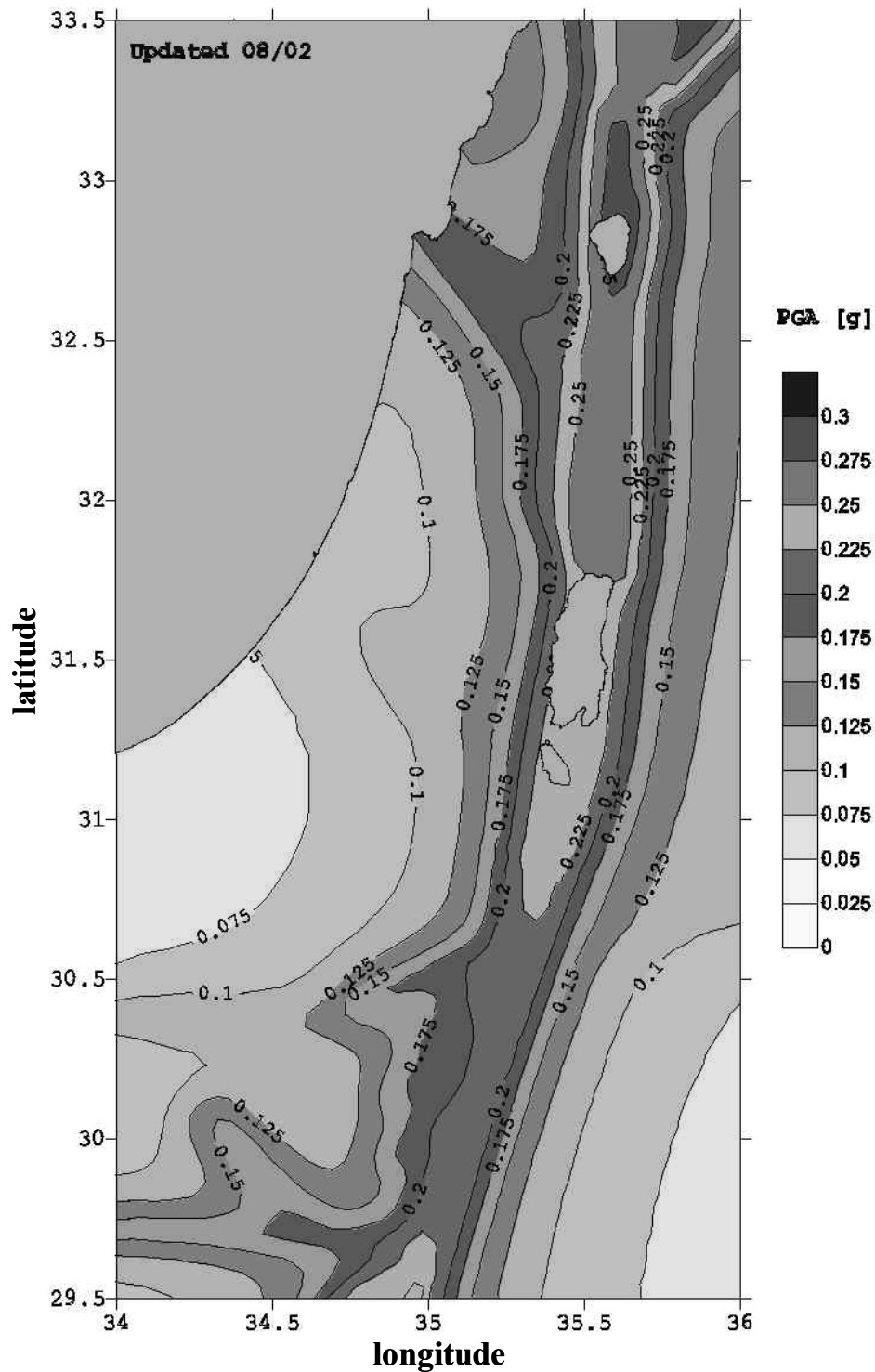


Figure 1.1. The seismic risk map of Israel. The map presents the seismic coefficient  $Z$  as predicted by Israel building code #413.  $Z$  is the expected Horizontal Peak Ground Acceleration (H-PGA) with a 10% probability for occurring at least once in 50 years. (Shapira, 2002)

Recurrence time estimations might be erroneous if specific earthquakes are not correctly associated with specific fault segments (Avni et al., 2002). Direct fault measurements have been performed using trenching of different segments of the DST (Marco et al., 2000; Zilberman et al.,

2000). Such measurements yield the amount and rate of slip on a fault, which may enable evaluation of the maximum expected magnitude.

Additional direct measurements have been performed in seven archaeological sites in Israel and the surrounding region, where exceptional circumstances resulted in surface faulting of archaeological ruins that are relatively well exposed. These provide accurate determination of date and amount of slip, thus improving the characterization of destructive earthquakes and of the seismicity of fault segments (Ellenblum et al., 1998; Galli and Galadini, 2001; Marco et al., 2003).

The paleoseismic research mentioned above focuses on determination of seismic behavior of faults. However, there is little reference, if any, to site response or characterization of ground motions, which are the relevant issues in seismic-hazard context and in determination of building codes around the world. Such parameters can be derived using mechanical back-analysis on either geological or man-made structures, under two conditions:

1. Knowledge of both initial and final positions of a structure – allows complete resolution of the displacement vector.
2. Knowledge of the mechanical properties and behavior of the structure – allows determination of the failure mechanism, and derivation of equilibrium equations.

An example of such a mechanical approach is the research performed by J. Brune and co-workers in Reno, Nevada (Anderson et al., 2000; Anooshehpour and Brune, 2002; Brune, 2002). The analysis is used to provide constraints on the level of ground motions, by assuming that precariously balanced rocks in seismically active regions are effectively upper-limit strong motion seismoscopes that have been in place for thousands of years. Thus, estimates of the dynamic toppling acceleration of these rocks (through rigid body rocking) can provide

constraints on the peak ground accelerations experienced during past earthquakes. Their results are compared and confirmed by physical and numerical models.

### **1.3 Research Objectives**

The scope of this research is to develop a new method for evaluation of threshold horizontal PGA values and characterization of ground motions of historical earthquakes using analytical and numerical solutions. It would be interesting to compare the results of this research with PGA values predicted by Israel Building Code on the basis of a completely different method.

In this work we focus on man-made masonry structures such as towers and arches, where the hewn stones that form the building provide a well-defined initial geometrical reference. Where failure is confined to displaced blocks within an otherwise intact structure, block displacement is measurable and a mechanical analysis is possible; this can not be achieved in completely collapsed structures. Additionally, the reliability of the results can be enhanced by elimination of other failure sources, such as poor construction methods or weak foundation material. Therefore, bedrock foundation and high-quality masonry are two favorable conditions for such an approach (Mazor and Korjenkov, 2001).

In search of suitable sites, an extensive survey of a large number of archaeological sites in Israel was performed. All considered sites exhibit earthquake destruction, although most of the structural failures, such as rotation of blocks or oriented collapse of walls and columns, are not applicable for the type of mechanical analysis which is required here.

The focus of this research, therefore, is narrowed down to the analysis of only two failure modes:

1. Block sliding out of a wall on a horizontal or an inclined plane - observed in Tel Kadesh, Monfort Fortress, and Avdat.

2. Block sliding out of a masonry arch - observed in Nimrod Fortress and Mamshit.

We present the suggested method of analysis using three case studies in Israel: The Nabatean cities of Avdat and Mamshit, and the Ayyûbid-Crusader Fortress of Nimrod, all presented in Fig 1.2.

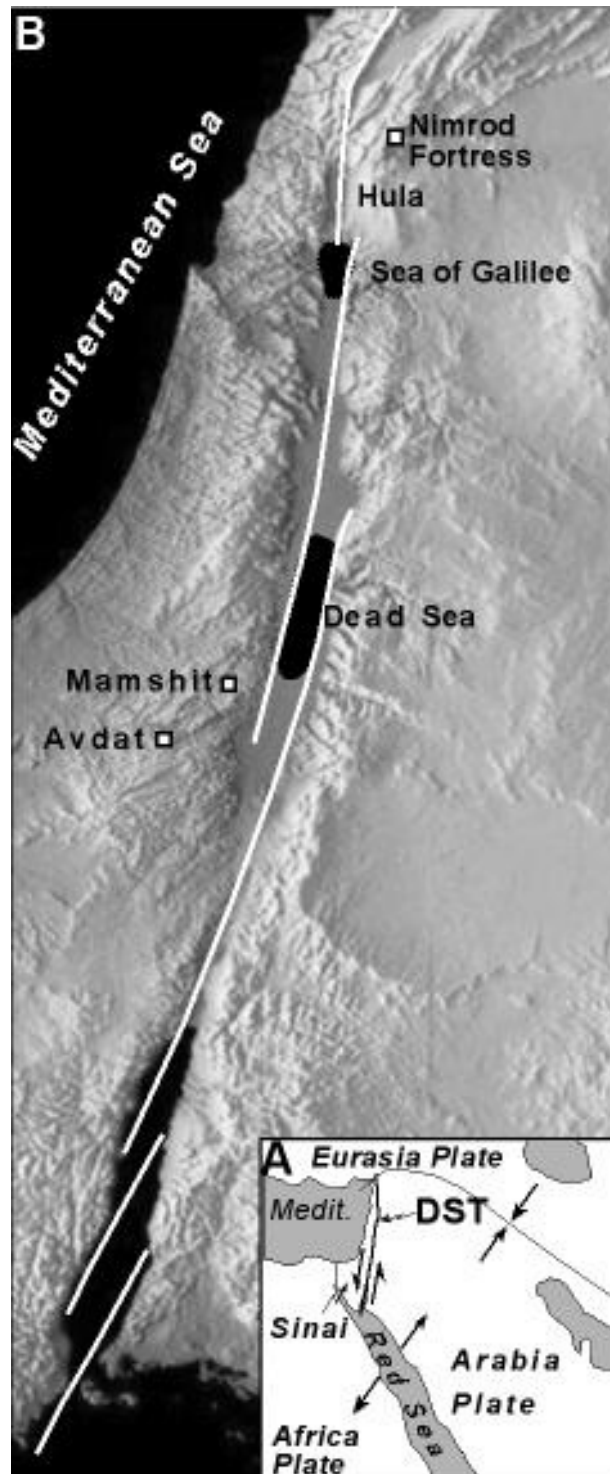


Figure 1.2. Location map of studied sites (After (Hall, 1994)). The three investigated sites – Avdat, Mamshit, and Nimrod fortress are marked, and their vicinity to the DST can be seen.

## 2 Theoretical Background

Existing methods for evaluating the performance of structures subjected to seismic loads are divided by Cai and Bathurst (1996) into three general categories, depending on the fundamental solution approach: (1) Force-based pseudo-static methods, (2) Displacement-based sliding block methods, and (3) Finite element methods. Methods from all three categories are discussed in this chapter and their application for dynamic analysis of structures is presented in Chapters 4 and 5. Sections 2.1.1-2.1.5 present solutions that are taken from earlier studies along with some new and original developments: The pseudo-static solution for a block on a plane (Section 2.1.1) together with the final integration for derivation of the displacement of a block on an incline (Section 2.1.2) are new developments of this research, based on classical force equilibriums. The dynamic solution of block response to induced displacement in the foundation (Section 2.1.3) is a novell solution, developed especially for this research, in order to validate the use of displacement as a loading mechanism in DDA. Apart from these developments, other parts of this chapter introduce the statics of a masonry arch (Section 2.1.4) and some fundamentals of the numerical DDA method (Sections 2.1.2 and 2.2.2) and are basically a literature review of the subject.

### 2.1 Analytical Solutions

#### 2.1.1 *Block on a plane – pseudo static solution*

The pseudo-static methods are probably the most common approach for seismic engineering design of structures. The basic premise in pseudo-static methods is that the structure is at a state of limit-equilibrium under the action of acceleration-induced inertial forces superimposed on the static forces (Cai and Bathurst, 1996). The implementation of a pseudo-static analysis requires input of the geometry of the structure and of the frictional parameters of the sliding surface. The threshold acceleration is obtained at limit equilibrium between the total resisting forces and the

total destabilizing force. The pseudo-static analysis is incapable of quantifying the amount of displacement, calculated using different methods and is dependant on the frequency and duration of the earthquake (Cai and Bathurst, 1996; Goodman and Seed, 1966; Newmark, 1965).

Figure 2.1 presents a single block sliding out of a masonry wall, between two frictional surfaces, top and bottom. The analysis is restricted to a two-dimensional perspective and is based on three assumptions:

1. The only block that moves out of the wall is the analyzed block (shaded in Figure 2.1).
2. The weight of the overlying blocks is distributed homogenously so that the overlying weight only depends on the width ( $d$ ) and density ( $\rho$ ) of the blocks.
3. There is no cement between the blocks so that the resisting force is only a function of the friction angle along the interface.

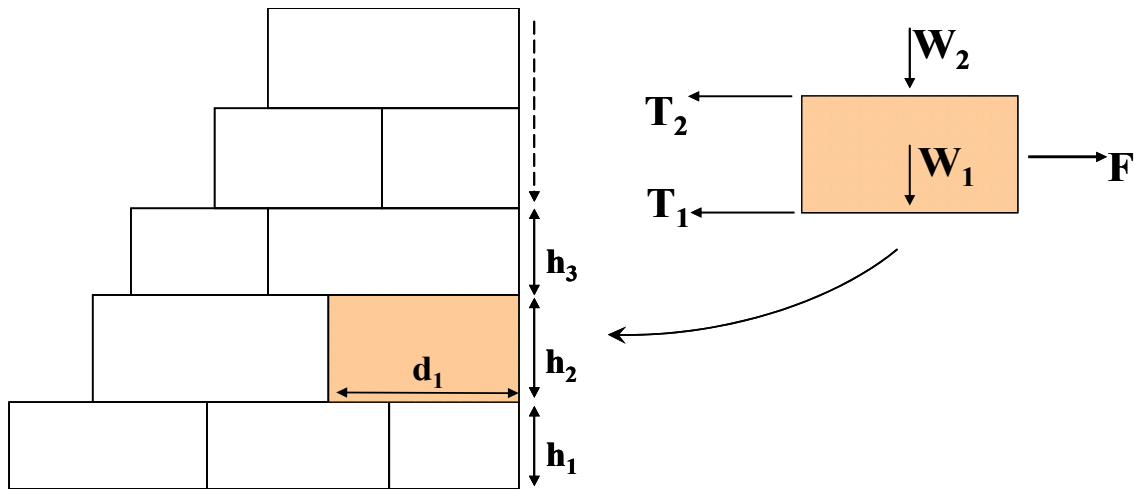


Figure 2.1. Schematic presentation of the forces acting on a block in a masonry wall. The shaded block is analyzed,  $T_1$  and  $T_2$  are the frictional forces resisting to the sliding movement, and  $F$  is the driving force.

The static equilibrium equations for this case are as follows

$$W_1 = (h_2 + h_3 + \dots h_n) \cdot d_1 \cdot t \cdot \rho \cdot g \quad (2.1)$$

$$W_2 = (h_3 + \dots h_n) \cdot d_1 \cdot t \cdot \rho \cdot g \quad (2.2)$$

$$T_2 = W_2 \cdot \tan \phi \quad (2.3)$$

$$T_1 = W_1 \cdot \tan \phi \quad (2.4)$$

$$F = m_{block} \cdot a \quad (2.5)$$

$$m_{block} = h_2 \cdot d_1 \cdot t \cdot \rho \quad (2.6)$$

where  $t$  is the depth of the blocks, which is the third dimension that does not appear in Figure 2.1 and  $\rho$  is block density.

In equilibrium:  $F = T_1 + T_2$ , which results in:

$$a_{threshold} = \frac{(W_1 + W_2)}{m_{block}} \cdot \tan \phi = \frac{(2(h_3 + \dots h_n) + h_2)}{h_2} g \cdot \tan \phi \quad (2.7)$$

It can be seen that the only parameters that effect the threshold acceleration are the interface friction angle and the ratio between the analyzed block height and the overlying blocks height. Seismogenic upward vertical accelerations may reduce the overburden on the frictional surfaces, thus reducing threshold accelerations. The effect of adding vertical accelerations can be calculated under the assumption that all the blocks are effected by the acceleration in the same way, as a vector acting on the block centroid. In this case the block weight becomes:

$$W = h \cdot d \cdot t \cdot \rho \cdot (g - a_v) \quad (2.8)$$

where  $a_v$  is the vertical acceleration, upward considered positive, therefore the threshold horizontal acceleration is:

$$a_{threshold} = \frac{(2(h_3 + \dots h_n) + h_2)}{h_2} \tan \phi \cdot (g - a_v) \quad (2.9)$$

Equation 2.9 shows that an increase in vertical acceleration will reduce the threshold horizontal accelerations and vice versa.

### 2.1.2 Block on an incline – dynamic solution

A displacement based sliding block model was first proposed by Newmark (1965) and by Goodman and Seed (1966), and is now largely referred to as “Newmark” type analysis.

Determination of the amount of displacement during an earthquake necessarily involves two steps (Goodman and Seed, 1966):

1. Determination of horizontal acceleration required to initiate downslope motion, also known as “yield acceleration” ( $a_y$ ), which can be found by pseudo-static analysis.
2. Evaluation of the displacement developed during time intervals when yield acceleration is exceeded, by double-integration of the acceleration time-history, with the yield acceleration used as reference datum (Fig. 2.2).

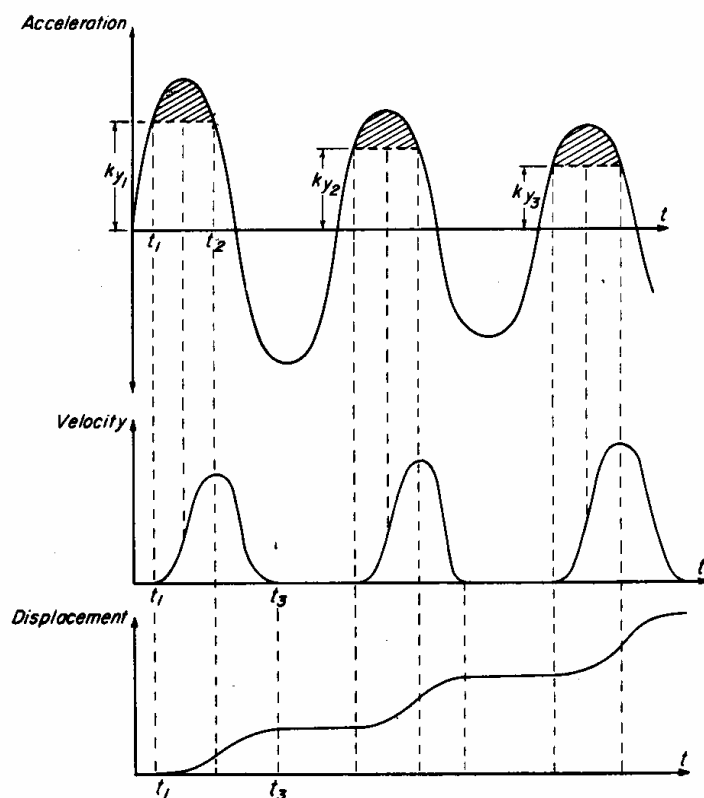


Figure 2.2. An example of the displacement-based solution, also known as “Newmark type” solution. The displacement in the lower figure results from the double integration of the acceleration function in the upper figure between  $t_1$  and  $t_2$  - beyond the yield acceleration ( $k_y$  in this figure) (Goodman and Seed, 1966).

Figure 2.3 displays a block on an inclined plane, subjected to gravitational acceleration and a horizontal, time-based, sinusoidal acceleration as driving forces.

Goodman and Seed (1966) show that for this case the yield acceleration is given by:

$$a_y = \tan(\phi - \alpha)g \quad (2.10)$$

For the acceleration record of the form  $a = kg \sin(\omega t)$  as displayed in Figure 2.3, where  $\omega$  is the frequency of the function and  $k$  calibrates the proportion between  $a$  and  $g$ , the corresponding time interval  $\theta$  until motion ensues is:

$$\theta = \frac{\sin^{-1}(a_y / kg)}{\omega} \quad (2.11)$$

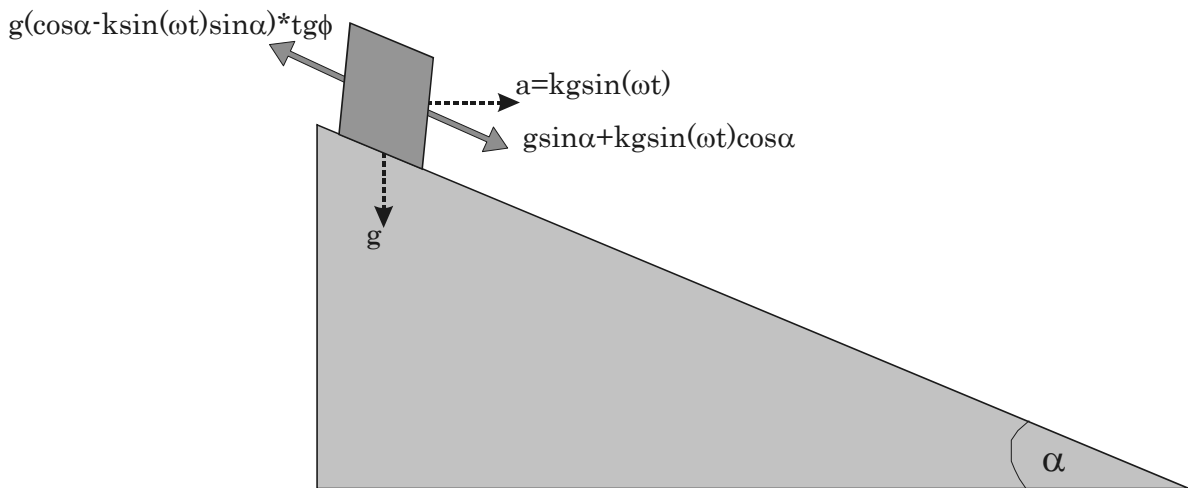


Figure 2.3. Schematic presentation of the forces acting on a single block lying on an incline. The activating force is a horizontal time-based sinusoidal acceleration. The resisting frictional force is constant; the friction angle does not change after motion begins.

The downslope acceleration of the sliding block can be determined by subtracting the resisting forces from the driving forces, as described in Figure 2.3:

$$a_t = [kg \sin(\omega t) \cos \alpha + g \sin \alpha] - [g \cos \alpha - kg \sin(\omega t) \sin \alpha] \tan \phi \quad (2.12)$$

Similarly, the displacement of the block at any time is determined by double integration on the acceleration, with  $\theta$  as reference datum:

$$d_t = \int_{\theta}^t v = \iint_{\theta} a = g[(\sin \alpha - \cos \alpha \tan \phi)(t^2 / 2 - \theta t)] + \frac{ag}{\omega^2} [(\cos \alpha + \sin \alpha \tan \phi)(\omega \cdot \cos(\omega\theta)(t - \theta) - \sin(\omega t) + \sin(\omega\theta))] \quad (2.13)$$

Eq. 2.13 provides the analytical solution for the dynamic displacement of a block on an inclined plane with inclination  $\alpha$  and friction angle  $\phi$ , starting from rest and subjected to a sinusoidal loading function with frequency  $\omega$ .

### 2.1.3 Block response to induced displacements in the foundation – dynamic solution

Figure 2.4 presents two blocks: the basement block (Block 1) is subjected to a horizontal displacement input function, and the upper block (Block 2) responds dynamically. Our analytical solution of such a case will consider one degree of freedom only: both blocks are confined to horizontal motions only, whereas in reality the upper block may experience rotation, bouncing, or even plowing.

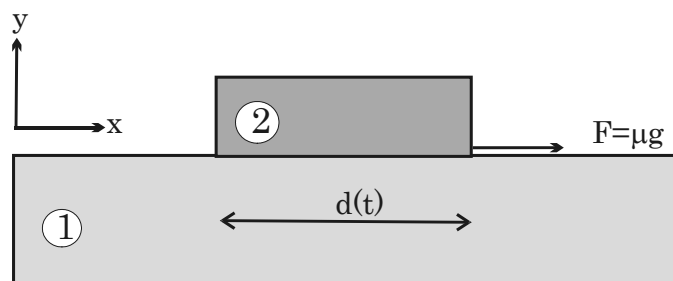


Figure 2.4. Schematic presentation of the case of an upper block (2), lying on the foundation block (1) which is subjected to a dynamic displacement input function.

The only force acting on Block 2 other than gravity is the frictional force, which immediately determines the acceleration of Block 2:

$$m_2 a_2 = F_{friction} \quad (2.14)$$



$$m_2 a_2 = \mu \cdot m_2 g \quad (2.15)$$



$$a_2 = \mu \cdot g \quad (2.16)$$

where  $\mu$  is the friction coefficient.

The direction of the driving force is determined by the direction of the relative velocity between Block 1 and 2 ( $v_1^*$ ). When Block 1 moves to the right relative to Block 2, the frictional force pulls Block 2 in the same direction, and determines the sign of  $a_2$ .

When Block 2 is at rest in relation to the Block 1, the frictional force is determined by the acceleration of the bottom block ( $a_1$ ). The threshold acceleration, under which the two blocks move in harmony, is equal to the friction coefficient multiplied by the gravitation acceleration ( $\mu g$ ). When the acceleration of the Block 1 passes the threshold value, the frictional forces act in the same direction as  $a_1$ .

The positive direction is determined by the sign convention in Figure 2.4, and the relative velocity of Block 1 is given by:

$$v_1^* = v_1 - v_2 \quad (2.18)$$

The direction of the acceleration of Block 2 is set by the following boundary conditions and inequalities:

$$\begin{aligned}
 & \text{if } v_1^* = 0 \dots\dots\dots \text{and } |a_1| < \mu g \dots\dots\dots a_2 = a_1 \\
 & \qquad \qquad \qquad \text{and } |a_1| > \mu g \dots\dots\dots \text{and } a_1 > 0 \dots\dots\dots a_2 = \mu g \\
 & \qquad \qquad \qquad \qquad \qquad \qquad \text{and } a_1 < 0 \dots\dots\dots a_2 = -\mu g \\
 \\
 & \text{if } v_1^* \neq 0 \dots\dots\dots \text{and } v_1^* > 0 \dots\dots\dots a_2 = \mu g \\
 & \qquad \qquad \qquad \text{and } v_1^* < 0 \dots\dots\dots a_2 = -\mu g \quad (2.17)
 \end{aligned}$$

The implementation of these conditions into a Matlab algorithm is shown in Appendix 1.

### 2.1.4 The masonry arch

A masonry arch is a common ancient structure, typically used in construction of vaults in cathedrals, fortresses, and public facilities. It is composed of wedge-shaped blocks, “voussoirs”, with or without cementing material between them. When cementing material does exist there is very little of it and its strength is negligible, therefore it is typically ignored in stability analyses of such structures.

The structural behavior of masonry arches has attracted much attention since the 18th century, because of their extensive use in both ancient and modern structures. A variety of approaches have been used to model masonry arch behavior, starting with large scale field tests (Boothby et al., 1998), through analytical attempts to describe the limit behavior of the arch at the collapse point (Blasi and Foraboschi, 1994; Heyman, 1982; Sinopoli et al., 1997; Vilnay, 1988), and onto numerical modeling of the dynamic arch behavior under base-motions or vertical loads (Bicanic et al., 2003; Clemente, 1998; De Luca et al., 2004).

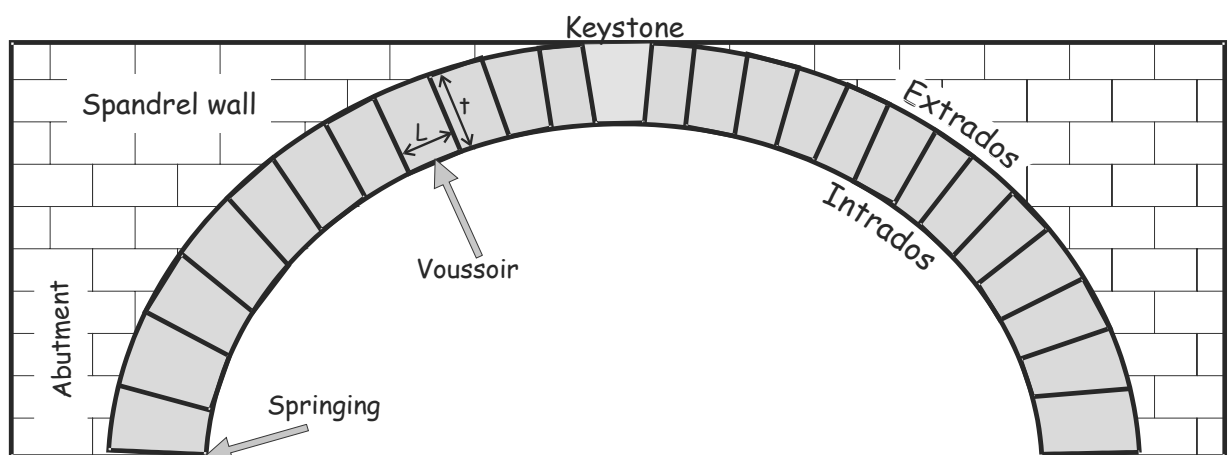


Figure 2.5. Structural terms for the masonry arch

The following analysis is an attempt to deal with horizontal accelerations through pseudo-static analysis, in order to simplify the understanding of the behavior of the arch during an earthquake.

The study of the strength of masonry arches is based on three key assumptions (Heyman, 1982):

1. Sliding failure cannot occur; either because friction is too high, or because the wedge-shaped blocks are effectively interlocked.
2. Masonry has no tensile strength; although the masonry material itself has a definite tensile strength, the masonry mass cannot transmit tensile forces since the joints between voussoirs are dry or filled with weak cement.
3. Masonry has an infinite compressive strength; this assumption implies that stresses are so low in masonry construction that there is no danger of crushing the material.

The most significant assumption considering the strength of the arch is the second one, which indicates that failure of the arch is conditioned by the existence of tensile forces at the joints.

Since there is no tensile strength across the joints, such forces cause opening of some of the joints by hinge formation either at the top or the bottom of the joint, and by rotation of the voussoirs about their edges.

The location of hinges and amount of rotation determine the mode of failure the arch experiences, if rotation is not arrested. The existence of tensile forces at the joints can be studied by investigating the position of the thrust line (Heyman, 1982; Vilnay and Cheung, 1986).

The thrust line connects all equivalent stress vectors, representing the compressive stresses transmitted between the voussoirs, at equilibrium with external loads. Note that the thrust line is not necessarily transmitted normal to the faces of the voussoirs; instead, at each section there is a normal force accompanied by a tangential shear one, that might cause slip between voussoirs if interlocking is not sufficient.

If the thrust line is entirely contained within an arch, the arch is stable. On the other hand, if the line of thrust touches the edge of the arch ring, a hinge will form. This ‘safe’ theorem regarding the stability of the arch is displayed in Figure 2.6.a and is formulated by Heyman (1982):” *If a*

*thrust line can be found, for the complete arch, which is in equilibrium with the external loading (including self weight) and which lies everywhere within the masonry of the arch ring, then the arch is safe”.*

It can be shown that arch stability increases with arch thickness ( $t$  on Figure 2.5). Figure 2.6.b displays the critical thickness of the arch in which the thrust line is still included, a thinner arch would not be stable. Vilnay and Cheung (1986) study the case of a simply supported three voussoir arch, and find a critical “aspect ratio”- the ratio between arch thickness ( $t$ ) and voussoir length ( $L$ ) – above which the arch is always stable under uniformly distributed load.

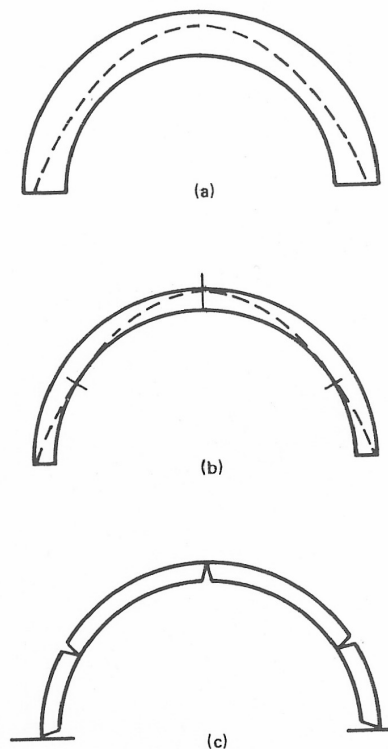


Figure 2.6. The thrust line : (a) The thrust line is comfortably contained within the arch, (b) The thinnest possible arch, in which the thrust line touches the edge at 5 points, (c) The arch is on the point of collapse, by formation of 5 hinges, where the thrust line touched the edge in 2.6.b. (Heyman, 1982)

The stability of an arch with a constant thickness can be disturbed by application of external loads. Figure 2.7 displays the two end conditions for which the arch is stable. The minimum and

maximum abutment thrust  $H$  can be determined by moment equilibrium at the hinges (Blasi and Foraboschi, 1994; Heyman, 1982; Vilnay and Cheung, 1986), since any point on the thrust line itself has zero moments.

We chose to use the full derivation of the horizontal thrust  $H$ , displayed by Blasi and Foraboschi (1994) for both a "lower collapse mechanism" (Fig 2.7.a) and an "upper collapse mechanism" (Fig 2.7.b) of a semicircular arch under a uniformly distributed load.

The following analysis relates to a free standing arch only, since there is no agreement as to the amount of constraints the spandrel walls apply on the arch response (Boothby, 1996). In addition, in order to find the critical acceleration ( $a_c$ ) in a pseudo-static type analysis the magnitude of  $H_{\min}$  and  $H_{\max}$  must be divided by a corresponding mass. It is not clear which mass should be considered for the expression of the critical inertia force:

$$F_I = m \cdot a_c \quad (2.18)$$

whether the mass of the arch only, or the mass of the entire surrounding structure in which the arch is embedded.

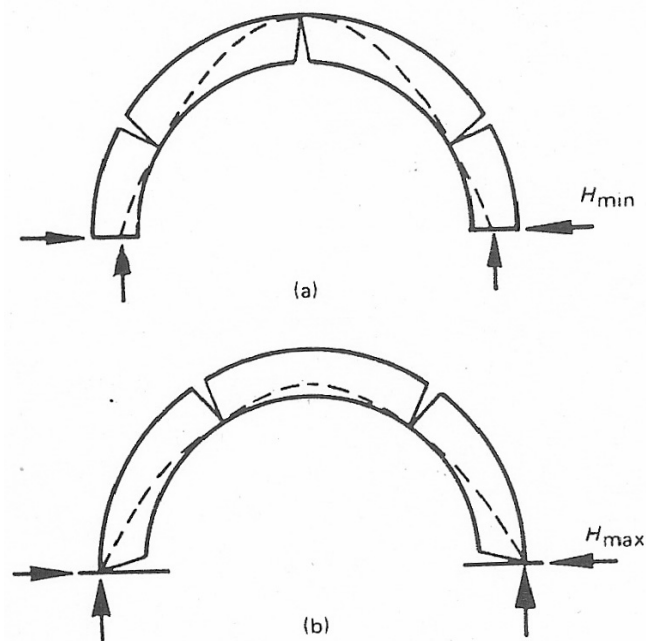


Figure 2.7. A semicircular arch with: (a) The least possible value for abutment thrust,  $H_{\min}$  (b) The greatest possible value for abutment thrust,  $H_{\max}$ . (Heyman, 1982)

Finding  $H_{\min}$ :

The arch, which is presented in Figure 2.8, has a radius  $R$ , a constant thickness  $s$  and a unit weight  $w$ . A hinge is set in the intrados in a generic position D and another hinge is set in the crown section to obtain a collapse mechanism. The position of the hinge in D is defined by the angle  $\theta$ , which is a variable.

The rotational equilibrium equation about D follows, where  $H_b$  is the internal force applied at point B:

$$H_b \cdot [(r + s) - r \sin(\theta)] = P_v \cdot d_1 + Q_v \cdot d_2 \quad (2.19)$$

The expressions providing  $P_v$ ,  $d_1$ ,  $Q_v$  and  $d_2$  in Eq. 2.19 are obtained in the following.

The weight  $P$  of the half arch with thickness  $t = 1$  is given by:

$$P = \frac{\pi}{2} \cdot R \cdot s \cdot w \quad (2.20)$$

Therefore the weight  $P_v$  of ABCD is:

$$P_v = P \cdot \left(1 - \frac{\theta}{\pi/2}\right) = \frac{\pi}{2} \cdot R \cdot s \cdot w \cdot \left(1 - \frac{\theta}{\pi/2}\right) \quad (2.21)$$

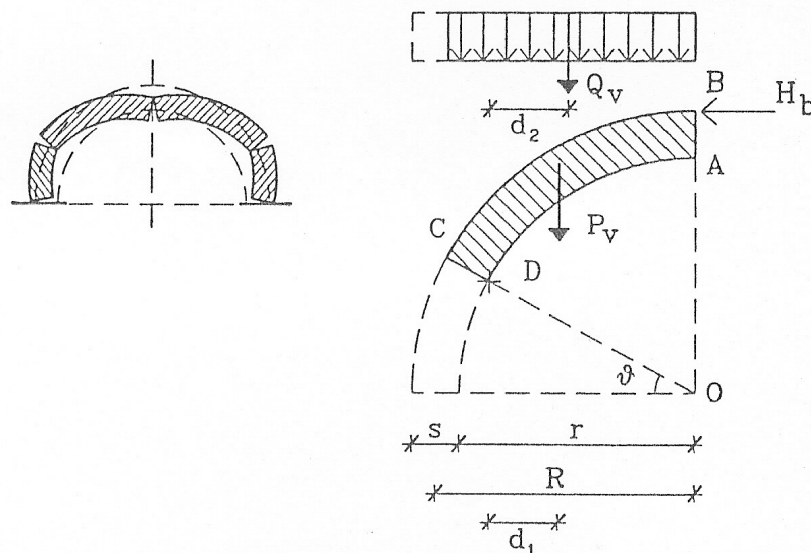


Figure 2.8. Lower horizontal limit thrust (Blasi and Foraboschi, 1994)

The arm  $d_1$  of  $P_v$  is obtained by another moment equilibrium with respect to the arch symmetry axis:

$$P_v \cdot [r \cdot \cos(\theta) - d_1] = \int_{\theta}^{\frac{\pi}{2}} s \cdot R^2 \cdot w \cdot \cos(\theta) d\theta \quad (2.22)$$

$d_1$  is obtained from (2.21) and (2.22) and is :

$$d_1 = r \cdot \cos(\theta) - \frac{2 \cdot R \cdot [1 - \sin(\theta)]}{\pi \cdot \left(1 - \frac{\theta}{\pi/2}\right)} \quad (2.23)$$

The resultant  $Q_v$  of the part of the uniformly distributed load  $q$  applied on BC is given by:

$$Q_v = q \cdot (r + s) \cdot \cos(\theta) \quad (2.24)$$

The arm  $d_2$  of  $Q_v$  is given by the following relationship:

$$d_2 = r \cdot \cos(\theta) - \left(\frac{r+s}{2}\right) \cdot \cos(\theta) \quad (2.25)$$

Substitution of Eq. 2.21, 2.23, 2.24 and 2.25 into Eq. 2.19, yields an expression for  $H_b$  as a function of the angle  $\theta$ . The value of  $\theta$  that produces the maximum thrust is the angle of the hinge in the haunch of the lower mechanism.

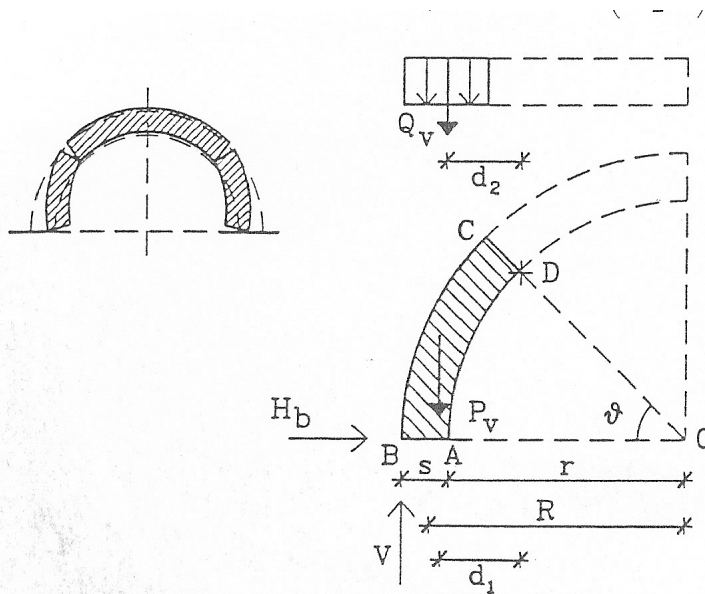


Figure 2.9. Upper horizontal limit thrust (Blasi and Foraboschi, 1994)

Finding  $H_{max}$ :

The same arch and loads as in the case of the lower mechanism are considered. Referring to Figure 2.9, a hinge is set at the arch's intrados in a generic position D and another hinge is set at the skewback.

The rotational equilibrium about D is given by:

$$H_b \cdot r \cdot \sin(\theta) = V \cdot [(r + s) - r \cdot \cos(\theta)] - P_v \cdot d_1 - Q_v \cdot d_2 \quad (2.26)$$

The expressions providing  $V$ ,  $P_v$ ,  $d_1$ ,  $Q_v$  and  $d_2$  in Eq. 26 are obtained in the following:

$$V = P + q \cdot (r + s) = \frac{\pi}{2} \cdot R \cdot s \cdot w + q \cdot (r + s) \quad (2.27)$$

$$P_v = \frac{\pi}{2} \cdot R \cdot s \cdot w \cdot \left( \frac{\theta}{\pi/2} \right) \quad (2.28)$$

$$d_1 = \frac{R \sin(\theta)}{\theta} - r \cdot \cos(\theta) \quad (2.29)$$

$$Q_v = q \cdot (r + s) \cdot [1 - \cos(\theta)] \quad (2.30)$$

$$d_2 = \left( \frac{r + s}{2} \right) \cdot [1 - \cos(\theta)] + s \cdot \cos(\theta) \quad (2.31)$$

To obtain the upper horizontal limit thrust from Eq. 2.26, the value of  $\theta$  corresponding to the upper mechanism must be evaluated. Structural considerations similar to those developed for the lower thrust show that the value of the upper thrust is the minimum value of  $H_b$  with respect to  $\theta$ .

Since the calculation of the abutment thrust at steady state is too complex (Blasi and Foraboschi, 1994), most publications are restricted to the development of collapse analysis and thrust calculations at critical stages. Therefore, the thrust at the abutments of a semi circular arch at limiting static equilibrium is unknown, but should be between  $H_{max}$  and  $H_{min}$ . Consequently, the largest possible inertia force required to turn the arch into a mechanism must be the difference

between the two extremes, and the horizontal threshold acceleration is that inertia force divided by the mass of the entire arch.

#### Limitations and reservations of the pseudo-static solution:

1. The derived critical acceleration value is pseudo-static; therefore it does not describe reliably the dynamic behavior of the arch during a progressive failure process.
2. The discussed solutions are only valid for semi-circular arches; the arch in Nimrod Fortress for example has a different geometry and therefore in this and similar cases the pseudo-static analytical solution will not be valid.
3. The procedure does not consider spandrel walls, thus results are approximate only.
4. Unique failures, where arch deformation is arrested and complete collapse is not achieved, as seen in the cases of Mamshit and Nimrod, can not be solved by this procedure.

## **2.2 Numerical Solutions**

### *2.2.1 Background*

Numerical methods and computing techniques are rapidly becoming common design tools in rock mechanics and rock engineering. Such methods allow formulating conceptual models and mathematical theories integrating diverse information about geology, physics, structural engineering, construction techniques, and their interactions. An extensive and comprehensive review of techniques and advances in numerical modeling for rock mechanics and rock engineering is presented by L. Jing (2003), and is the main information source for this section. Problems in rock mechanics and rock engineering differ from each other by the characterization of the problem domain, the heterogeneity of the rock mass, and the extent of resolution of the

problem. Due to the differences in the underlying material assumptions, different numerical methods have been developed for continuous and discrete systems.

The continuous approach assumes full continuity within the problem domain which requires a division of the problem domain into an infinite number of elements, thus applying infinite degrees of freedom. The computational process of such an approach is obtained by discretization of the continuum, and by sub-division of the problem domain into a large number of standard-shaped elements, with a finite number of degrees of freedom. The most common and popular numerical method in this group, and practically in all engineering sciences, is the Finite Elements Method (FEM).

The Discrete Element Method (DEM) originated from several disciplines, such as rock mechanics, structural analysis and multi-body systems. It focuses mostly on applications in the fields of fractured or particulate geological media and divides the problem domain into well-defined components. The behavior of each component (element) and of the contacts between them is well known. The key concept of DEM is that the domain of interest is treated as an assemblage of rigid or deformable blocks, where the contacts among them are identified and continuously updated during the entire deformation process, and represented by proper constitutive models.

Large displacements caused by rigid body motion of individual blocks, including block rotation, fracture opening and complete detachments are straightforward in the discrete approach, but impossible to model in the continuous approach.

Numerical solution schemes are often referred to as being explicit or implicit. When a direct computation of the dependent variables can be made in terms of known quantities, the computation is said to be explicit. In contrast, when the dependent variables are defined by coupled sets of equations, and either a matrix form or an iterative technique is needed to obtain the solution, the numerical method is said to be implicit. Although programming of implicit

solution methods is complex, and requires more computational effort in each solution step, the principal reason for using an implicit approach is to allow for large time-steps.

The implicit DEM is represented mainly by the Discontinuous Deformation Analysis (DDA) method, originated by Shi (1993). It occupies the front position in terms of development and application among other implicit DEM methods (Jing, 2003). DDA has two advantages over the explicit DEM: permission for relatively larger time steps, and closed-form integrations for the stiffness matrices of elements. In this research numerical analysis will be performed using DDA. Further information on the different numerical methods can be found in Jing (2003).

### *2.2.2 Basic concepts of DDA*

In this section the basic concepts of DDA are briefly reviewed; a more complete description is provided by Shi (1993).

The DDA method solves a finite element type of mesh, where all elements are real isolated blocks, and the unknowns of the equations are the displacements and deformations of the blocks. The blocks are not restricted to standard shapes as in FEM, but can be of any convex or concave shape. When the blocks are in contact, Coulomb's friction law applies to the contact interface, and the simultaneous equilibrium equations are formulated and solved for each loading or time increment. The formulation is based on minimization of the system potential energy, following the second law of thermodynamics.

Although originating from the discrete element method family, DDA closely parallels the finite element method and is basically a generalization of it (Shi, 1993).

DDA considers both statics and dynamics using a time-step marching scheme and an implicit algorithm formulation. The difference between static and dynamic analysis is that the former assumes the velocity as zero in the beginning of each time step, while the latter inherits the velocity of the previous time step.

Block system kinematics in DDA has two constraints: no-penetration and no-tension between blocks. These two constraints are applied using a "penalty" method, in which stiff springs are attached to block contacts. Since tension or penetration at the contacts will result in expansion or contraction of the springs, a process that requires energy, the minimum energy solution is one with no tension or penetration.

Blocks in DDA are "simply deformable", namely stresses and strains are constant throughout the block.

One of the strengths of the DDA method is that the mode of failure of the block system is a result of the analysis and not an assumption. Consequently, it is critical to test the ability of DDA to correctly model initiation of failure involving sliding and/or toppling of blocks. Many validations for DDA have been published recently, some of which will be discussed in the next chapter.

In this research a new C/PC version of DDA is used where earthquake acceleration can be input directly in every time step (Shi, 1999).

#### Basic formulations:

The plane displacement  $(u,v)$  of any point  $(x,y)$  in a block  $i$  can be represented by six displacement variables which yield the displacement matrix of the block

$$[D_i] = (u_0 \ v_0 \ r_0 \ \varepsilon_x \ \varepsilon_y \ \gamma_{xy}) \quad (2.32)$$

where the first three are the rigid body displacement and rotation, and the last three are normal and shear strains in the block. It can be shown that the complete block deformation matrix is:

$$\begin{pmatrix} u \\ v \end{pmatrix} = \begin{pmatrix} 1 & 0 & -(y-y_0) & (x-x_0) & 0 & (y-y_0)/2 \\ 0 & 1 & (x-x_0) & 0 & (y-y_0) & (x-x_0)/2 \end{pmatrix} \begin{pmatrix} u_0 \\ v_0 \\ r_0 \\ \varepsilon_x \\ \varepsilon_y \\ \gamma_{xy} \end{pmatrix} \quad (2.33)$$

Assuming  $n$  blocks in the defined block system, the simultaneous equilibrium equations have the form:

$$\begin{pmatrix} K_{11} & K_{12} & K_{13} & \cdots & K_{1n} \\ K_{21} & K_{22} & K_{23} & \cdots & K_{2n} \\ K_{31} & K_{32} & K_{33} & \cdots & K_{3n} \\ \vdots & \vdots & \vdots & \ddots & \vdots \\ K_{n1} & K_{n2} & K_{n3} & \cdots & K_{nn} \end{pmatrix} \begin{pmatrix} D_1 \\ D_2 \\ D_3 \\ \vdots \\ D_n \end{pmatrix} = \begin{pmatrix} F_1 \\ F_2 \\ F_3 \\ \vdots \\ F_n \end{pmatrix} \quad (2.34)$$

where each coefficient  $K_{ij}$ , is defined by the contacts between blocks  $i$  and  $j$ , and where  $i = j$  it depends on the material properties of block  $i$  alone.

Because each block has six degrees of freedom ( $u_0 \ v_0 \ r_0 \ \varepsilon_x \ \varepsilon_y \ \gamma_{xy}$ ) each element  $K_{ij}$  in the coefficient matrix is a 6 X 6 submatrix.  $D_i$  and  $F_i$  are 6 X 1 submatrices where  $D_i$  represents the deformation variables of block  $i$ , and  $F_i$  is the loading on block  $i$  distributed to the six deformation variables.

The equilibrium equations are derived by minimizing the total potential energy  $\Pi$  produced by the forces and stresses. The  $i^{\text{th}}$  row of Eq. 2.34 consists of six linear equations

$$\frac{\partial \Pi}{\partial d_{ri}} = 0, \quad r = 1, \dots, 6 \quad (2.35)$$

where  $d_{ri}$  is the deformation variable of block  $i$ . The total potential energy  $\Pi$  is the summation over all the potential energy sources: individual forces and stresses.

#### The DDA program package (Young, 1996):

DDA method is comprised of 4 different computer programs: DL, DC, DF and DG;

- Program DL generates lines representing joints, the boundary of the joint domain, and perimeters of tunnels. Geological layers are represented as a joint set. The joint lines are generated by statistics based on the average spacing, average length, average bridge (Shi

and Goodman, 1989), and degree of randomness of each joint set. In addition to the statistically-generated joint lines, other lines can also be input directly to define blocks that are not formed by the joint lines.

- Program DC generates the block system by forming all possible blocks from individual line segments defined by DL. After all intersection points are computed, the "dead branches" that do not contribute to forming finite blocks are deleted automatically by the program. Once the blocks are identified, DC computes and saves the block area and the block integral. In addition, specific points such as fixed points, measuring points, loading points and hole points are defined.
- Program DF performs the DDA forward static or dynamic analyzes of a block system defined by DC. Physical data added at this point are material constants, point loads, body forces, initial stresses, and initial velocity.

Four numerical parameters are defined:  $k01$ ,  $g2$ ,  $g1$ , and  $g0$ .

- Dynamic control parameter ( $k01$ ) - defines the type of the analysis required, from static to fully dynamic. For static analysis the velocity of each block is set to zero at the beginning of each time step,  $k01=0$ . In the case of the dynamic analysis the velocity of each block at the end of a time step is fully transferred to the next time step,  $k01=1$ . Different values of  $k01$  between 0 and 1 correspond to different degrees of damping or energy dissipation.
- Assumed maximum displacement ratio ( $g2$ ) – The calculated maximum displacement within a time step is limited to an assumed maximum displacement in order to ensure infinitesimal displacement within a time step. The maximum displacement within a time step is limited to  $g2*W$ , where  $W$  is half the vertical length of the analysis domain.

- Upper limit of time step size ( $g_1$ ) – The maximum time interval that can be used in a time step.
- Penalty value ( $g_0$ ) - is the stiffness of contact springs, used to enforce contact constraints between blocks.

For each time step, all of the block contacts are found. The general equilibrium equations are formulated and solved iteratively, using an "open-close" iteration method, until there are no penetration and no spring tension. At the end of the time step, all the blocks are in equilibrium with appropriate contact conditions.

- Program DG is a graphic post-processor, which displays graphic output on screen and produces postscript files for printing. In addition, it also draws the principal stresses in every block at the end of the analysis.

Over the last decade, researchers in the DDA community have dedicated a great deal of effort to prove the accuracy of the method by performing validation studies. MacLaughlin and Doolin (2005) review more than 100 validation studies with respect to analytical solutions, laboratory and field data, and other numerical techniques. DDA performance was found to be more than adequate for engineering applications.

### 3 Experimental

#### 3.1 Mechanical properties of intact rocks

Original building stones were taken from the three archaeological sites, under supervision of the Israel Nature and Parks Authority, to the Rock Mechanics Laboratory of the Negev at Ben-Gurion University (RMLN, BGU). Lab tests were performed in order to obtain physical and mechanical properties of intact rock samples as described below. Test results are summarized in Table 3.1.

- Density and porosity of the material were calculated according to the formulae:

$$\rho (\text{Kg} / \text{m}^3) = \frac{m}{V} \quad (3.1)$$

where  $m$  and  $V$  are the mass and the volume of the specimen, respectively.

$$n (\%) = \frac{V_v}{V_t} = 1 - \frac{\rho_t}{\rho_s} \quad (3.2)$$

where  $V_v$  and  $V_t$  are void and total volume of the specimen respectively, and  $\rho_t$  and  $\rho_s$  and total and solid densities of the specimen respectively.

Calculations were performed under assumptions of dry conditions ( $w=0\%$ ) and specific gravity ( $G.S.$ ) of 2.7.

- Dynamic elastic constants such as Poisson's ratio ( $\nu_d$ ), Young's modulus ( $E_d$ ), and shear modulus ( $G_d$ ) were obtained from ultrasonic velocity tests performed on solid cylinders (Figure 3.1.A), in complete adherence to ISRM standard (ISRM, 1978).
- Unconfined uniaxial compressive strength was estimated through Point load index tests performed on solid cylinders (Figure 3.1.B), in complete adherence to ISRM standard (ISRM, 1978; ISRM, 1985).

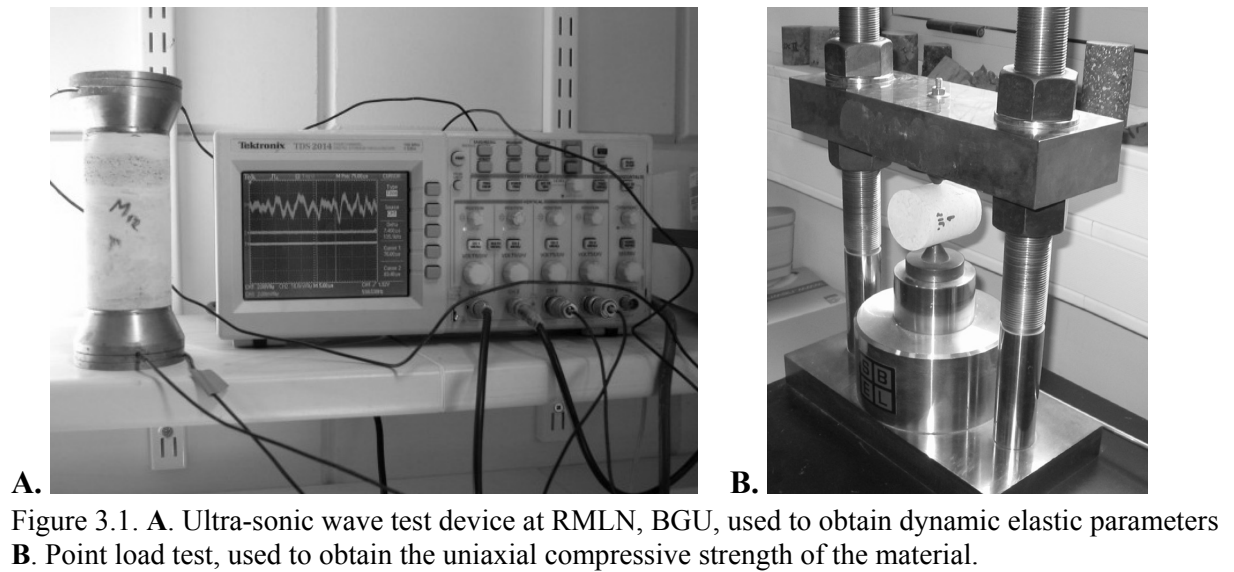


Figure 3.1. **A.** Ultra-sonic wave test device at RMLN, BGU, used to obtain dynamic elastic parameters **B.** Point load test, used to obtain the uniaxial compressive strength of the material.

Table 3.1. Mechanical properties obtained in the lab from the original building blocks taken from the studied sites.

Mechanical property	Avdat	Mamshit	Nimrod Fortress
Lithology and Formation	Matred limestone	Hazera limestone	Hermon limestone
Density ( $\text{Kg/m}^3$ )	2555	1890	2604
Porosity (%)	5	30-38	3.5
Dynamic Young's modulus (GPa)	54.2	16.9	-
Dynamic Poisson's ratio	0.33	0.37	-
Dynamic Shear modulus (GPa)	20.3	6.17	-
Point load Index (MPa)	-	2.64	3.6
Uniaxial compressive strength (MPa) – standard	-	66	90

### 3.2 Shear strength of interfaces

Interface friction was obtained from direct shear tests, which were performed using a hydraulic, close loop servo-controlled direct shear system (Product of TerraTek Systems Inc.), described in Hatzor et al. (2004). Three segment direct shear tests were performed on each sample, under a

constant shear displacement rate of 0.025 mm/s and under an imposed constant normal stress condition.

Results from the direct shear tests of the Avdat samples are presented in Figs. 3.3 and 3.4. The results yield linear failure envelope in  $\tau$ - $\sigma$  space with peak friction angle of  $30^\circ$ . The residual strength values yield a linear residual strength criterion with  $\phi_r=28^\circ$ .

Direct shear test results for the Mamshit samples are presented in Figs. 3.5 and 3.6. After shear displacement of about 0.25mm, the interface exhibits plastic deformation with no stress drop. Because the Mamshit rocks are more porous and much weaker than the Avdat rocks friction along interfaces in this material seems to depend on the magnitude of the normal stress. Jaeger and Cook (1979) suggest an alternative method for inclined asperity surfaces, in which the *dynamic* friction coefficient ( $\mu^*$ ) is plotted against  $\sigma$  ( Figure 3.6 ). According to this alternative method, the friction angle is in inverse proportion to the normal stress on the interface, and Figure 3.6 suggests that the peak friction angle for low normal stresses is larger than  $30^\circ$  ( $\mu > 0.57$ ).

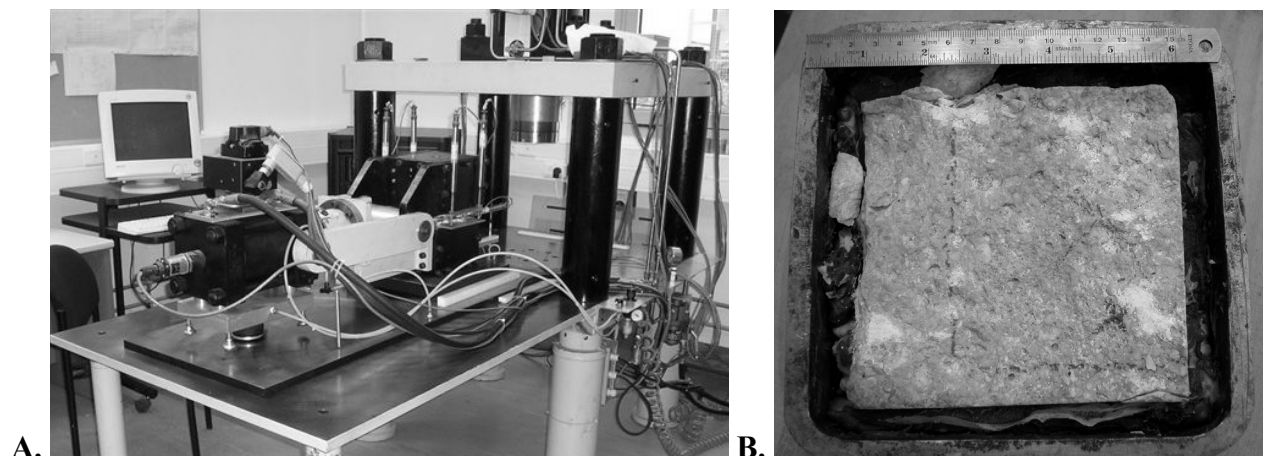


Figure 3.2. **A.** The servo-controlled direct shear system, the sample is ready to enter the load frame, **B.** A sample from Avdat after a test, the surface roughness is noticed by the white points, first to be sheared.

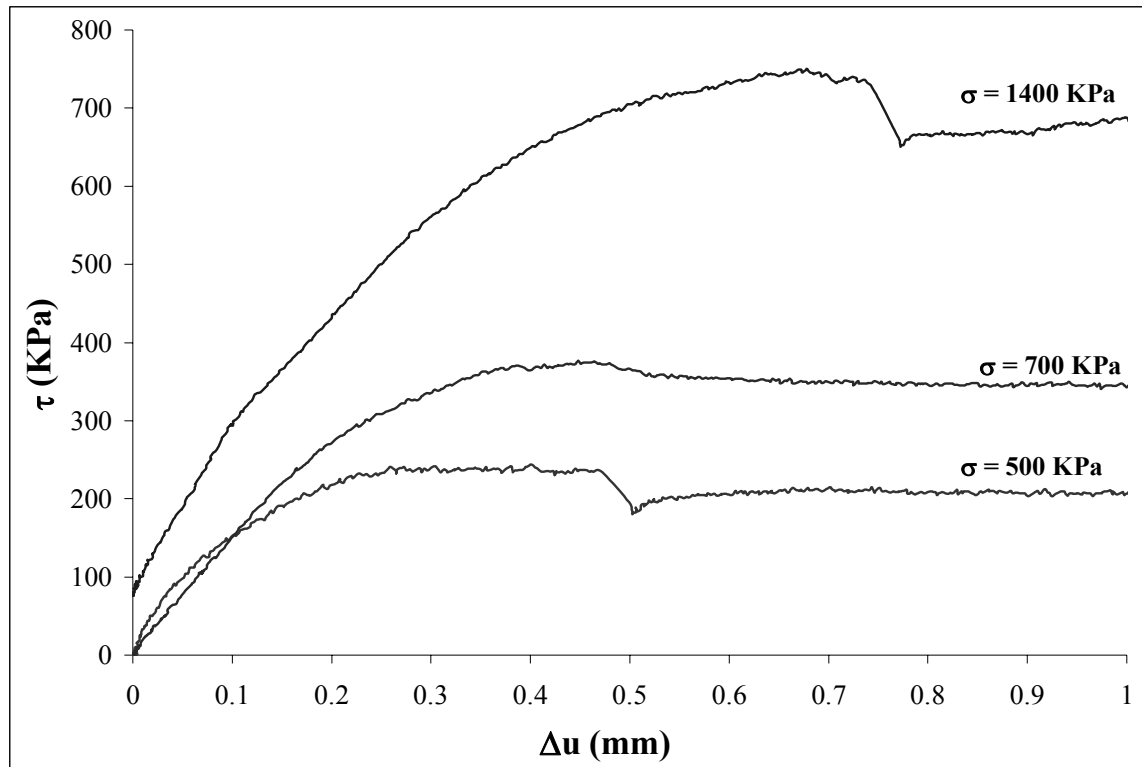


Figure 3.3. Results for a direct shear test on a sample from Avdat, under three different normal stresses.

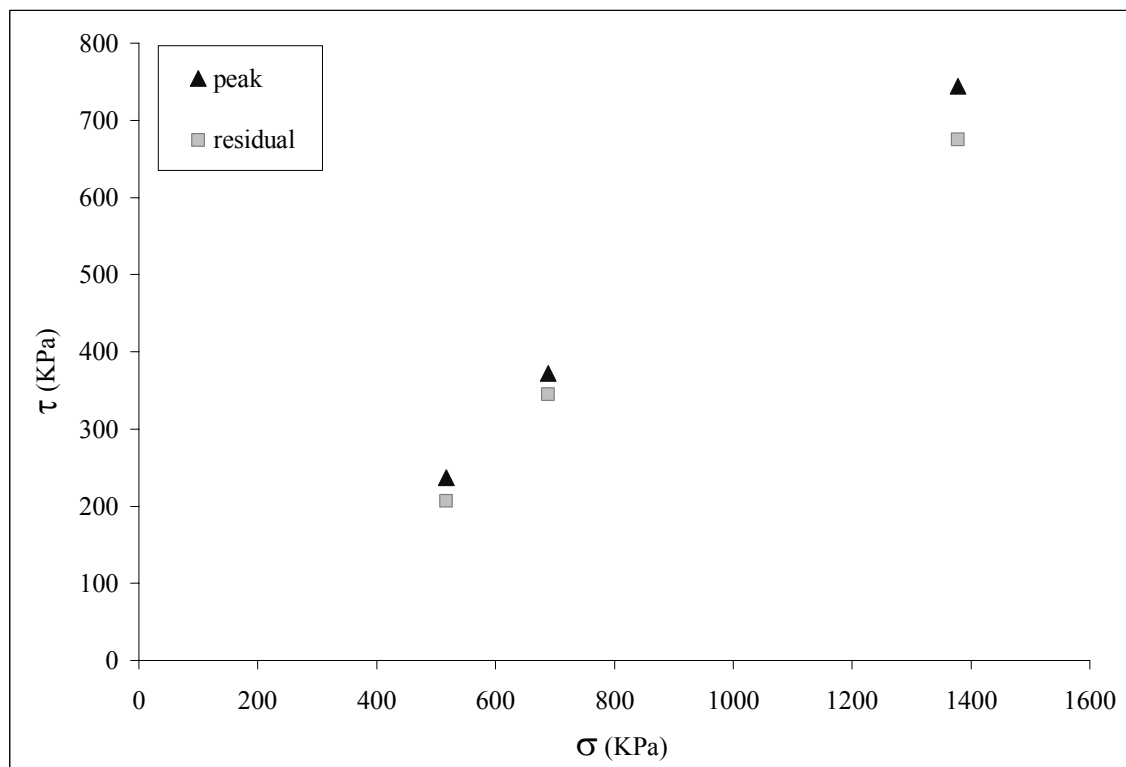


Figure 3.4. Results of the direct-shear tests on the Avdat samples, shear stress plotted versus normal stress. Even though the true behavior of the failure envelopes is not necessarily linear, a linear trend yields the following results:  $\mu=0.57$ ,  $\phi=30^\circ$  for the peak shear strength and  $\mu=0.53$ ,  $\phi=28^\circ$  for the residual strength.

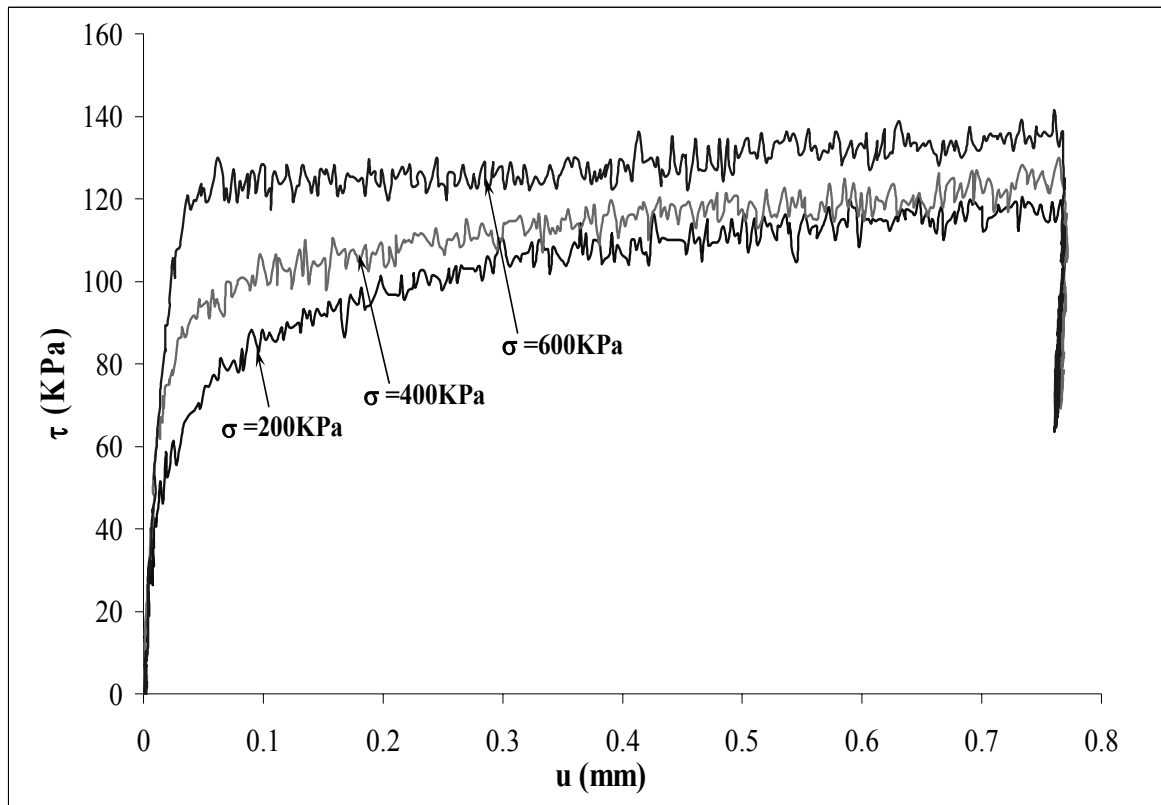


Figure 3.5. Results for a direct shear test on a sample from Mamshit, under three different normal stresses.

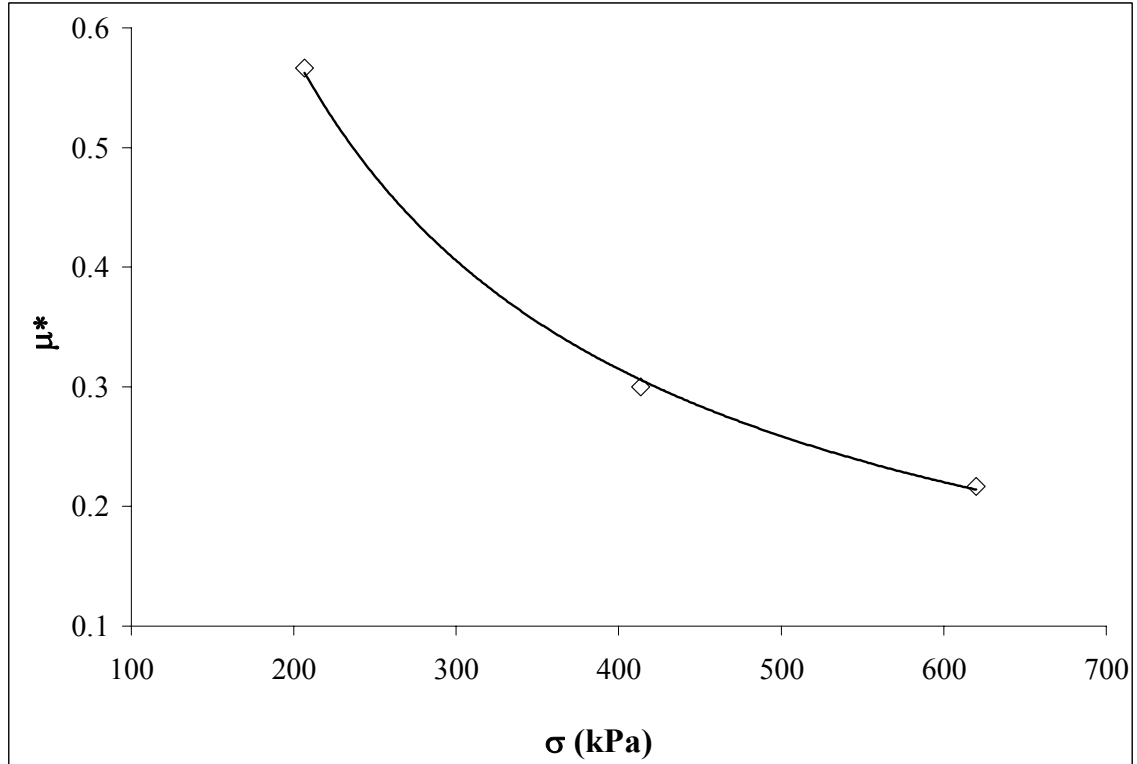


Figure 3.6. Results of the direct-shear tests on the Mamshit samples, dynamic friction coefficient plotted versus normal stress.

### 3.3 Summary

The mechanical parameters that were ascribed to the hewn stones of all three case studies, both in the analytical analyses and the numerical ones, are presented in Table 3.1. The friction angle was taken as  $35^\circ$  for all three cases.

Where the parameters for the surrounding wall are different than the ones for the embedded structure, they are mentioned and discussed in the relevant chapter.

## 4 DDA validation

Since DDA has been successfully validated by many researchers, comparing it with field data, physical models, and analytical solutions (MacLaughlin and Doolin, (2005)), validation studies in this chapter were performed for calibration purposes only, all with respect to analytical solutions. Section 4.1 repeats cases that have been validated before, yet sometimes with greater accuracy. Section 4.2 is a new development of a validation that has never been performed before. In Validations of simple cases where DDA results are compared to analytical solutions, the analysis is fully dynamic ( $k_{01} = 1$ ). Where the physical problem complicates, and the number of blocks increases, it was found that a certain degree of energy dissipation is required (Hatzor et al., 2004; Tsesarsky et al., 2005), usually 1-2% in problems with up to 500 blocks (see section 5.2.3). This might result from physical energy losses, other than friction, that are not modeled in DDA (such as heat generation, block edge damage, etc.).

### 4.1 Block on an Incline

Block displacement as a function of time has been studied by many researchers, since a well known analytical solution for displacement of a point mass is readily available. The case of a single block on an incline is perhaps the most studied of all validation cases (MacLaughlin and Doolin, 2005).

#### 4.1.1 *Gravitation only*

For a single block resting on a plane inclined at an angle  $\alpha$  with friction along the interface  $\phi$ , and subjected to gravitational acceleration  $g$ , the analytical solution for displacement  $d$  as a function of time  $t$  is given by:

$$d(t) = \frac{1}{2}at^2 = \frac{1}{2}(g \sin \alpha - g \cos \alpha \tan \phi)t^2 \quad (4.1)$$

The inclination of the modeled plane is  $28^\circ$  (Figure 4.1), and five friction angles are studied,  $\phi = 5^\circ, 10^\circ, 15^\circ, 20^\circ, 25^\circ$ . The accumulated displacements are calculated up to 1 sec.

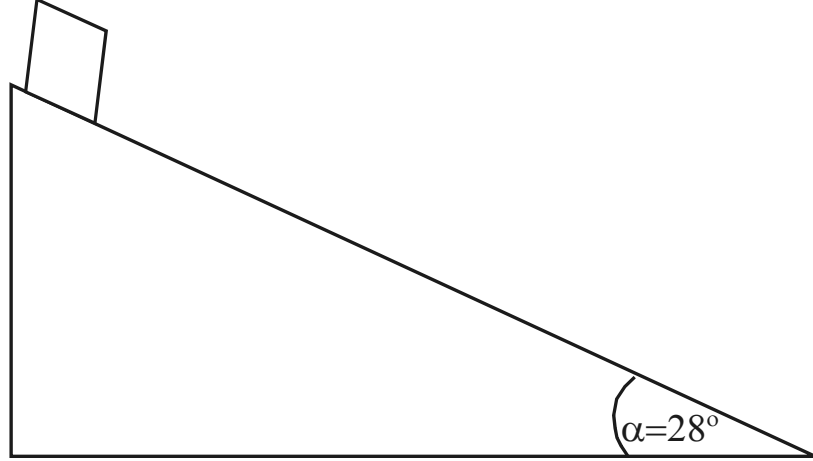


Figure 4.1. The model used for DDA validation of a block sliding on an incline.

Comparison between analytical and DDA solutions is shown in Figure 4.2. Block displacement during the elapsed time is much larger with  $5^\circ$  friction angle than with higher angles approaching the inclination angle of the plane, as expected. In addition, the agreement between the analytical and numerical solutions for a given time step is larger for the lower friction angles. The agreement between the analytical and numerical solutions is determined by the numerical error, which is defined in a conventional manner:

$$E_N = \left| \frac{d - d_N}{d} \right| \cdot 100(\%) \quad (4.2)$$

where  $d$  and  $d_N$  are analytical and numerical displacements respectively.

For a time step size of 0.002 sec., the largest errors with a  $5^\circ$  friction angle and a  $25^\circ$  friction angle are 0.05% and 78% (still only 0.5mm) respectively. After halving the time step size to 0.001sec. the largest error for a  $25^\circ$  friction angle reduces by an order of magnitude to 7.7%.

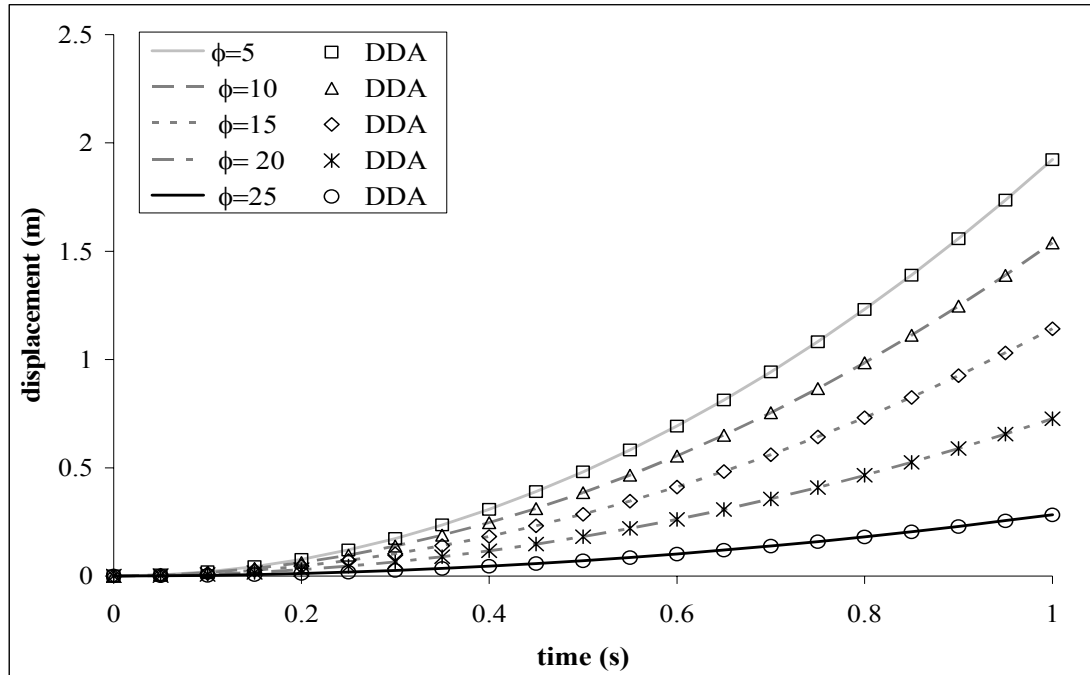


Figure 4.2. Block displacement vs. time for the case of a block on an incline – gravitational loading only. Comparison between analytical (lines) and DDA (symbols) solutions.

The results demonstrate a well known issue in numerical methods, that while time step size has no affect on the analytical solution, the numerical solution is very sensitive to these differences. Although implicit methods like DDA allow for relatively large time steps, as mentioned in Chapter 2, reduction of the time step size still increases the accuracy of the solution.

#### 4.1.2 Dynamic loading

The case of a single block on an inclined plane, subjected to both gravitational load and horizontal sinusoidal acceleration, has first been examined by Hatzor and Feintuch (2001) for an acceleration function consisting of a sum of up to three sines. Hatzor and Feintuch found that the accuracy of DDA prediction was within 15% of the analytical solution, provided that the numerical control parameters  $g_1$ ,  $g_2$  were carefully optimized, without application of any damping <sup>(1)</sup>.

(1) Note that in the analytical solution published by Hatzor and Feintuch (2001), the resisting force during sliding for  $a_t > a_{yield}$  was neglected in the double integration.

Tsesarsky et al. (2005) broadened the investigation and compared DDA results with physical results of shaking table experiments, for which an introduction of 1.5% damping was found to reduce the error significantly.

In this section, the presented validation is for an acceleration function of one sine only.

The complete analytical solution is displayed in section 2.1.2. It was shown that the displacement  $d$  of the block at any time  $t$  is determined by double integration on the acceleration, with  $\theta$  as reference datum:

$$d = \int_{\theta}^t v = \iint_{\theta} a = g \left[ (\sin \alpha - \cos \alpha \tan \phi) \left( \frac{t^2}{2} - \theta t \right) \right] + \frac{ag}{\omega^2} \left[ (\cos \alpha + \sin \alpha \tan \phi) (\omega \cdot \cos(\omega \theta)(t - \theta) - \sin(\omega t) + \sin(\omega \theta)) \right] \quad (4.3)$$

where  $\theta$  is the elapsed time from beginning of shaking until yield acceleration is reached and block motion ensues.

The inclination of the modeled plane is  $20^\circ$ , as shown in Figure 4.3. Three friction angles are studied:  $\phi = 20^\circ, 22^\circ, 30^\circ$ , and the accumulated displacements are computed.

Figure 4.5 displays the case of  $\alpha = \phi = 20^\circ$ , for which yield acceleration is zero, and displacement is calculated for more than a full cycle of the input sinusoidal earthquake. The higher friction angles,  $\phi = 22^\circ, 30^\circ$  have  $\theta = 0.089$  seconds and  $0.1802$  seconds respectively, which complicates the analytical solution after half a cycle. For that reason, the accumulated displacements in Figure 4.6 for  $\phi = 22^\circ$  and  $30^\circ$  are calculated up to  $\sim 2.5$  seconds.

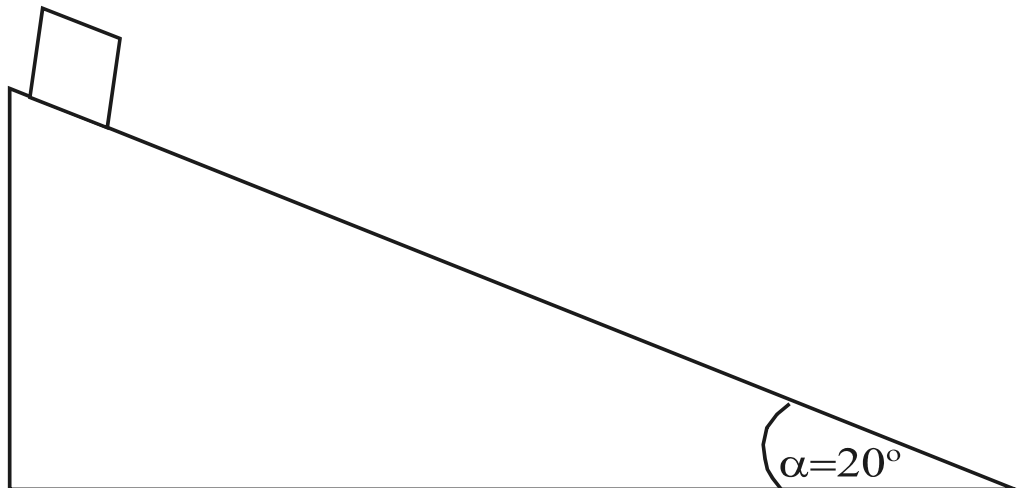


Figure 4.3. The model used in DDA for the dynamic validation of a block sliding on an incline. The driving forces act directly on the sliding block; the inclined block is fixed in place.

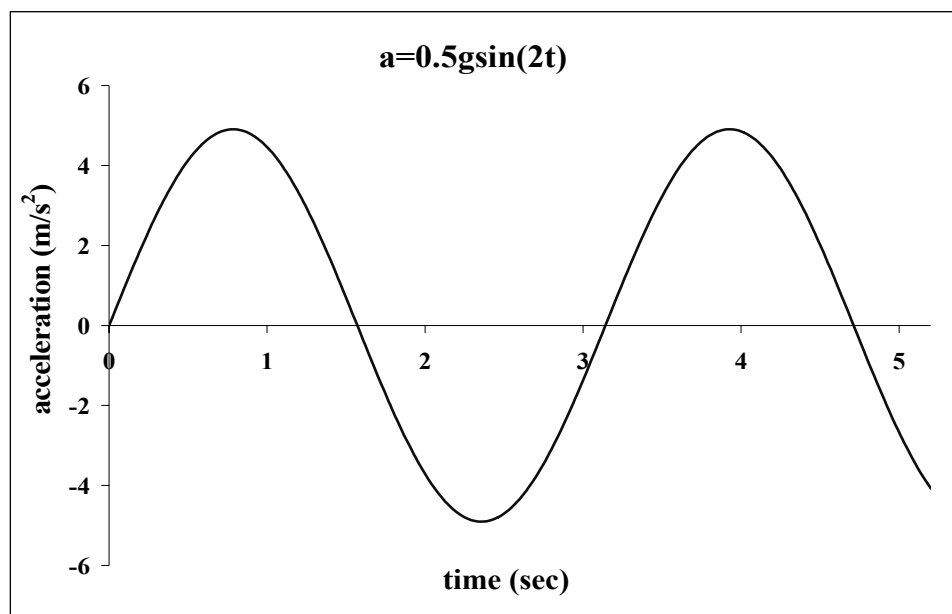


Figure 4.4. The input acceleration function used for the dynamic validation of a block sliding on an incline.  $A=0.5$ ,  $f=1/\pi$ .

Figures 4.5 and 4.6 present a comparison between DDA and analytical solutions. The obtained agreement is remarkable, with maximum displacement errors ranging between 0.2% and 0.9%.

The time-step size is kept constant in all DDA runs, 0.002 sec.

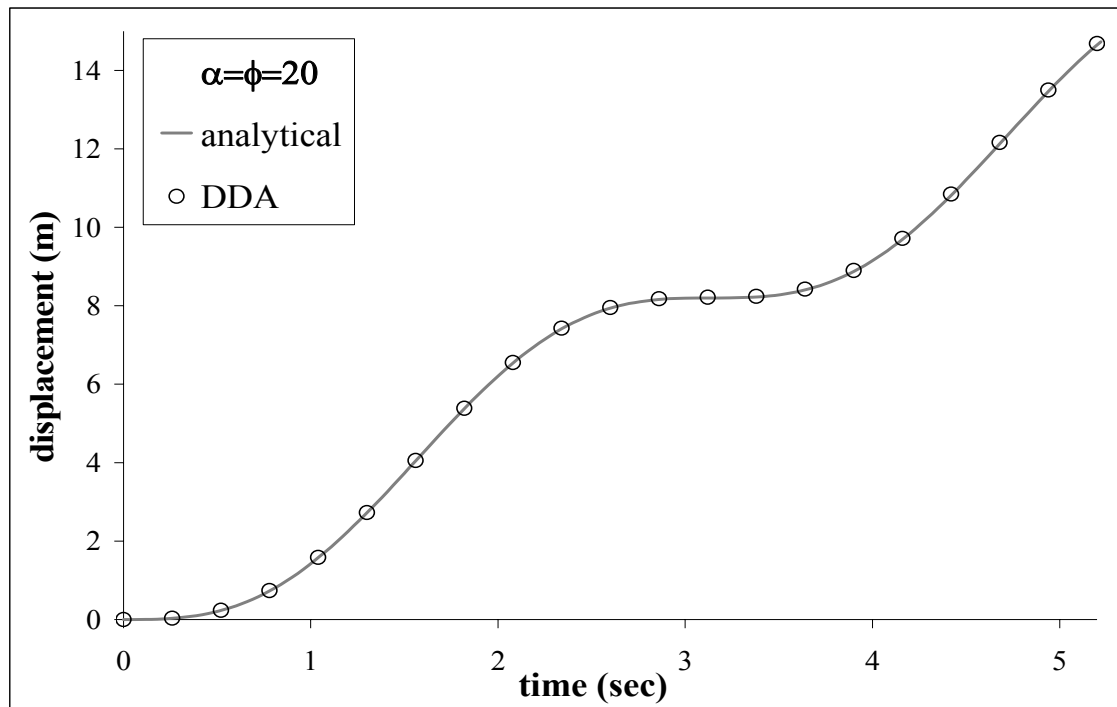


Figure 4.5. Block displacement versus time, for the dynamic case of a block on an incline,  $\alpha = \phi = 20^\circ$ . Comparison between analytical (solid line) and DDA (symbols) solutions.

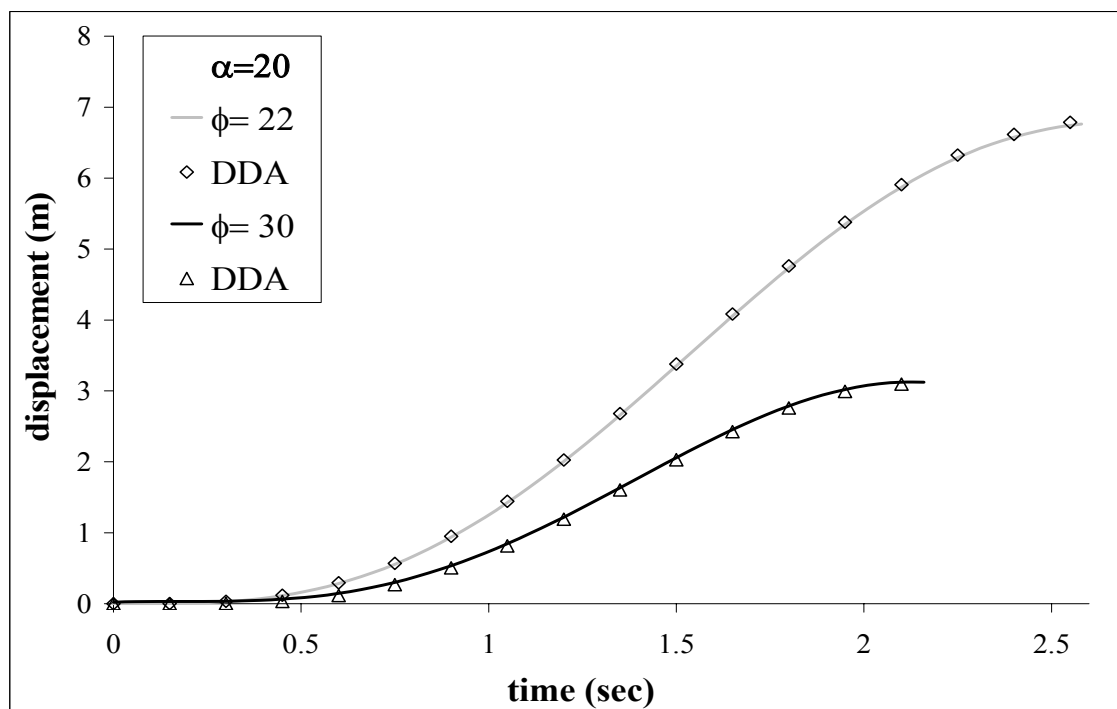


Figure 4.6. Block displacement versus time, for the dynamic case of a block on an incline,  $\alpha < \phi$ . Comparison between analytical (solid line) and DDA (symbols) solutions.

## 4.2 Block response to induced displacements in the foundation

DDA allows application of time-dependant displacements to “fixed” points in the mesh which are defined and positioned by the user. The intention is to use this feature of DDA to simulate seismic ground motions at the foundation of the structure and to investigate the response of a masonry structure, later in this work.

The purpose of this validation is to examine the accuracy of this DDA feature by comparing it to an analytical solution for the response of a single block resting on a block which is subjected to a time-dependant displacement input function.

The studied block system consists of three blocks: a fixed foundation block (no.0), the induced block (no.1), and the responding block (no.2) (see Figure 4.8). The displacement function for Block 1 is induced in a form of a cosine function, starting from 0 (Figure 4.7):

$$d(t) = D(1-\cos(2\pi\omega t)) \quad (4.4)$$

and the corresponding response of Block 2 is investigated.

For the case described in section 2.1.3 the analytical solution must be computed in time steps, since the relative velocity and the direction of the force are dependant on each other. The analysis was performed by Matlab 7.0, and the computation model is presented in Appendix 1.

The analytical solution is restricted to one degree of freedom, which in this case is one directional sliding of Block 2 on Block 1. In DDA however, the mode of failure of a blocky system is a result of the analysis, where each block has 6 degrees of freedom.

In order to compare between DDA and the analytical solution, the mode of failure of the analyzed block in DDA has to be constraint to horizontal sliding only. One way for constraining DDA to one degree of freedom is by generating a block system in which Block 2 has limited motion options. Three different DDA block systems are examined (displayed in Figure 4.8), together with two different sets of numerical parameters for model optimization.

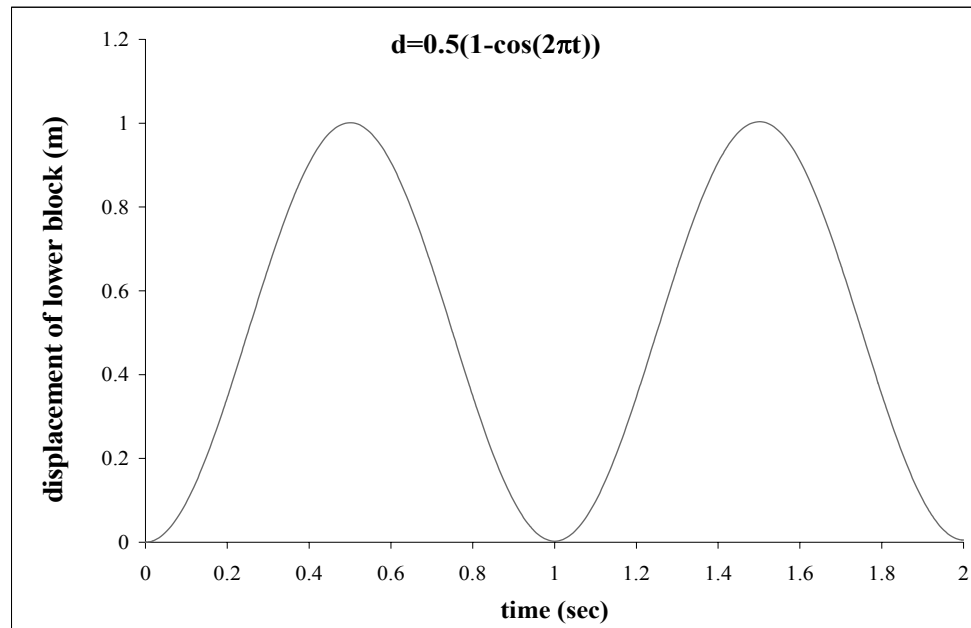


Figure 4.7. The input displacement function used for the dynamic validation of a block on a displaced block.  $D=0.5$ ,  $f=1$ .

The three block models are subjected to a displacement function of  $D=0.5\text{m}$  and  $f=1\text{Hz}$ , and results are presented in Figure 4.9. The best agreement with the analytical solution (by Matlab) is obtained by model 3 and the set of parameters  $g_1=0.0075$ ,  $g_2=0.002$ . In model 3 the responding block has the most slender geometry and therefore its preferred displacement mode is one dimensional sliding with no rotation or bouncing, namely one degree of freedom, as in the analytical solution. Since the forces are subjected to the block centroid, a block with different geometry experiences moments that lead to more complicated movements. Therefore, model 3 is used in further analysis.

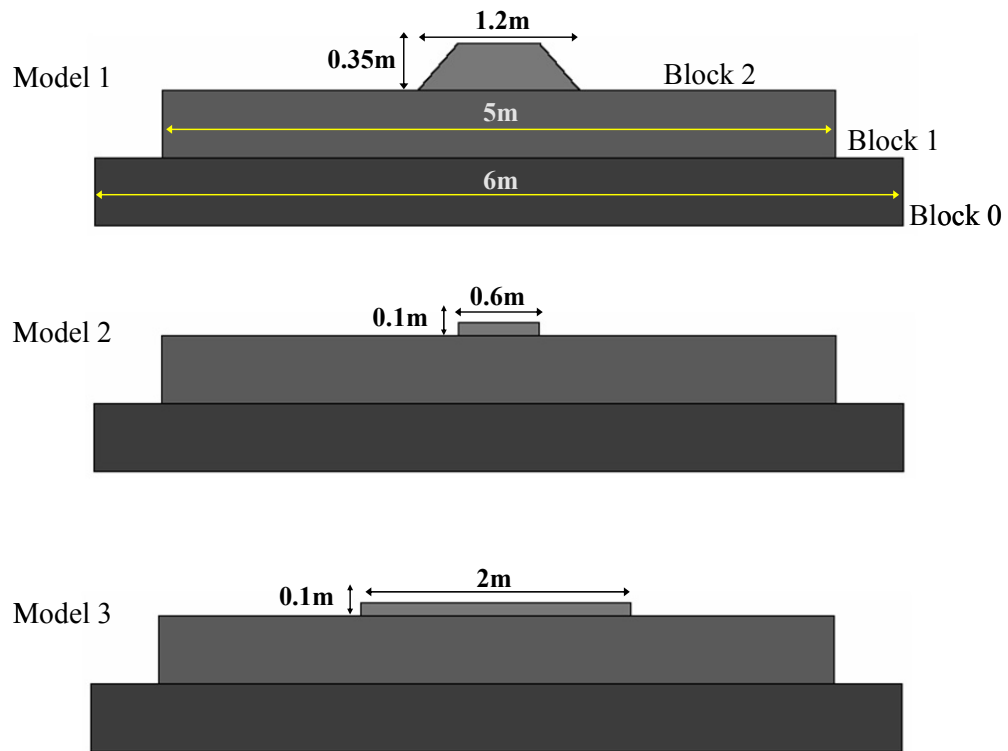


Figure 4.8. Three DDA block systems, examined for mode of failure. The number of the block is indicated on its right side. Model 3, with block 2 being the most slender, was found to obtain best agreement with the analytical solution.

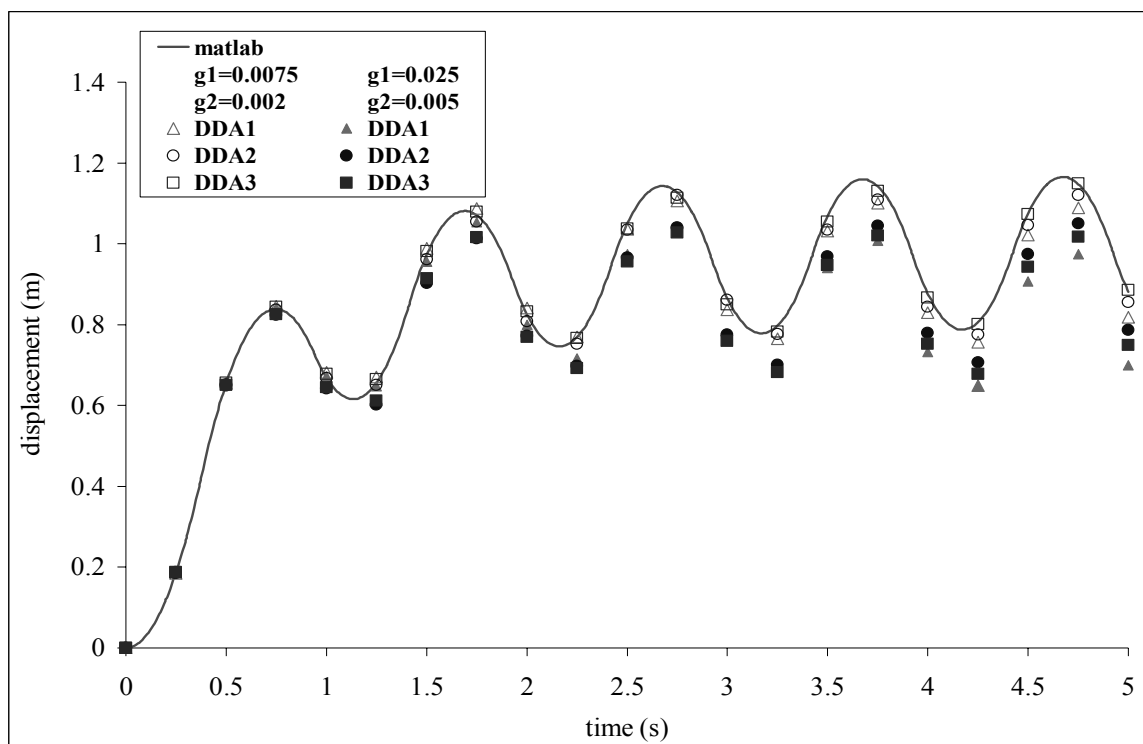


Figure 4.9. Response of Block 2 to displacement input of  $D=0.5\text{m}$ ,  $f=1\text{Hz}$ . Comparison between three DDA models (model 1 as triangles, model 2 as circles, and model 3 as rectangles), and two sets of numerical parameters (empty symbols –  $g1=0.0075$ ,  $g2=0.002$ . full symbols –  $g1=0.025$ ,  $g2=0.005$ ).

A sensitivity analysis for amplitude, frequency and friction was performed. Accumulating displacement of Block 2 was calculated, and comparison between DDA and Matlab results are presented in Figures 4.10-4.12:

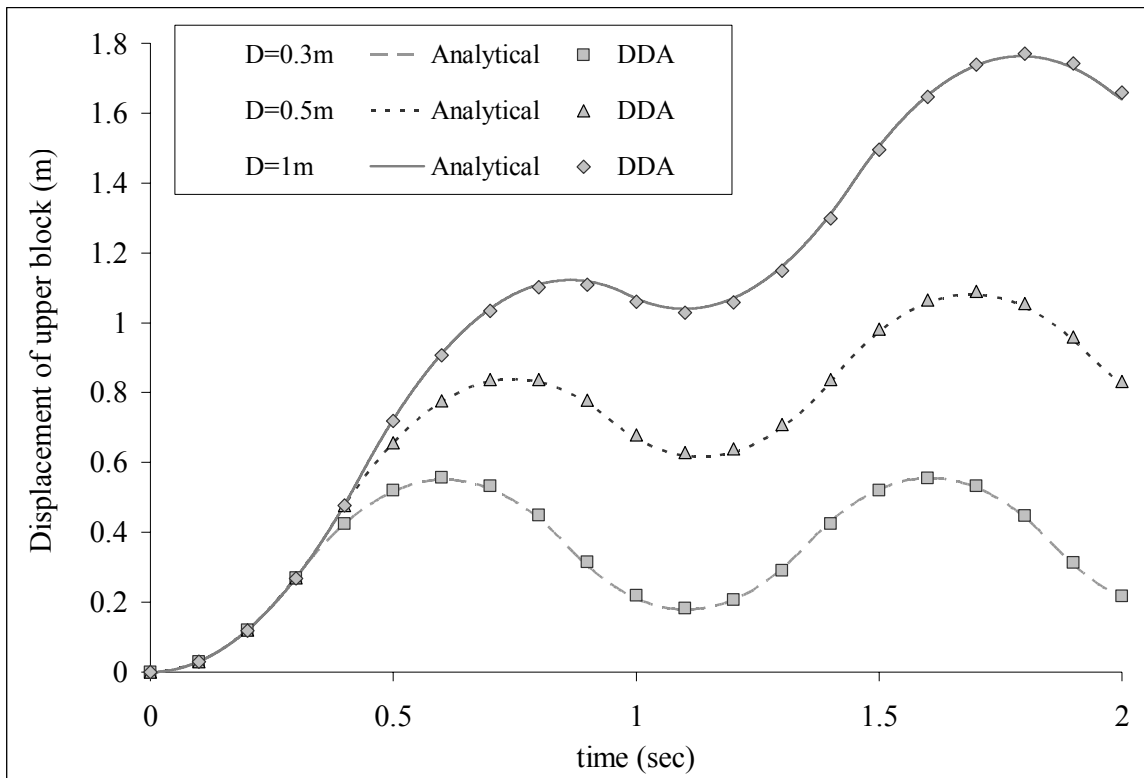


Figure 4.10. Response of Block 2 to displacement input of  $f=1\text{Hz}$ . Comparison between analytical (line) and DDA (symbols) solutions for different amplitudes of motion.

Figure 4.10 presents the response of Block 2 to changing amplitudes of motion ( $D$ ), with constant input frequency of 1Hz. The accumulating displacement is in direct proportion to the amplitude, as expected. Note that the three displacement curves follow the periodic behavior of the induced displacement function ( $T = 1 \text{ sec.}$ ), and that divergence between curves starts after 0.25 sec., where the displacement function (Figure 4.7) has an inflection point.

Figure 4.11 presents the response of Block 2 to changing frequencies. Although the displacement amplitude is constant (2cm), the acceleration amplitude ( $A=D\omega^2$ ) increases with increasing

frequency, according to the double integration of Eq. 4.4. The displacement curves follow the different periods of motion, and the accumulating displacement is in direct proportion to the amplitude of the acceleration.

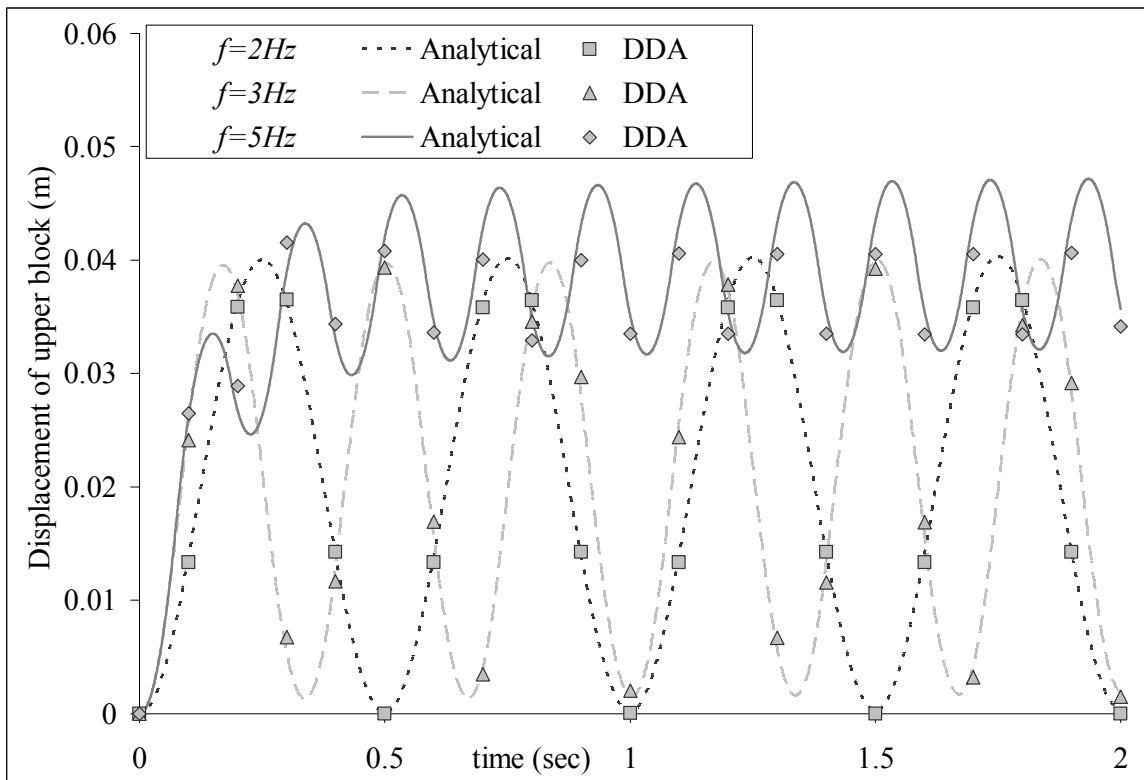


Figure 4.11. Response of Block 2 to displacement input of  $D=0.02\text{m}$ . Comparison between analytical (line) and DDA (symbols) solutions for different frequencies of motion.

Figure 4.12 presents the response of Block 2 to changing friction coefficients, with a constant displacement function of  $D=0.5\text{m}$ ,  $f=1\text{Hz}$  (Figure 4.7). Note that the accumulating displacement is in direct proportion to the friction coefficient up to 0.5sec., where the induced displacement function changes direction. After that point the accumulating displacement of  $\mu=0.6$  is larger than  $\mu=1$ , since the high friction works in both directions: forward and backward. Note that  $\mu=0.1$  and  $\mu=0.6$  follow the periodic behavior of the displacement function, whereas  $\mu=0.6$  is in a delay of about 0.25sec.

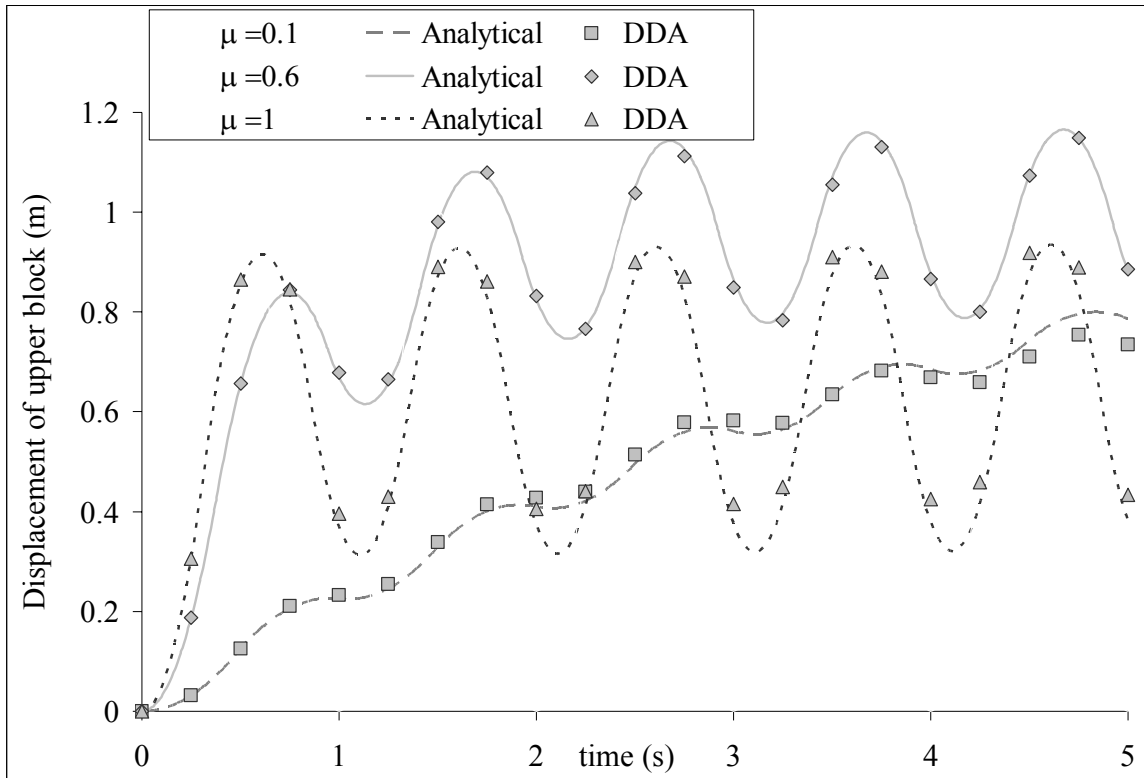


Figure 4.12. Response of Block 2 to displacement input of  $D=0.5\text{m}$ ,  $f=1\text{Hz}$ . Comparison between analytical (line) and DDA (symbols) solutions for different friction coefficients.

In general, a remarkable agreement can be seen in all three figures. DDA follows the analytical results in all cases, with changing friction coefficients, amplitudes, and frequencies of motion.

### 4.3 Summary and Conclusions:

The validation procedure shows that the DDA method is accurate, and a good agreement was obtained with respect to analytical solutions for various problems. Three driving mechanisms were used: gravitation load, time-dependant acceleration function, and time-dependant displacement function. The block response was examined for all cases

It was found that:

1. Since analytical solutions represent a superficial approximation of reality, they are often restricted in degrees of freedom and energy dissipation mechanisms, and represent an idealized case. In validation with respect to analytical solutions, these restrictions should be

identified, and the DDA model should accommodate such restrictions for a comparison to be meaningful.

2. In the validation study presented here introduction of damping was un-necessary, as should be the case for a validation with respect to analytical solution.
3. DDA numerical control parameters ( $g_1$ ,  $g_2$ ) should be carefully optimized in all analyses, including simple cases of two or three blocks.
4. DDA exhibits sensitivity to variations in input parameters such as friction angle and loading function parameters such as amplitude and frequency, with out any loss of accuracy.

## 5 Case studies

### 5.1 Masonry Arch - results from Mamshit

#### 5.1.1 Background

##### Geography and Geology

The ruins of Mamshit are located on the road leading from Beer-Sheva to the Arava junction (Figure 1.2). At a height of 475m above sea level, the city lies on the bank of the Mamshit river canyon, at the edge of the Hatira mountain range. The rocks on which the city is built are mostly limestones from the middle Cenomanian (Hazera formation).

##### Archaeology and History

The city of Mamshit was the sixth and last Nabatean city built in the Negev, on the trade route between Petra, Hebron, and Jerusalem. Mamshit is the most eastern and isolated of the Nabatean cities in the Negev, perhaps which is why it is the only one surrounded by a wall (Negev, 1988b). By the middle of the 1st century AD the Nabatean trade diminished, and the inhabitants turned to farming. Mamshit, also known as Mampsis or Curnub, was a very wealthy city thanks to the breeding of Arabian race horses. Two impressive churches were built as Christianity arrived at the second half of the 4<sup>th</sup> century AD, though not long afterwards, before the year 500 AD, the city was conquered by the Arabs, even before appearance of Islam (Negev, 1988b).

Mazor and Korjenkov (2001) reported over 200 cases of earthquake patterned damage throughout the city. Evidence point to a strong earthquake at the end of the Roman period, i.e. 4<sup>th</sup> century AD. The city was rebuilt at the Byzantine period, and new buildings were added, which, too, were damaged by a severe earthquake probably at the end of the 7<sup>th</sup> century AD. This earthquake is probably the major event which ended the Byzantine settlement in the Negev, and is evident in the ruins of Avdat and Shivta as well (Mazor and Korjenkov, 2001).



Figure 5.1. General plan of the city of Mamshit (Negev, 1988a). The black arrow points to building IX.

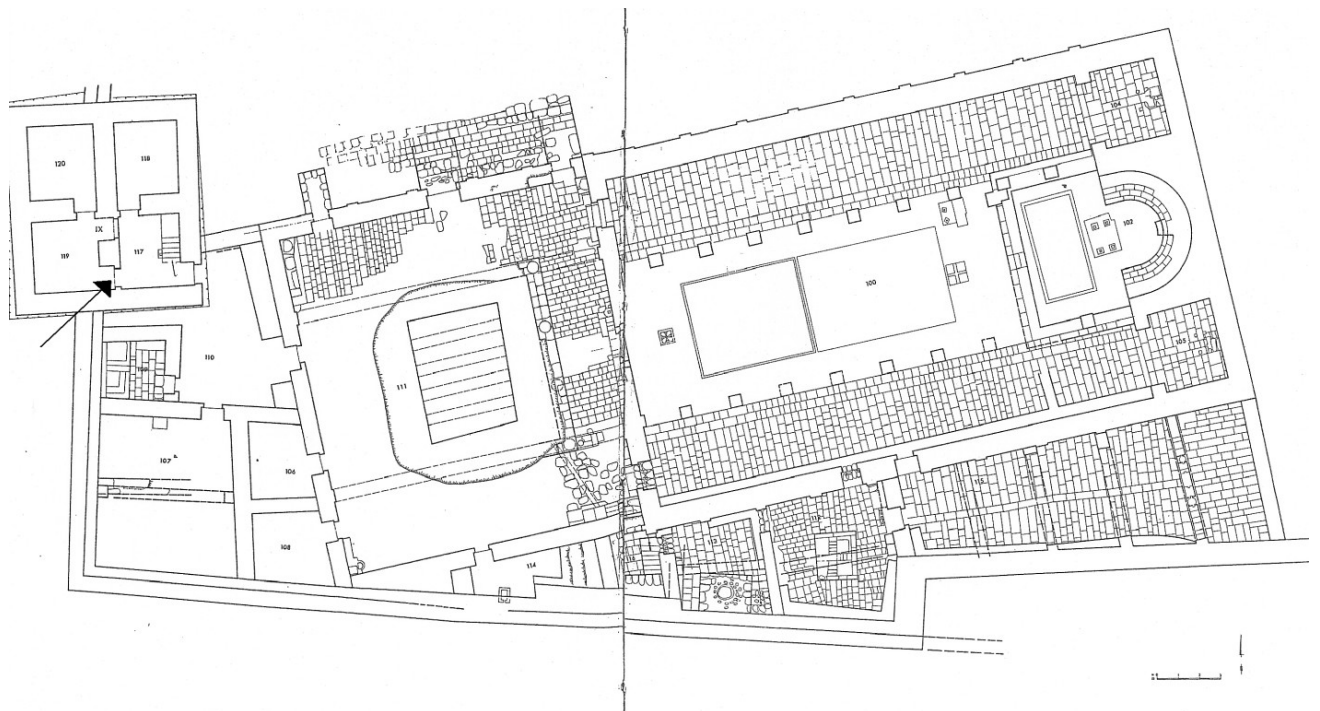


Figure 5.2. Detailed map of the eastern church (Negev, 1988a). The black arrow points to the location of the deformed arch in building IX.

A unique structural failure is noticed in a tower at the corner of the Eastern Church (building IX in Figure 5.2), where a key stone has slid downwards out of a still standing arch.

### The analyzed structure

Building IX is the earliest in the entire complex of the Eastern Church. It was probably used originally to guard the decent to the Mamshit wadi, and later was incorporated into the church complex, functioning as a bell tower (Negev, 1988a). The tower measured 8.6m x 9.5m above the foundation courses, constructed of one or more layers of hard, hammer-dressed stones, and rose to a height of 8-10m. The outer walls and the arched doors were built of excellent ashlar, while on the inside of the tower the walls were built in regular courses of large squared blocks of hard limestone, with an occasional filling of smaller stones and earth cement (Negev, 1988a), (Figure 5.3.A). Detailed mapping of the arch is presented in Appendix 2.



Figure 5.3. The deformed arch at Mamshit. **A.** The arch is embedded in a very heterogenic wall. **B.** The Keystone has slid 4cm downwards while the rest of the arch remained intact.

#### 5.1.2 Analytical solution

Following the equations presented in section 2.1.4, the limit horizontal thrust values for the semi circular arch at Mamshit are calculated. As mentioned before, the analytical solution is restricted to a free-standing arch, therefore  $q=0$ . Other geometrical parameters as derived from field

mapping are:  $R = 0.61\text{m}$ ,  $r = 0.44\text{m}$ ,  $s = 0.34\text{m}$ . The unit weight of the rock is  $w = 18.54\text{kN/m}^3$  (Table 3.1).

The parameters are substituted into the equations at section 2.1.4 and plots of horizontal thrust versus hinge angle  $\theta$  are presented in Figure 5.4 and Figure 5.5.

Results for the lower collapse mechanism, obtained from Figure 5.4, are a minimum horizontal thrust of  $0.1623\text{kN}$  and an angle of  $0.45\text{rad}$  ( $26^\circ$ ). Results for the upper collapse mechanism, obtained from Figure 5.5, are a maximum horizontal thrust of  $1.346\text{kN}$  and an angle of  $1.55\text{rad}$  ( $88^\circ$ ).

As explained in Section 2.1.4, the strongest possible force required to turn the arch into a mechanism is:  $H_{\max} - H_{\min} = 1.35 - 0.16 = 1.18\text{kN}$ . Dividing the obtained thrust by the mass of

the arch (only upper 7 blocks, without abutments), which is  $\frac{2 * P}{g} = 1231\text{Kg}$ , provides a yield

acceleration of:  $a_{\min} = 0.96\text{m/s}^2 = 0.1g$ . The implications of this result are that only pseudo-static tensional or compressional inertia forces higher than  $m * 0.1g$ , will initiate a failure mechanism.

Since these values refer only to a free-standing arch, their relevance to the studied failure events in the field is limited because in all cases the studied arc is embedded within a massive masonry wall. Nevertheless, the pseudo-static solution provides an insight into the behavior of a masonry arch and presents some constraints, albeit limited, on numerical results.

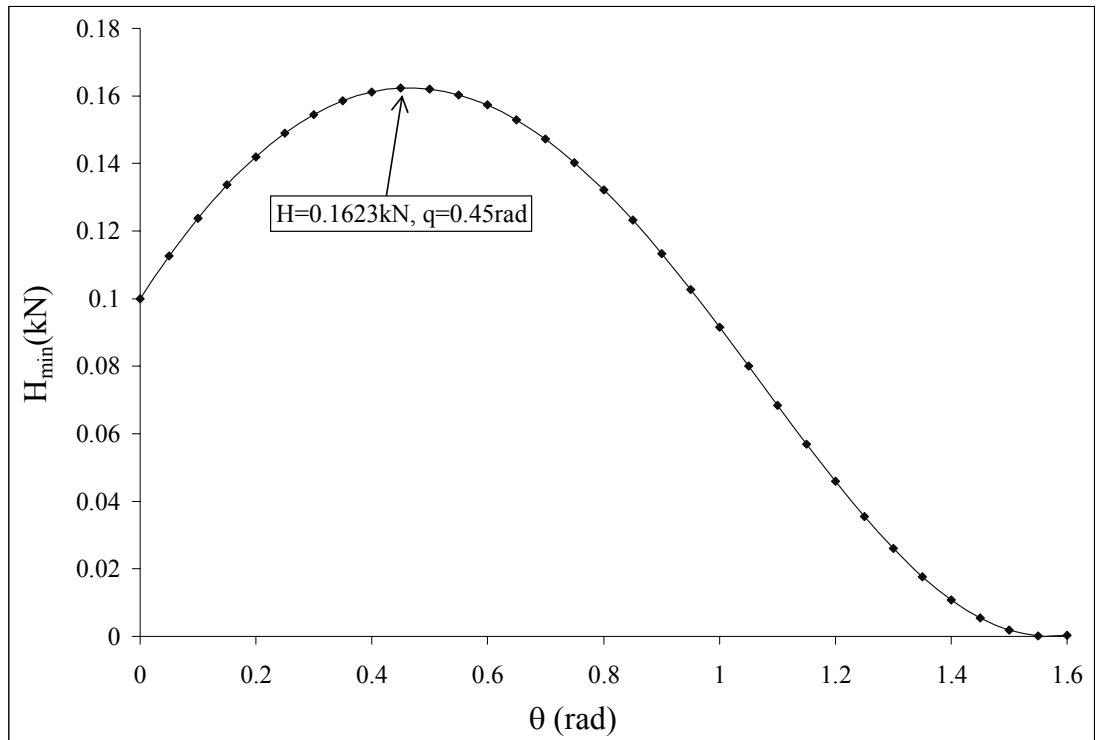


Figure 5.4.  $H_{\min}$  versus  $\theta$ . The maximum point is the minimum horizontal thrust at stability, and the associated angle of the hinge at the haunch for the lower collapse mechanism.

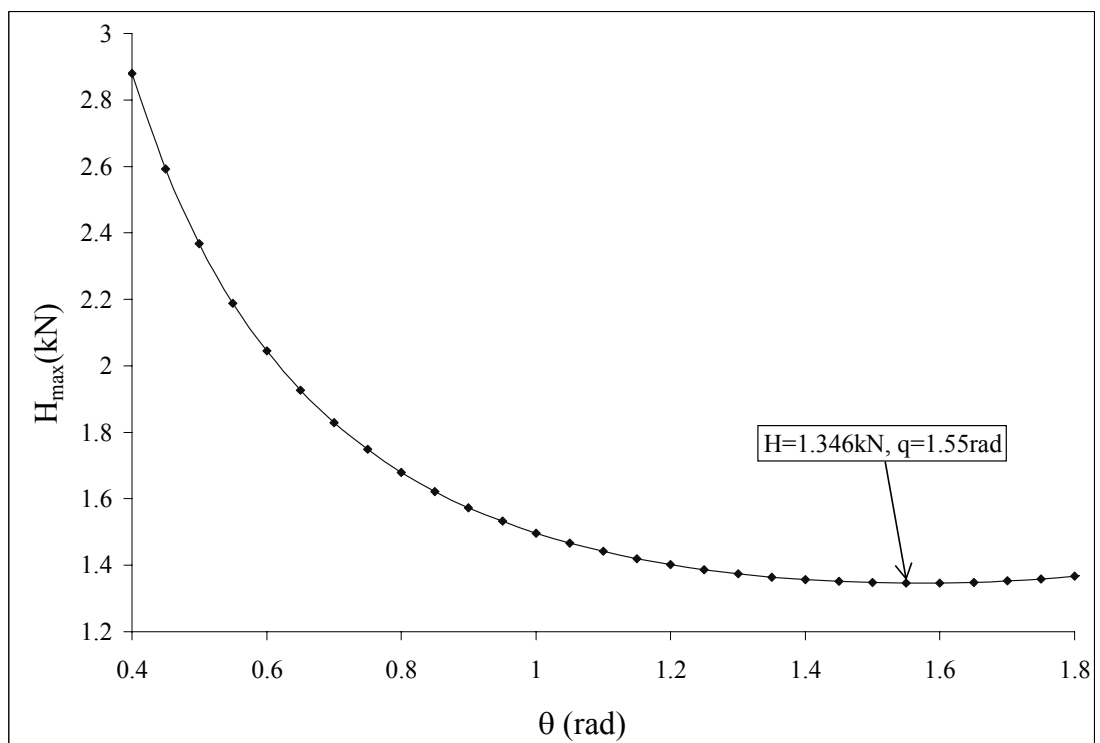


Figure 5.5.  $H_{\max}$  versus  $\theta$ . The minimum point is the maximum horizontal thrust at stability, and the associated angle of the hinge at the haunch for the upper collapse mechanism.

### 5.1.3 Numerical solution

The numerical analysis of the arch at Mamshit was performed in two stages:

1. Shaking of a free standing arch - to follow the development of the failure mechanism and compare with results of analytical solution.
2. Shaking of a fully embedded arch within a heterogenic wall - to obtain ground motion parameters most likely to cause the observed failure in the site.

#### Free standing arch

The block system for the free standing arch was generated using program DC of DDA, and the mechanical parameters inserted to program DF are the ones obtained in the laboratory (Table 3.1). The model was designed to be loaded with induced time-dependant displacements in the foundation block only, based on the validation study presented in section 4.2.

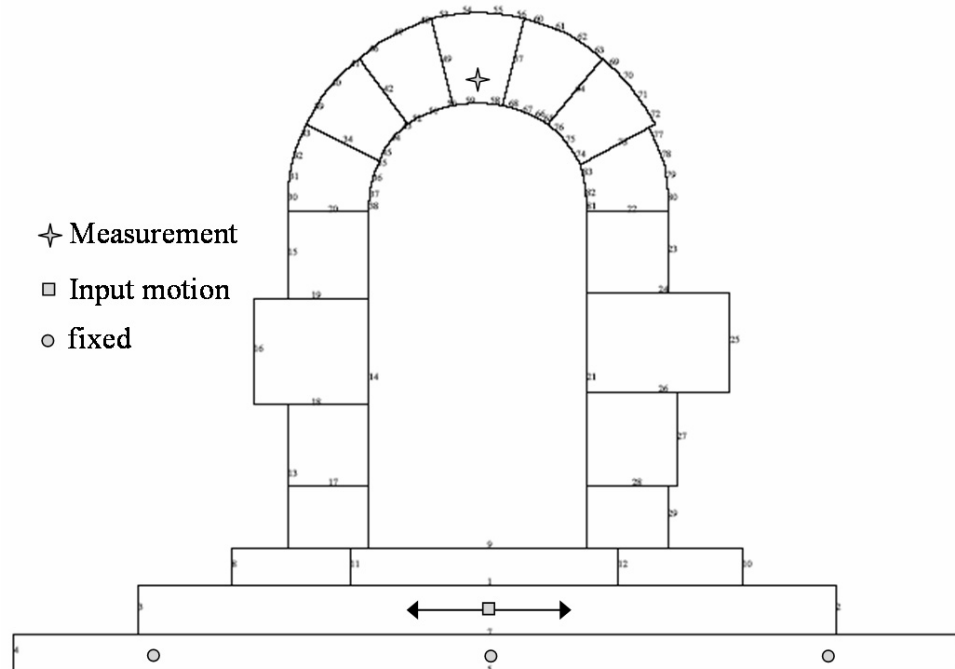


Figure 5.6. The DDA model for the free standing arch. Measurement, loading and fixed points assigned to the mesh are marked.

Figure 5.6 presents the block system for the free standing arch: a basement block is fixated by three fixed points to prevent the block system from falling, a second block is assigned an input point (also called “fixed” by DDA) that receives the induced time-dependant displacement input, and the arch block system above it responds to the motion. The displacements and stresses at the keystone throughout the analysis are recorded by placement of a measurement point at the keystone.

The dynamic response of the free-standing arch was examined under sinusoidal ground-motion functions, in a range of frequencies and amplitudes of 1-2.5Hz and 0.002-0.5m respectively. A number of combinations of frequency and amplitude yielded a failure similar to the one observed in the field. Both combinations of  $f$  and  $A$  of 2.5Hz, 0.005m and 1Hz, 0.013m yielded a downward keystone sliding of ~4.5cm, although in the first combination the adjacent blocks also exhibited a slight downward motion. The numerical analysis implies therefore that the ground motion which triggered keystone sliding in this semi-circular arch had an amplitude and frequency of 0.013m and 1Hz respectively. This combination is equivalent to an acceleration of 0.05g, which is the threshold acceleration found in the analytical analysis.

During the simulation, the expected mechanism of hinge opening which allows the keystone to slide down while the rest of the stones remain in place is confirmed. Furthermore, the pattern of the opening hinges changes dynamically during the simulation and includes hinges at the abutments that open inwards and hinges at the extrados that open outwards (Figure 5.7), similar to the “upper collapse mechanism” discussed in section 2.1.4.

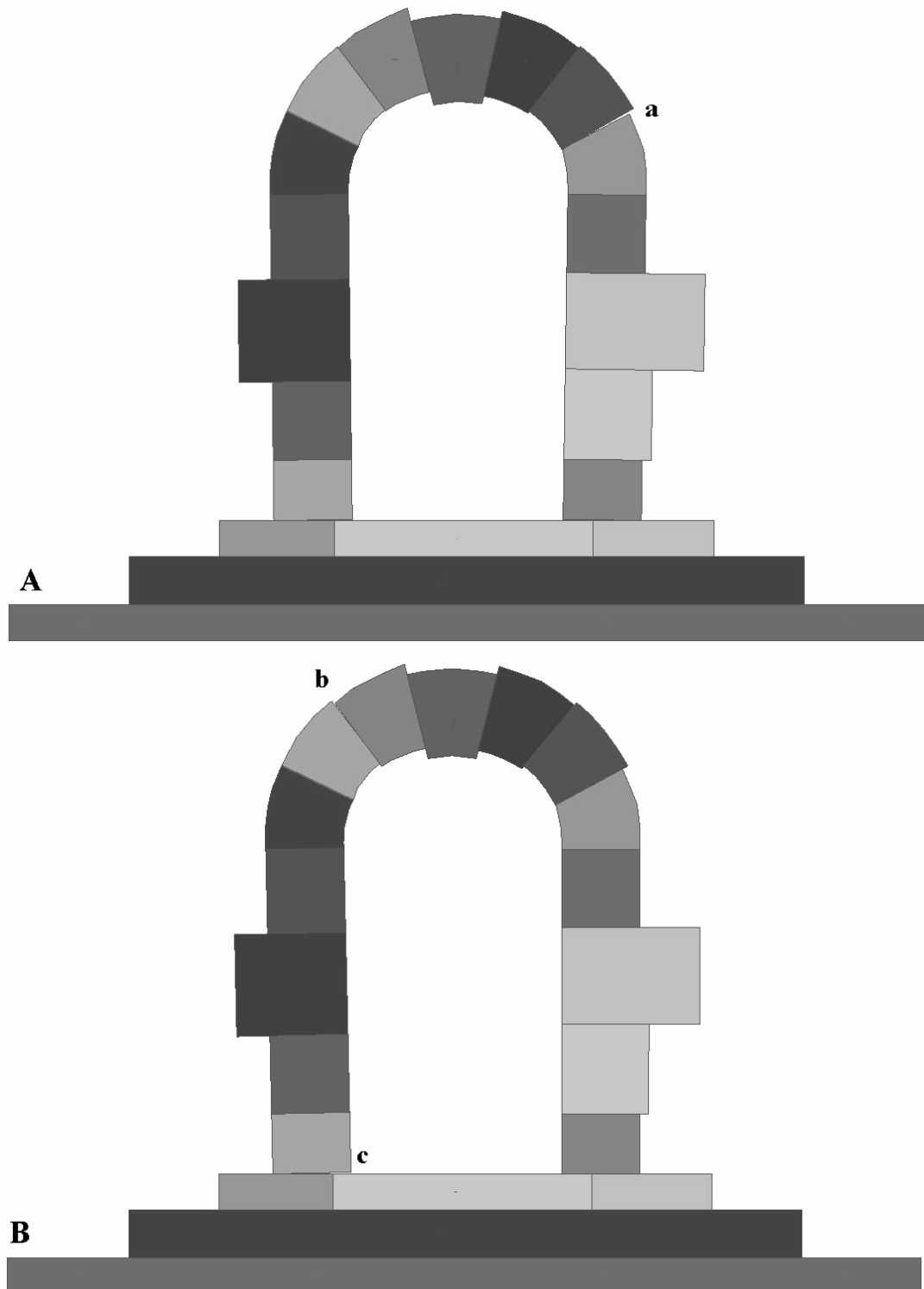


Figure 5.7. Simulation results for the free standing arch. **A.**  $f=1\text{Hz}$ ,  $D=0.013\text{m}$  (equivalent to  $0.05\text{g}$ ). Keystone slides down  $4.7\text{cm}$  after  $4.5\text{sec}$ , adjacent stones remain in place. **B.**  $f=2.5\text{Hz}$ ,  $D=0.005\text{m}$  (equivalent to  $0.126\text{g}$ ). Keystone slides down  $4.5\text{cm}$  after  $2.5\text{sec}$ . adjacent stones undergo downward sliding of up to  $1\text{cm}$ . Points a, b, and c are an open hinge- outwards as in a and b, or inwards as in c.

### Embedded arch

Modeling the embedded arch was a challenging task because of the heterogeneity in block material shape and size shown in Figure 5.3.A. Because of material heterogeneity DDA material lines were assigned to the arch blocks in order to assign different mechanical parameters to the arch and the wall (Figure 5.10). Different mesh configurations and material properties were tested in order to find the conditions in which forward modeling results would fit as closely as possible the observed failure pattern in the field:

1. Generating the block system using the synthetic joint trace generation algorithm of Shi and Goodman (1989) which is the basis for the statistical joint trace generation code DL. The arch was then inserted manually within the heterogeneous wedges that were formed (Figure 5.8.A and C). The result was opening of the wall along semi-vertical joints, separation of the wall from the arch stones, and loss of framework coherency (Figure 5.8.B and D).
2. Simulating the wall material by a continuous, low stiffness block (Figure 5.9.A and B).
3. A hybrid model of statistically generated large-sized blocks (Figure 5.9.C and D).

The last two block configurations resulted with deformations in the surrounding wall and arch abutments, instead of in the arch itself.

4. The final approach, which provided the most satisfactory results, was a simple, consistent masonry wall, in which the structural heterogeneity was represented by lower density and stiffness than those of the hewn stones forming the arch (Figure 5.10).

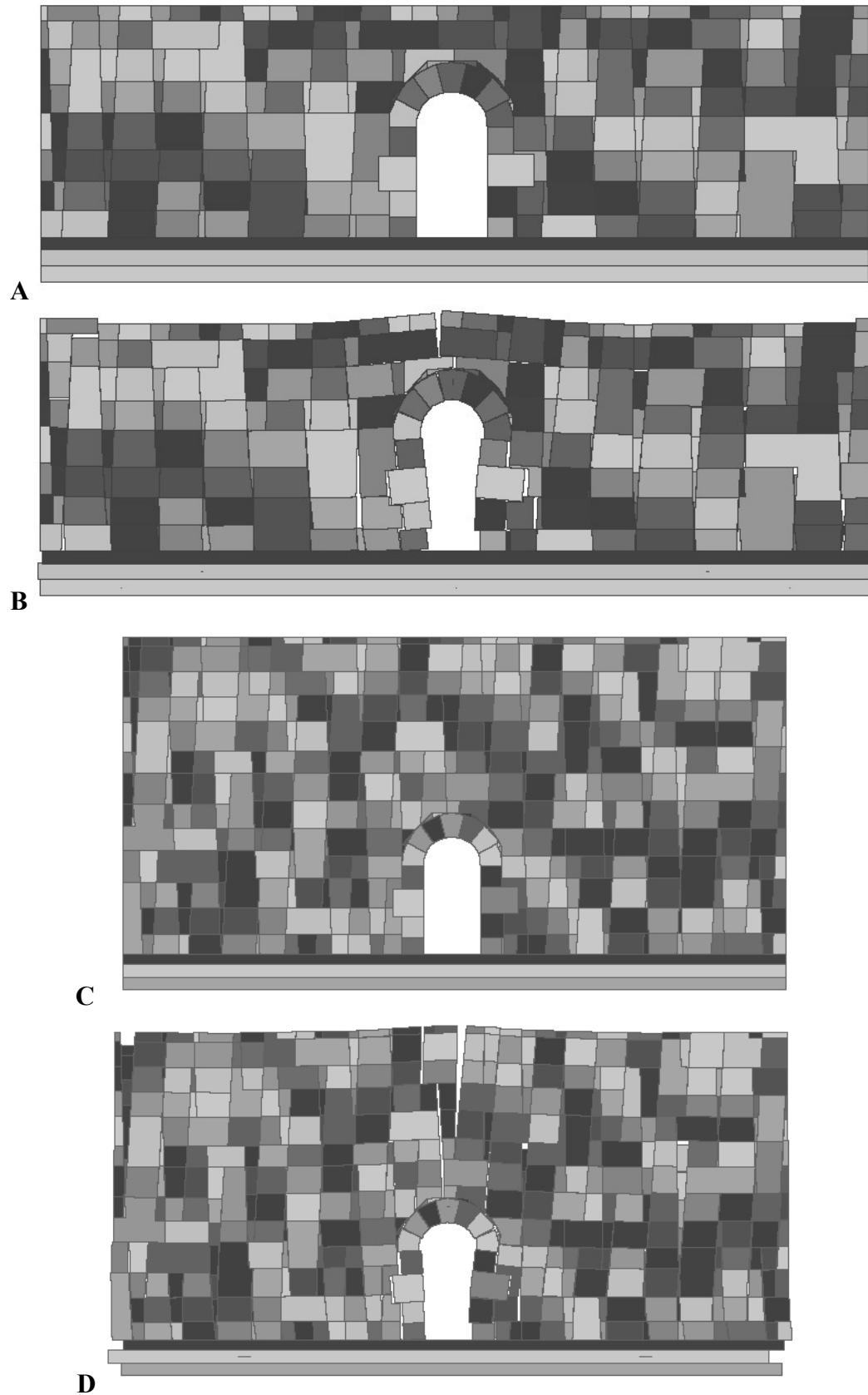


Figure 5.8. The first mesh configuration for the heterogeneous wall of the embedded arch; a combination of a statistical net with manually-inserted lines. **A.** A 10 meters wide, 3 meters high block system. **B.** After 10 seconds, vertical joints open. **C.** A 10 meters wide, 5 meters high block system. **D.** After 10 seconds, vertical joints open, and the arch is distorted.

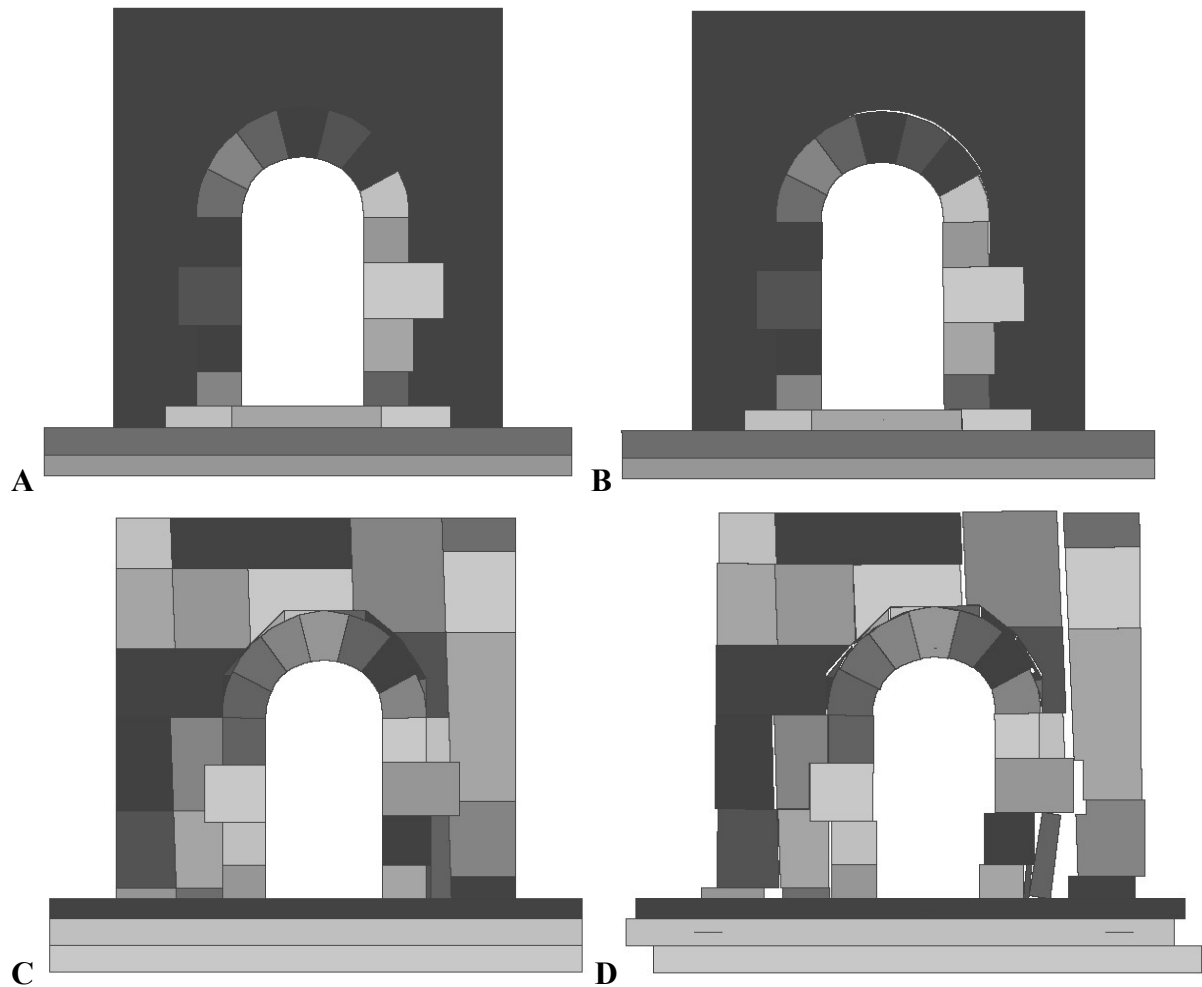


Figure 5.9. **A.** Simulation of the surrounding heterogeneous wall as one soft block,  $E=1\text{MPa}$ . **B.** After 2 seconds, the surrounding block extends and the arch remains intact. **C.** A statistical net with bigger and softer blocks. **D.** After 2 seconds, the wall disassembles.

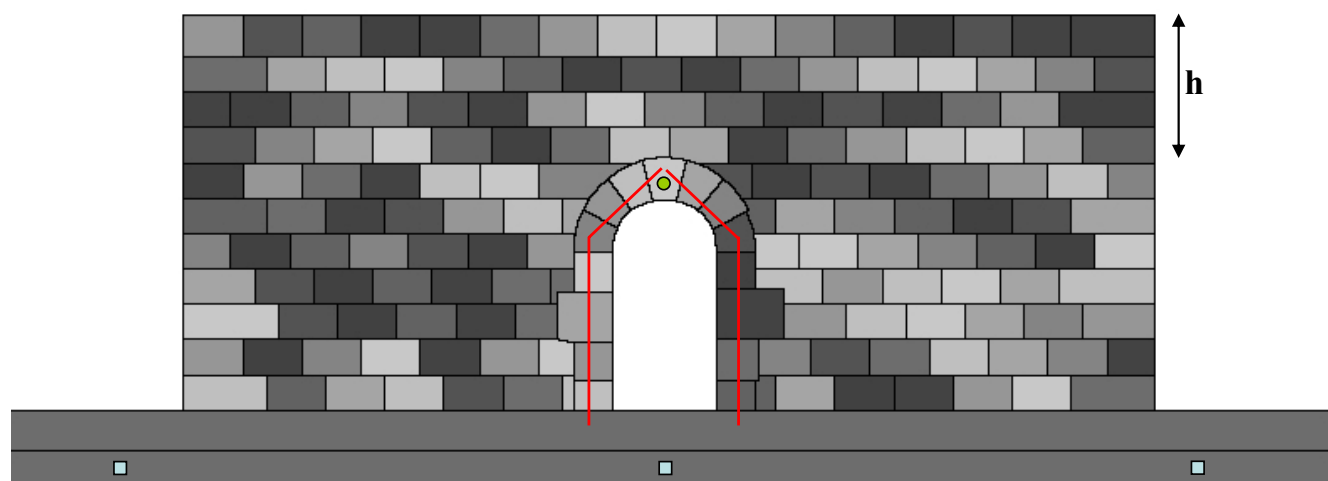


Figure 5.10. The final mesh configuration for the embedded arch. The uniform masonry wall rests on two blocks: the lower is fixed by assignment of three fixed points (squares), and the overlying block can be subjected to time-dependant displacements. The height of the wall above the arch is  $h$ . the lines intersecting the arch blocks represent material lines, and a measurement point (circle) is assigned at the keystone.

Two different loading mechanisms were examined: In the first one, later referred to as ‘dis. mode’, the foundation block was subjected to time-dependant displacements, based on the validation presented in section 4.2. In the second, all block centroids were subjected to time-dependant acceleration. This loading mechanism has been studied before in DDA and is later referred to as ‘qk. mode’.

Repeated runs of the problem revealed that the dis. mode, although validated successfully in a two-block problem, does not provide satisfactory results for a multiple block system, where over 100 blocks respond to the induced motion of a single block at the foundation.

Figures 5.11 and 5.12 display the difference in the mesh response to dis. mode vs. qk. mode. In displacement mode the keystone was displaced upwards, and the entire block system deformed, whereas in quake mode the keystone moved downwards and the rest of the mesh remained intact.

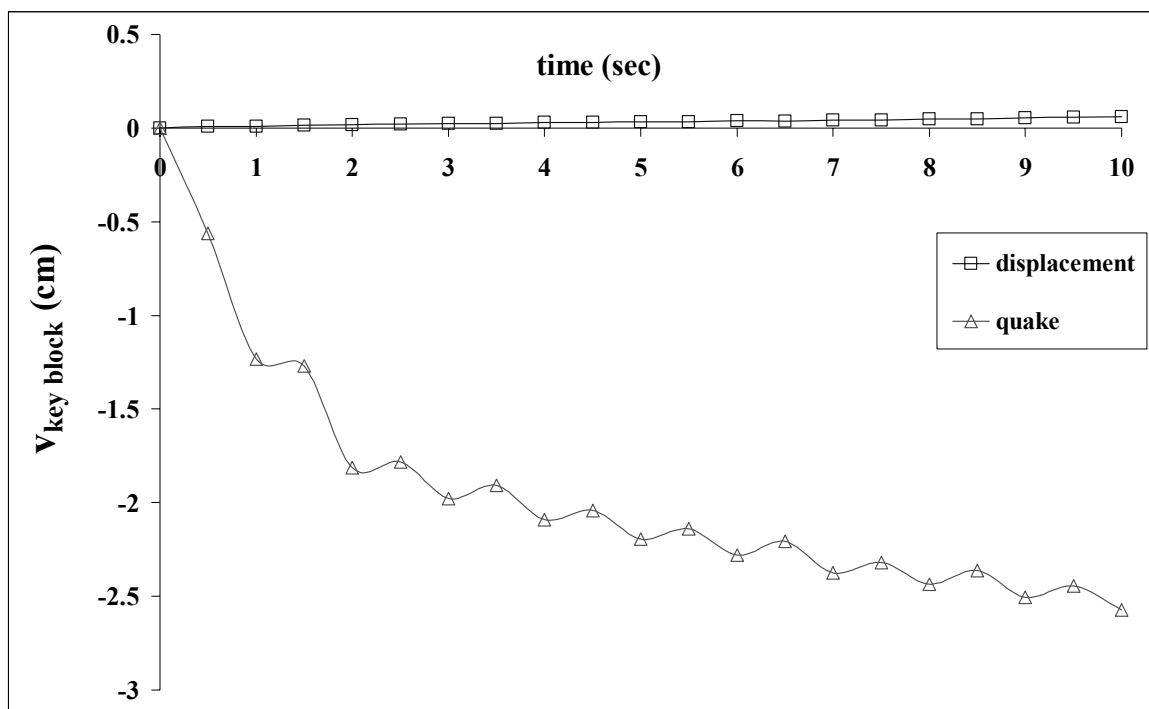


Figure 5.11. Keystone vertical displacement vs. time - influence of loading mechanism.  $A=0.32g$  ( $D=8\text{cm}$ ),  $f=1\text{Hz}$ .

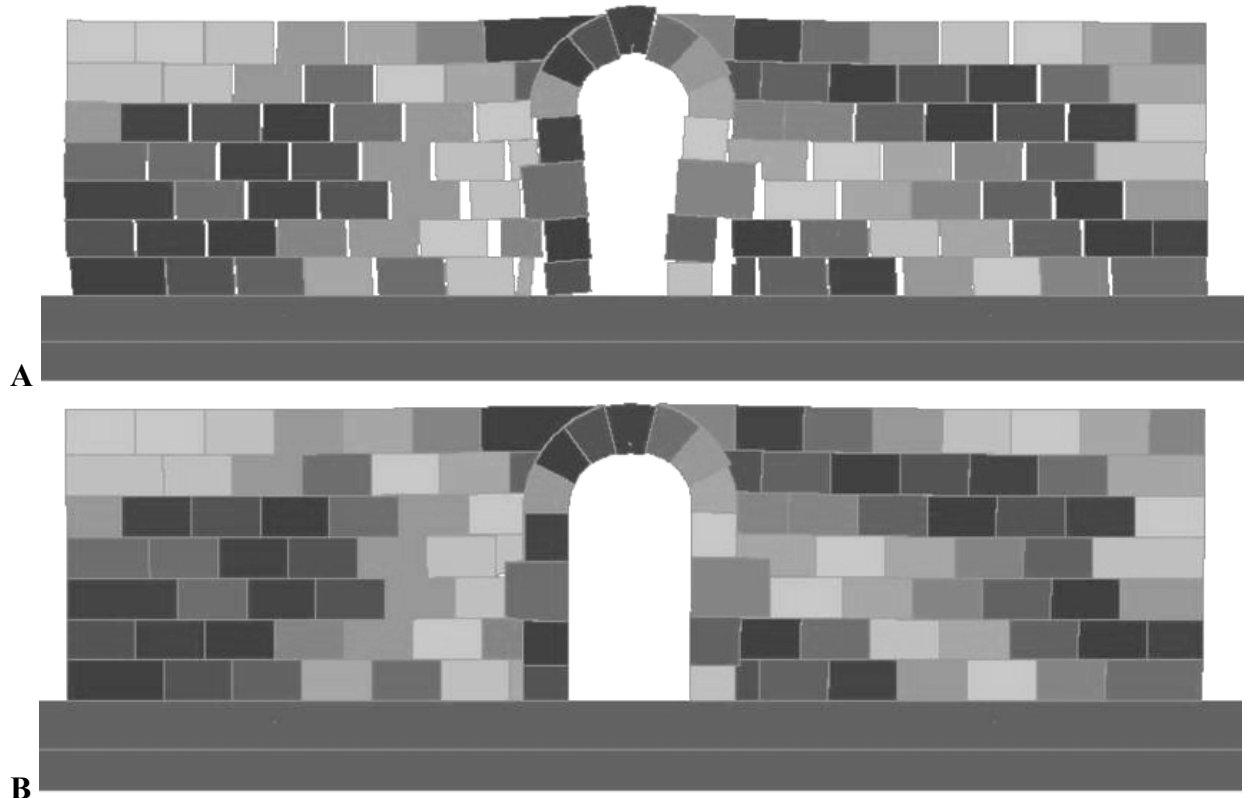


Figure 5.12. Response of the Mamshit block system to an earthquake with  $A=0.32g$  ( $D=8\text{cm}$ ),  $f=1\text{Hz}$ . **A.** displacement mode **B.** quake mode.

In most simulations, the input function (either acceleration or displacement) was of a sinusoidal shape. A real earthquake record was used for comparison, in which the Nuweiba 1995 record, recorded in Eilat and de-convoluted to rock response, was amplified to reach different amplitudes. An example of both records is presented in Figure 5.13 and Figure 5.14.

A sensitivity analysis for the block system presented in Figure 5.10 was performed, with over 50 DDA runs (the full list is displayed in Appendix 3). Overburden, wall stiffness, numerical damping ( $k_{01}$ ), and motion parameters (Amplitude and frequency) were examined. Results are presented in Figure 5.15 to Figure 5.19, where the downward vertical displacement of the key-stone is plotted vs. time. The mechanical parameters of the block system are:  $\phi_{\text{arch}}=35$ ,  $\phi_{\text{wall}}=40$ ,  $E_{\text{arch}}=17\text{GPa}$ ,  $E_{\text{wall}}=1\text{MPa}$ ,  $h=0$ , unless mentioned otherwise, and the analysis is performed in qk. mode. The difference between  $E_{\text{arch}}$  and  $E_{\text{wall}}$  is discussed in relation to Figure 5.16.

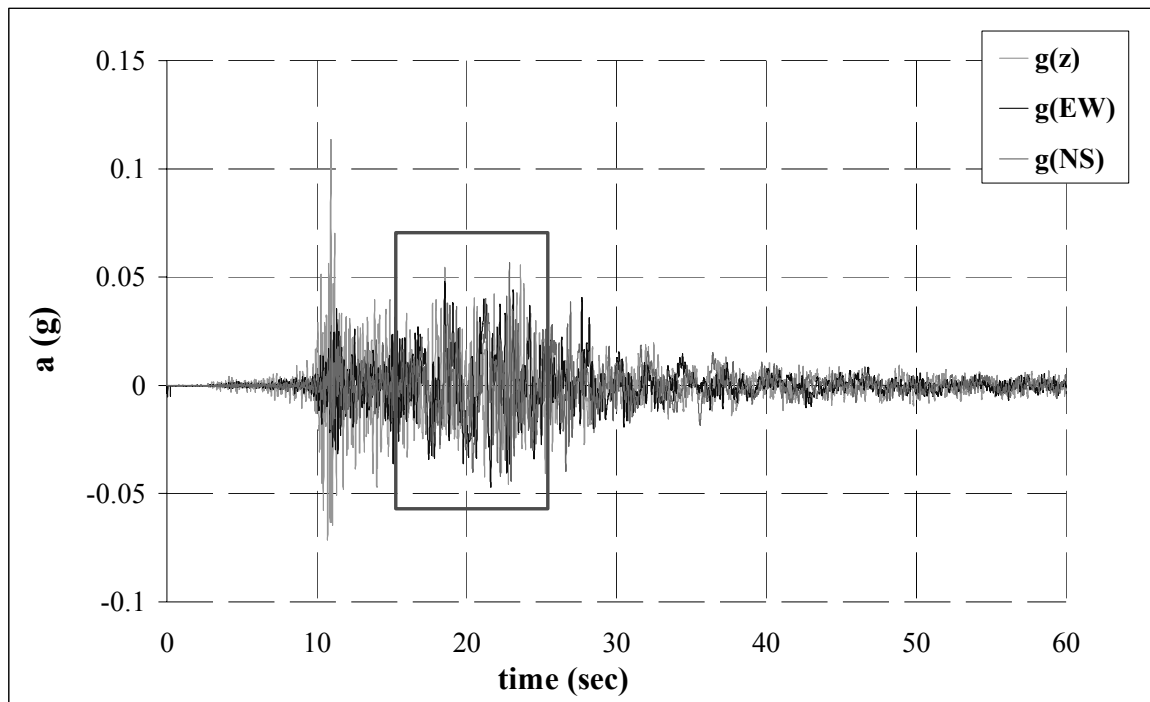


Figure 5.13. The Nuweiba 1995 record, after de-convolution to rock response. The red rectangle marks the 10 seconds that were used for the analysis of the Mamshit block system, 15-25 sec.

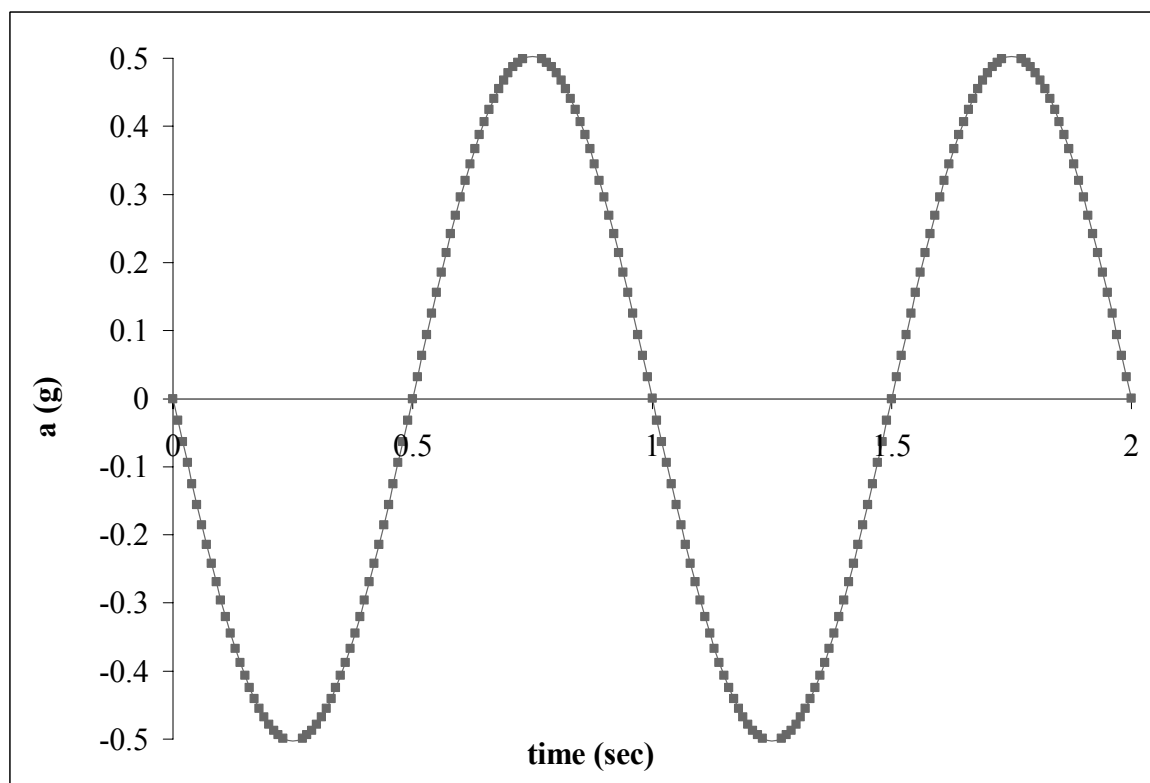


Figure 5.14. A synthetic sinusoidal acceleration record, used for analysis on the Mamshit block system.  $A=0.5g$ ,  $f=1\text{Hz}$ .

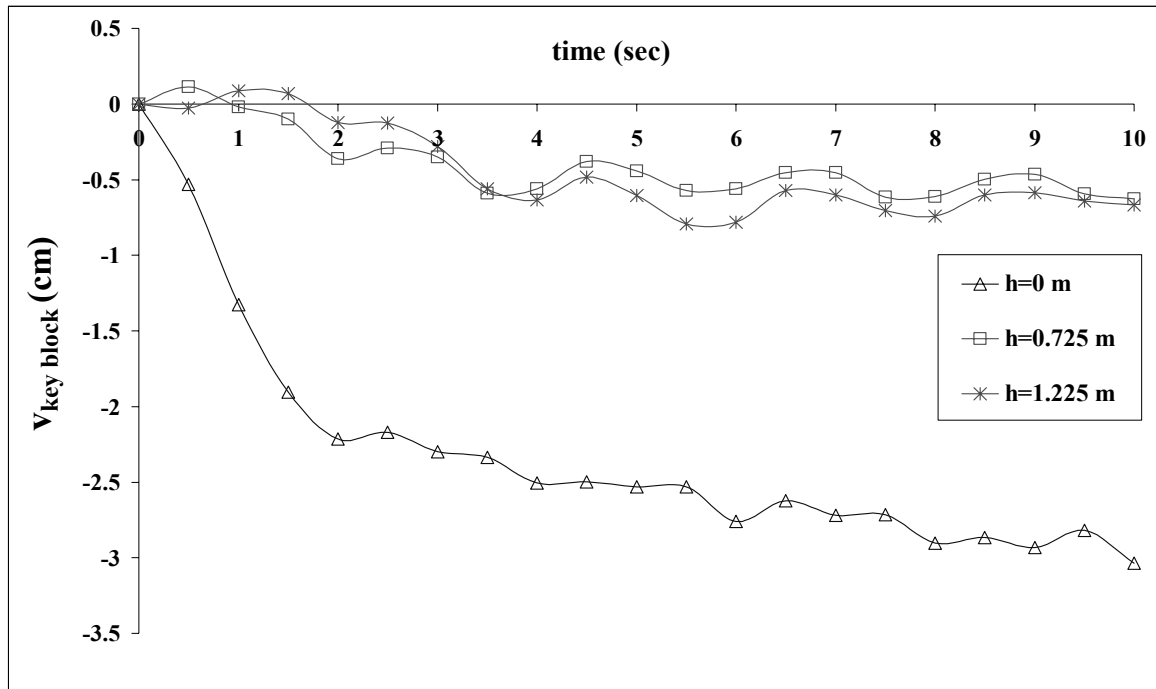


Figure 5.15. Keystone vertical displacement vs. time - influence of overburden ( $h$ ).  $A=0.5g$ ,  $f=1.5\text{Hz}$ .

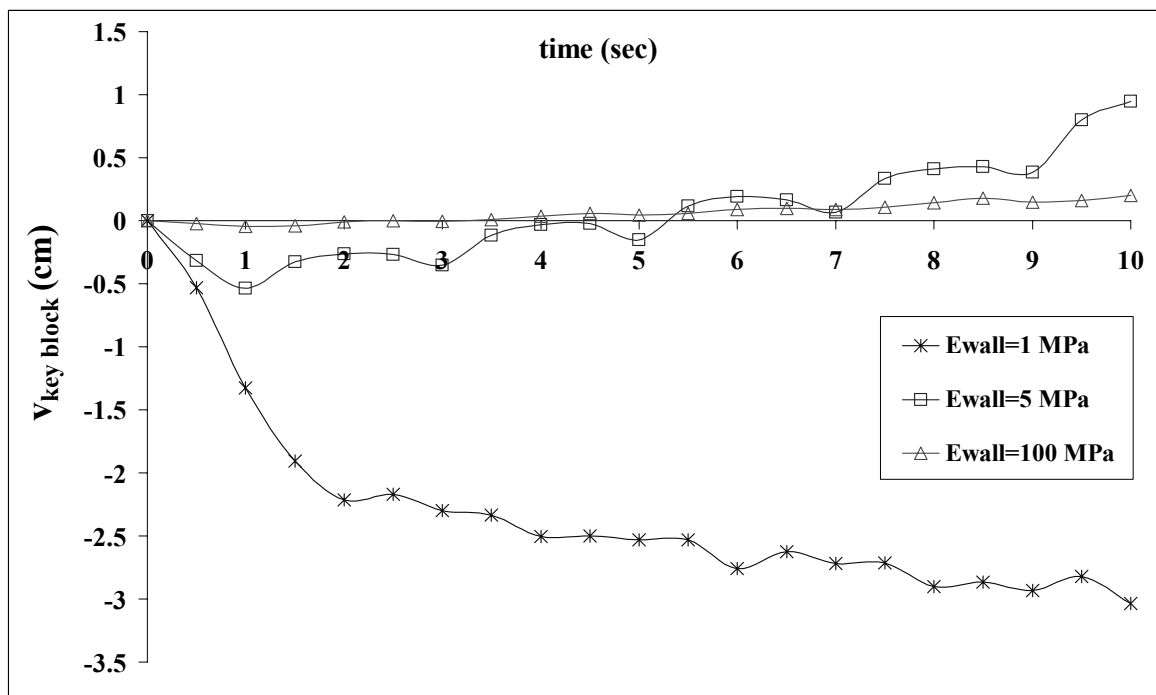


Figure 5.16. Keystone vertical displacement vs. time - influence of wall stiffness.  $E_{arch}=17\text{GPa}$ ,  $A=0.5g$ ,  $f=1.5\text{Hz}$ .

Figure 5.15 shows that when there is overburden above the arch, both in the case of one row of blocks ( $h=0.725\text{m}$ ) and in the case of two ( $h=1.225$ ), the keystone is displaced downwards less than 1cm in the first 4 seconds and is later ‘locked’. However, when there is no overburden

above the arch, the keystone is displaced downwards more than 3cm, almost 2.5 of them in the first 2 seconds. The displacement keeps accumulating without oscillations that can be seen when there is overburden, and the final displacement amount is similar to what is seen at the site. Therefore, it is clear that the observed downward displacement of the arch-keystone became possible only after the collapse of all overlying layers, most probably due to relaxation of arching stresses.

Figure 5.16 implies that a difference of four orders of magnitude between the arch and wall materials is required to obtain the desired deformation and for the deformation to be restricted to the arch only. This large difference might seem exaggerated, but a close inspection of Figure 5.3.A reveals the large heterogeneity and diversity of the wall, where spaces between the wall-blocks are filled with soft filling materials. These materials allow for large deformations under low stresses, and drastically reduce the stiffness of the wall. Therefore a 1 MPa wall stiffness may be reasonable.

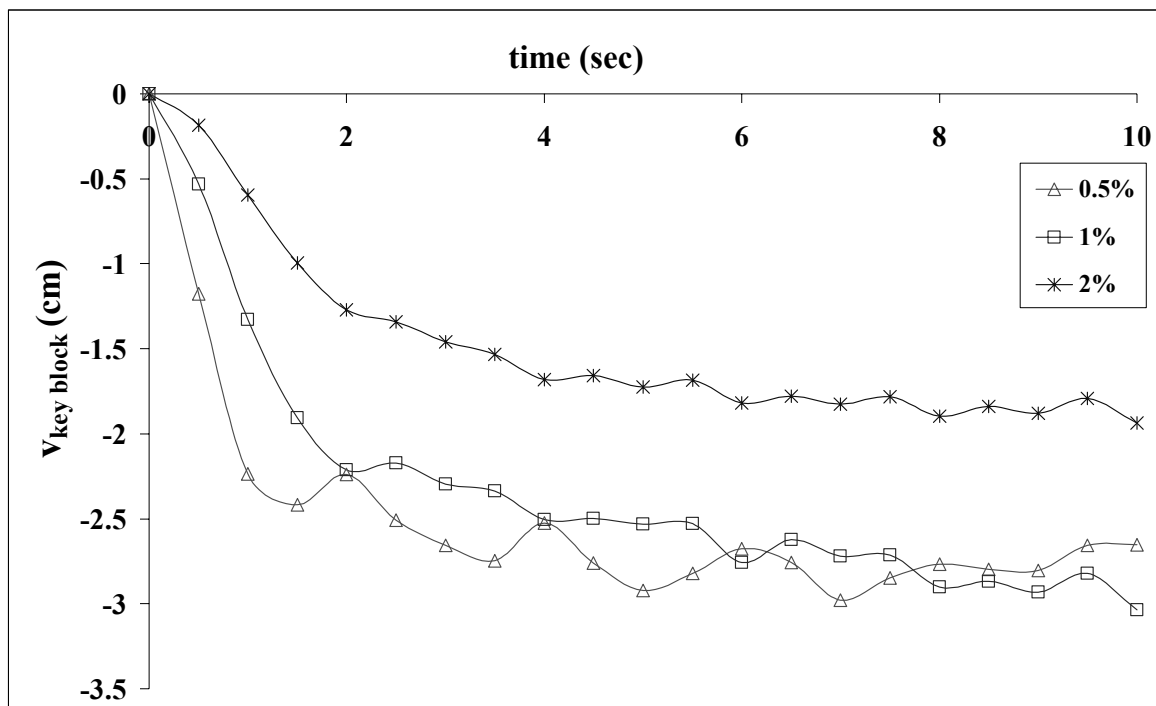


Figure 5.17. Keystone vertical displacement vs. time - influence of numerical damping ( $k_{01}$ ).  $A=0.5g$ ,  $f=1.5\text{Hz}$ . Zero damping is not presented, since it resulted in complete destruction of the block system.

The application of numerical damping was discussed in the beginning of Ch.4. It was found that in the case of a large block-system, consisting of many blocks, some energy dissipation is required for obtaining realistic results. On the basis of field and experimental studies Hatzor et al. (2004) and Tsesarsky et al. (2005) found that 2% velocity damping should be sufficient. Figure 5.17 suggests that for the Mamshit case, the ideal amount of damping is 1%, since 2% damping reduces the displacement unnecessarily, while the 0.5% damping produces stronger keystone fluctuations. When no damping is applied ( $k_{01}=1$ ), the analysis results in complete destruction of the structure.

Figure 5.18 displays the influence of the acceleration amplitude on keystone displacement. It can be seen that while a relatively low amplitude ( $A=0.1g$ ) results in a small displacement, a high amplitude ( $A=1g$ ) results in strong fluctuations and in a shift in the accumulated displacement direction after  $\sim 4$  sec. The best fit amplitude for this block system seems to be around  $0.5g$ .

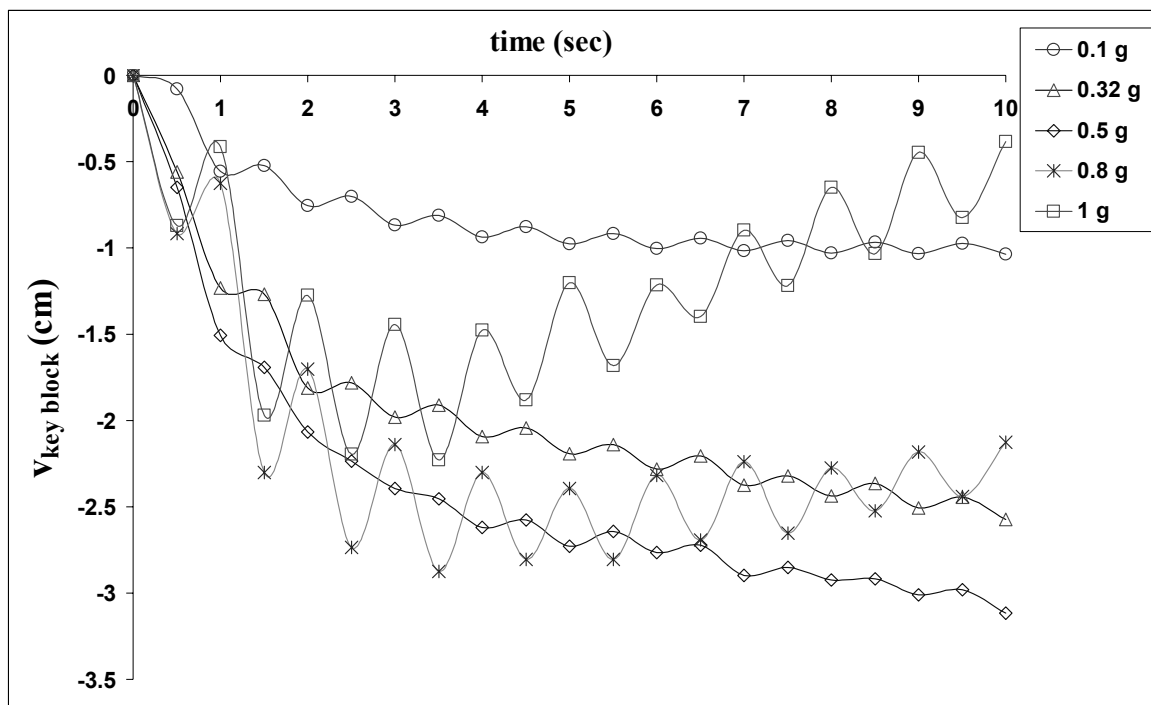


Figure 5.18. Keystone vertical displacement vs. time - influence of amplitude.  $f=1\text{Hz}$ .

A very interesting behavior is displayed in Figure 5.19 which shows the influence of frequency on keystone displacement: the ideal frequency seems to be around 1Hz, because a low frequency (eg. 0.5Hz) results in strong fluctuations and a high frequency (eg. 5Hz and 10Hz) result in “locking” of the structure, and very little displacement.

The structure response to the real Earthquake record of Nuweiba 1995, amplified by 15 (PGA~0.6g), is also displayed in Figure 5.19. It can be seen that the behavior of the block system is not significantly different when a range of frequencies and additional vertical accelerations are introduced, meaning, that the results of the synthetic records of horizontal motion only are valid enough to be discussed and analyzed.

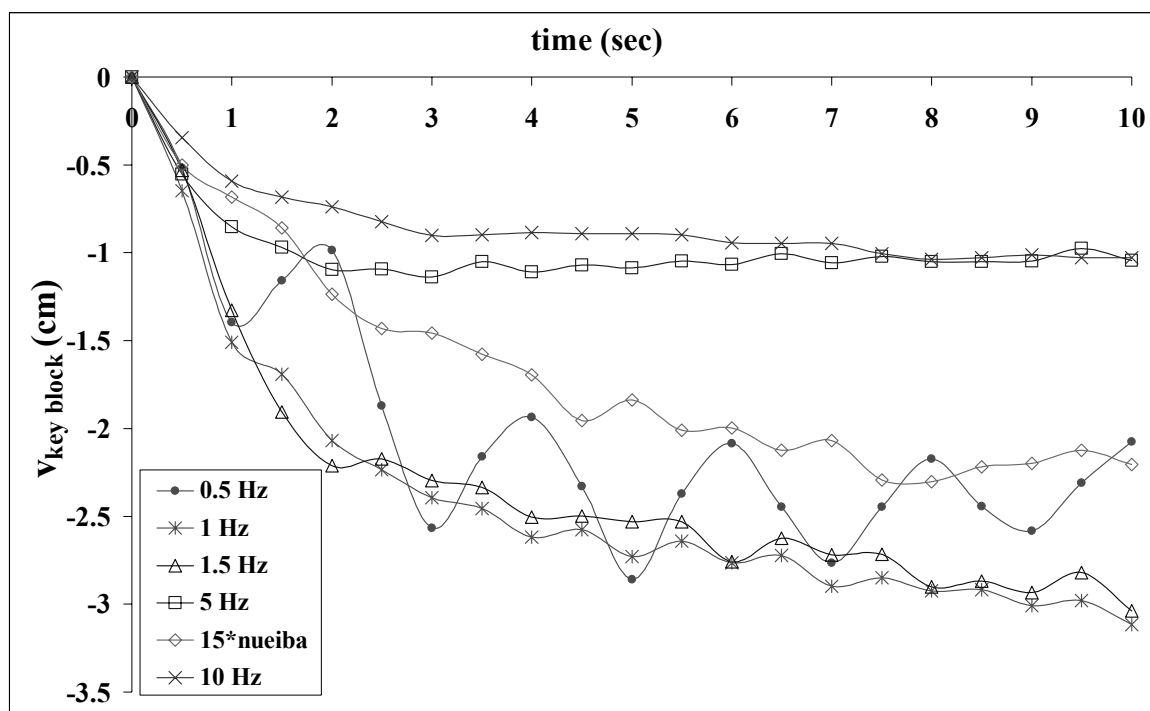


Figure 5.19. Keystone vertical displacement vs. time - influence of frequency.  $A=0.5g$ .

#### 5.1.4 Summary

- Although the analytical analysis is very simple, fast, and straight-forward, the results are not representative, since they are restricted to a free-standing, semi circular arch only. Furthermore, the obtained results are only valid for pseudo-static loading at the abutments and neglect frequency or duration of motion. Nevertheless, the obtained acceleration value is in remarkable agreement with the numerical analysis of the free-standing arch, which implies that the analysis is correct, even if not satisfying.
- The displacement mode, which was validated in section 4.2 for three blocks, does not provide satisfactory results in a more complex block system. Further work is required to obtain realistic results with this loading mode in large block systems.
- The quake mode was designed for coherent rock-masses, and using it for masonry structures might overlook the differences between the two: is there a structural amplification that is ignored? How do seismic waves propagate through the structure? How different are accelerations in different heights and parts of the structure? Answers to these questions are beyond the scope of this research, though they might affect significantly the implementations of its results.
- The sensitivity analysis brings up some interesting site-specific conclusions:
  1. Downward displacement of the arch-keystone became possible only after the collapse of the overlying layers due to the relaxation of arching stresses.
  2. The observed failure mode was mainly a result of horizontal accelerations, whereas vertical accelerations had little effect on it, if any.
  3. As can be seen in Figure 5.19 and Figure 5.18, most of the accumulating downwards displacement occurs in the first two seconds. Therefore, all simulations lasted 10 seconds, and a longer simulations was not attempted.

4. The critical frequency and amplitude for the detected failure mode in the analyzed arch is 1Hz and 0.5g, respectively. The response of the structure and final position of the keystone after a DDA run with these parameters is shown in Figure 5.20.

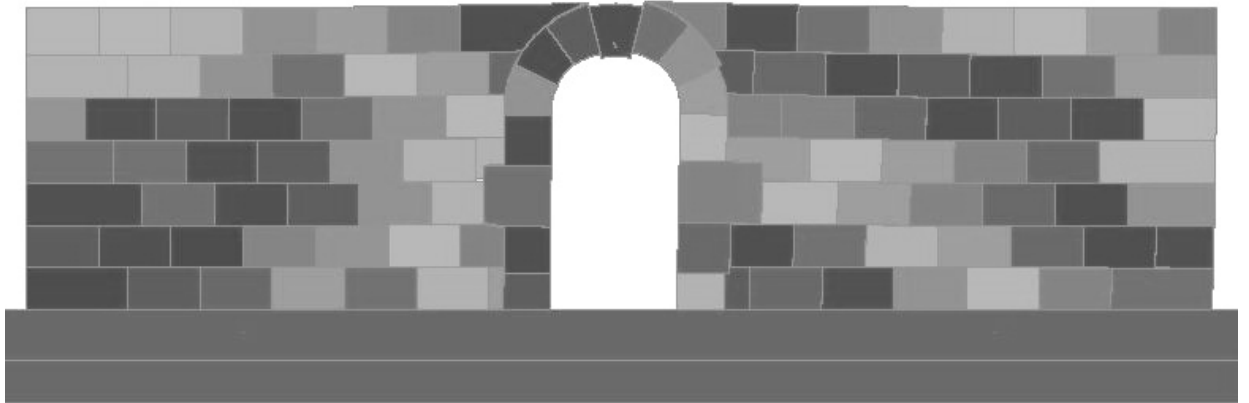


Figure 5.20. The result of the dynamic block system response under an earthquake with  $A=0.5g$  and  $f=1Hz$ . The accumulating downwards displacement of the keystone is 3.11 cm.

## 5.2 A block sliding on a plane - results from Avdat

### 5.2.1 Background

#### Geography and Geology

The ruins of Avdat lie in the central Negev Mountains, at a height of 655m above sea level, and about 80m above the surrounding terrain, on one of the higher levels of the Eocene Avdat Plateau (Figure 1.2).

The Eocenian strata are composed of four interchanging layers of soft chalk and hard limestone. Part of the ancient city is carved as caves into the soft chalk (Horsha formation), while the acropolis (the higher part of the city) is set on hard limestone (Matred formation), from which the building material for Roman and Byzantine structures was taken.

#### Archaeology and History

Avdat (or Oboda) was established as a road station along the Nabatean Spice route in the 3rd century BCE. Evidence for extensive farming and four wine-presses found amongst the ruins of the city, tell of a fruitful transition into farming by the middle of the 1st century AD. At the year 106 AD the Nabatean kingdom, amongst the rest of the Negev, was annexed to Provincia Arabia as part of the Roman Empire, and the Roman quarters were built, along with a couple of watch towers and a fortress. With the advent of Christianity in the Negev, by the middle of the 4th century AD, two churches and a monastery replaced the pagan temples in the acropolis on top of the hill (Negev, 1988b).

The occupation in Avdat came to an end at 636 AD. There is evidence for Muslim occupation that set the town on fire, though the main reason is probably an earthquake between 631-636 (Fabian, 1998) that destroyed 75% of the buildings after which the town was never rebuilt (Negev, 1988b). Mazor and Korjenkov (2001) reported over 180 cases of seismic damage to buildings from all settlement periods, including buildings that were in use in the late Byzantine

period, that is, the 7th century AD. There is evidence of an earlier earthquake as well, in the 4<sup>th</sup> century, attributed to the historically recorded 363 AD quake. Amongst the different failure types observed, the sliding of a block on a plane was noticed in several places. This work will focus on 5 blocks in the western wall of the southern Roman tower (Figure 4.1), which show up to 7cm of westerly sliding; partly rotational.

### The analyzed structure

The Roman tower was built in the year 294 AD. It is a two-story building, claimed by A. Negev (1988b) to have raised to a height of 12m, from which only 6m are left standing today. The tower walls, 1m thick, built of two layers of ashlar, are laid directly on bedrock (Negev, 1997). The collapse of the whole top floor and small shifts of numerous blocks in its walls indicate that this building has withstood several strong earthquakes.

Detailed mapping of the northern wall of the tower is presented in Appendix 2.

The displaced blocks are numbered (Figure 5.22) and their parameters are presented in Table 5.1.

Table 5.1. Geometry and weight of the displaced blocks in the Roman tower at Avdat.

Block number	Width to NS (m)	Width to EW (m)	Height (m)	Volume (m <sup>3</sup> )	Weight** (kN)	Overburden (m)	Weight of overburden (kN)
1	0.78	0.37	0.46	0.133	3.33	3.39	24.52
2	0.38	0.62	0.39	0.091	2.28	3.01	17.77
3	0.57	0.36	0.36	0.074	1.86	2.65	13.63
4	0.65	0.36*	0.39	0.091	2.28	3.01	17.65
5	0.63	0.36*	0.36	0.081	2.03	2.65	15.06

\* Estimation, not enough data

\*\*  $\rho = 2555 \text{ Kg/m}^3$  (taken from laboratory results, see section 4.1.2)

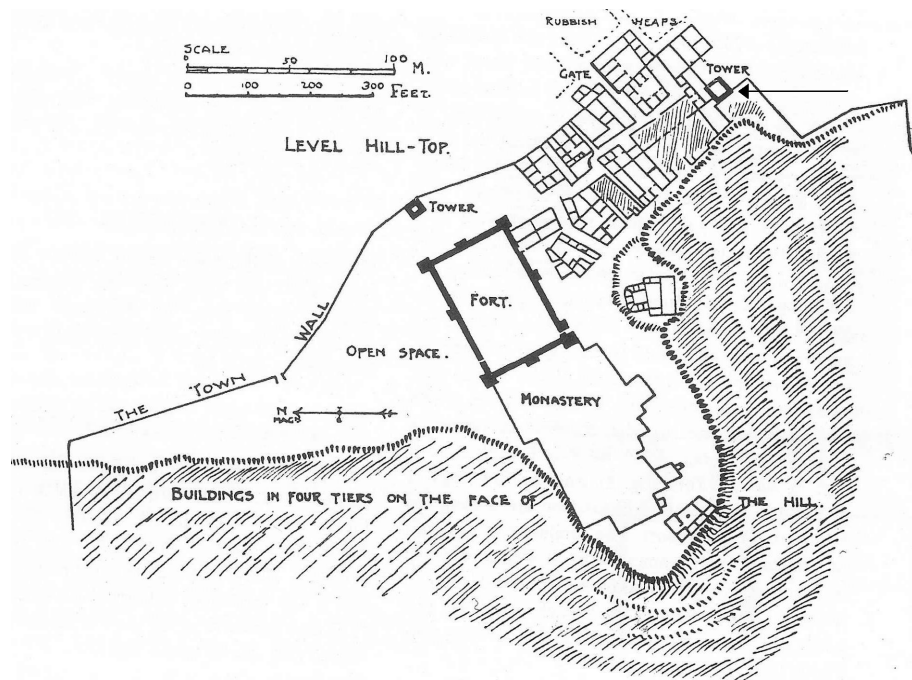


Figure 5.21. A sketch-plan of the city of Avdat, after Woolley and Lawrence, 1914 (Negev, 1997), The black arrow at the top points at the southern Roman tower.



Figure 5.22. The Roman tower in Avdat, a view of the western wall. The displaced blocks are numbered for reference.

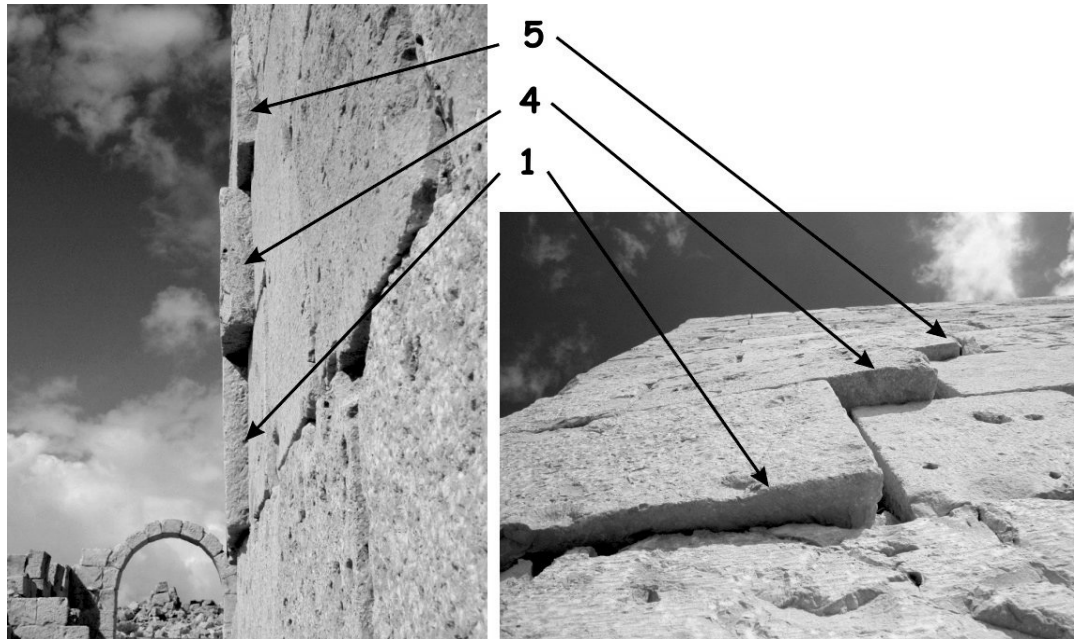


Figure 5.23. The displaced blocks, two additional points of view. Block numbers refer to Figure 5.22.

### 5.2.2 Analytical solution

The equation development is presented in section 2.1.1. The analytical analysis can be done for one block at a time, or for a group of blocks. Although there is relative displacement between the five displaced blocks in the roman tower, mutual motion may be assumed since the five blocks are adjacent and show similar displacement in order of magnitude and direction.

#### Block no.1 only:

$H_{\text{overburden}}=3.39\text{m}$ ,  $h_2=0.46\text{m}$ ,  $\phi=35^\circ$  (chapter 3).

Substituting the values into Eq. 2.7 gives:

$$a_{\text{threshold}} = \frac{(2(h_3 + \dots h_n) + h_2)}{h_2} g \cdot \tan \phi = \frac{(2 \cdot 3.39 + 0.46)}{0.46} g \cdot \tan \phi = 15.74g \cdot \tan \phi = 11.02g \quad (5.1)$$

#### 5 blocks together:

This case is more complicated and thus treated in 3D, using the same concept that was introduced in Section 2.1.1 but different equations. The shape of the composed block is a stepped one that forms six frictional surfaces (marked as  $S_i$ ) which are applied with different loads, depending on

the overburden above them (Figure 5.24). The weight on each of the surfaces is calculated according to the following general equation:

$$W = d * L * h_{\text{overburden}} * \rho * g \quad (5.2)$$

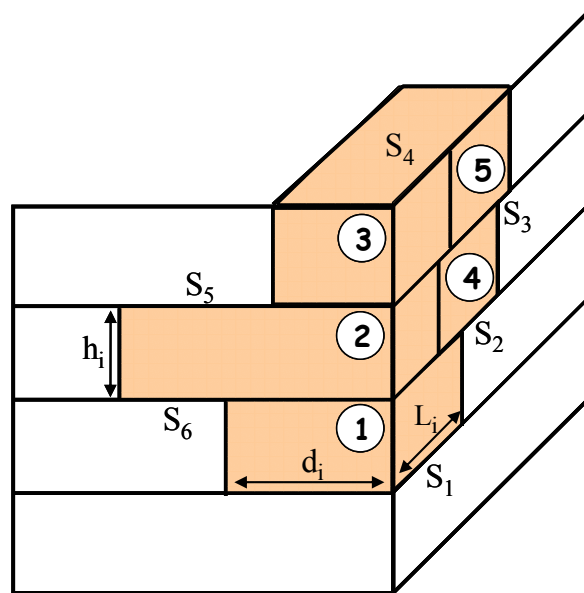


Figure 5.24. A schematic presentation of the 5 block case: six frictional surfaces (marked as  $S_i$ ) are formed by the stepped shape of the composed block. The North-South dimension of the block is marked as  $L_i$  and the East-West dimension is  $d_i$ . The weight on the frictional surfaces is calculated from the column of rock mass above the surface.

The Normal weights (after Eq. 5.2) on the six frictional surfaces and the mass of the composed block (Eq. 2.6) are:

$$W_1 = 27.72 \text{ kN}, W_2 = 7.64 \text{ kN}, W_3 = 4.61 \text{ kN}, W_4 = 28.66 \text{ kN}, W_5 = 7.45 \text{ kN}, W_6 = 8.06 \text{ kN},$$

$$W_{\text{total}} = 84.25 \text{ kN} \quad m_{\text{block}} = 1200 \text{ Kg}.$$

Substituting the values into Eq. 2.7 gives:

$$a_{\text{threshold}} = \frac{\sum W_i}{m_{\text{block}}} \cdot \tan \phi = 70.16 \cdot \tan \phi = 4.13g \quad (5.3)$$

Both values are unrealistically high, though the threshold value for the 5 blocks together can be significantly reduced by introducing vertical accelerations. For example, in the case of  $a_v = 0.75g$ , the horizontal threshold acceleration will be  $a_h = 1.03g$ . Still, the initiation of block displacement requires very high values and a concordant phase of vertical and horizontal accelerations.

### 5.2.3 Numerical solution

The numerical analysis of the roman tower at Avdat was performed on a block system representing the tower's northern wall, to best capture the observed westerly sliding of the three corner stones.

The block system, displayed in Figure 5.26, was generated using program DC of DDA. The DC mesh includes the entrance door and a confining block on the left side, which represents the later added structure that restricts lateral movements to the left (Figure 5.25). The confining block was fixed by five fixed points, and the displacement of five corner blocks was measured: three of the analyzed blocks (1, 2, and 3 from Figure 5.22 are marked as *b*, *c* and *d* in Figure 5.26), one above (e) and one below (a) them (Figure 5.26). The structure consists of one set of mechanical parameters, presented in Table 3.1.



Figure 5.25. The northern wall of the roman tower at Avdat. The five corner blocks are marked and their displacement direction is displayed with an arrow.

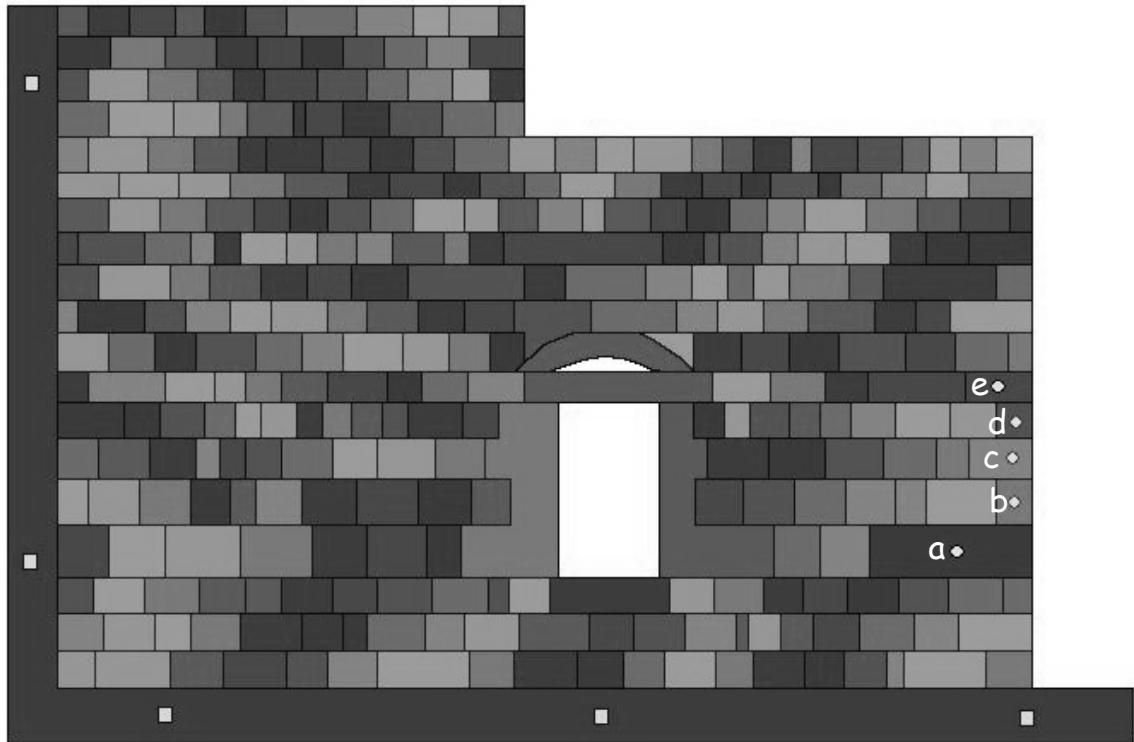


Figure 5.26. The DDA block system for the tower at Avdat. Five fixed points (squares) are assigned to the confining block, and five measurement points (circles) are assigned corner blocks. Points *b*, *c* and *d* are blocks 1,2 and 3 respectively.

The location of the displaced blocks at mid height of the wall and not at the top, where normal stresses on the frictional surfaces are at minimum, is not intuitively understood and is in contradiction with the basic physical principals of the pseudo-static analysis. Therefore, a simulation without the confining wall was performed in order to analyze the basic behavior of the structure. The analysis predicts the exact observation that is noticed in the field, though with greater expansion, in which all blocks in the doorway level, on both sides, are displaced outwards (Figure 5.27). This result might indicate arching caused by the doorway on both sides, which reduces normal stresses, and allows for block displacement in the relaxed “abutments”, in mid-height of the structure. This interesting result, again, demonstrates the extensive treatment of a dynamic solution to such a multi-block problem, versus the restricted and limited analytical approach.

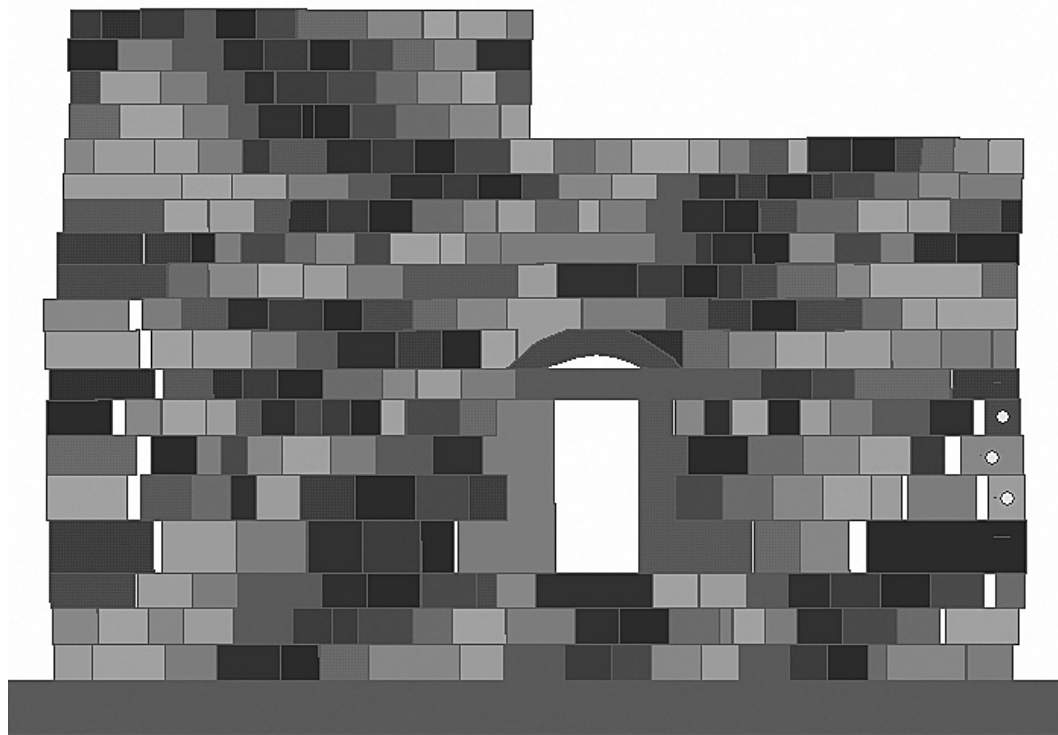


Figure 5.27. A simulation without a confining wall predicts the exact height of displaced blocks as is observed in the field. The graphical output implies that preferred displacement will occur at the doorway level.  $A=1.5g$ ,  $f=5\text{Hz}$ .

A sensitivity analysis for amplitude, frequency and additional vertical accelerations was performed, and results are presented in Figure 5.28 through Figure 5.32, where the average horizontal displacement ( $D_h$ ) of the five measurement points is plotted vs. time. All simulations were performed with 1% damping and are induced by a synthetic sinusoidal acceleration record (Figure 5.14). The full list of DDA runs is displayed in Appendix 3.2.

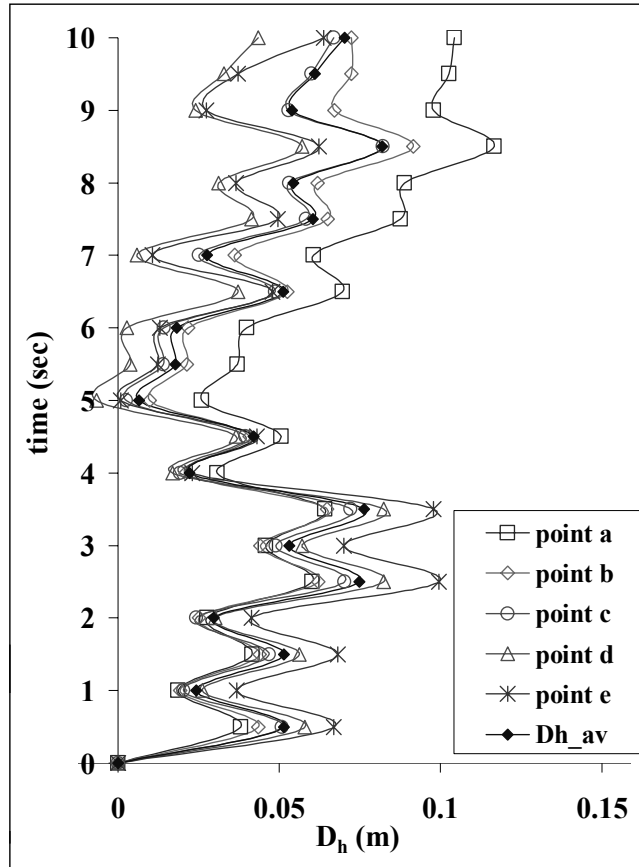


Figure 5.28. Horizontal displacement of all 5 measurement points, point *a* being the lower one and point *d* the upper one, points *b*, *c* and *d* correlate to blocks 1, 2 and 3 from Figure 5.22.  $D_{h\_av}$  is the average horizontal displacement of the five measurement points.  $A=1g, f=3Hz$ .

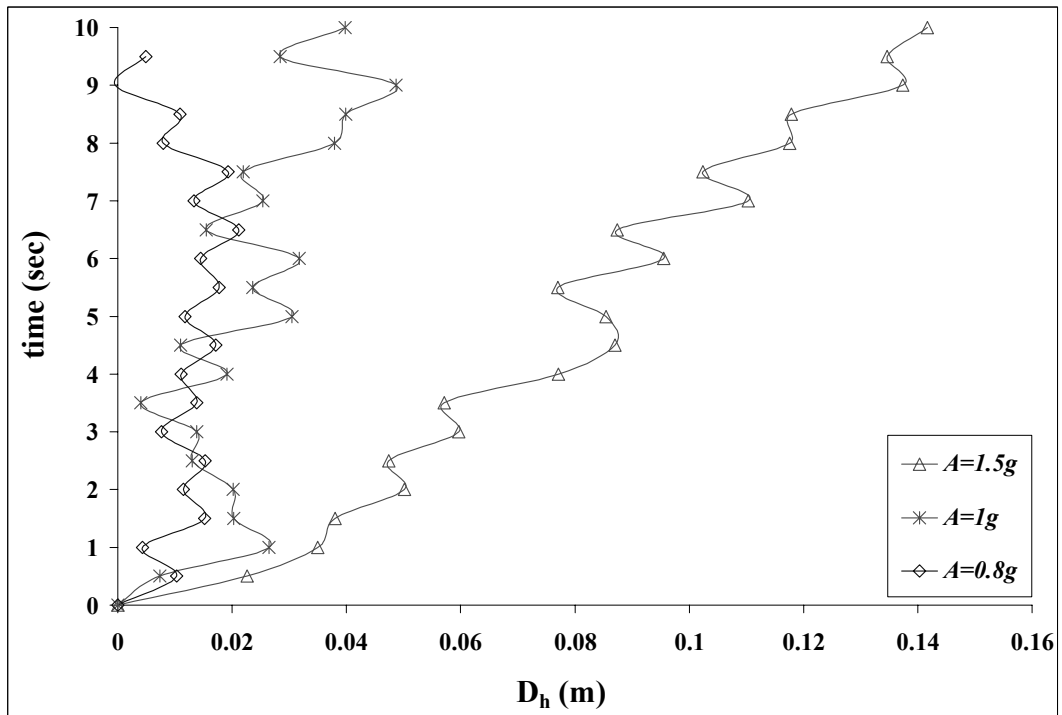


Figure 5.29. Average horizontal displacement ( $D_h$ ) of the five measurement points vs. time - influence of amplitude.  $f=2Hz$ .

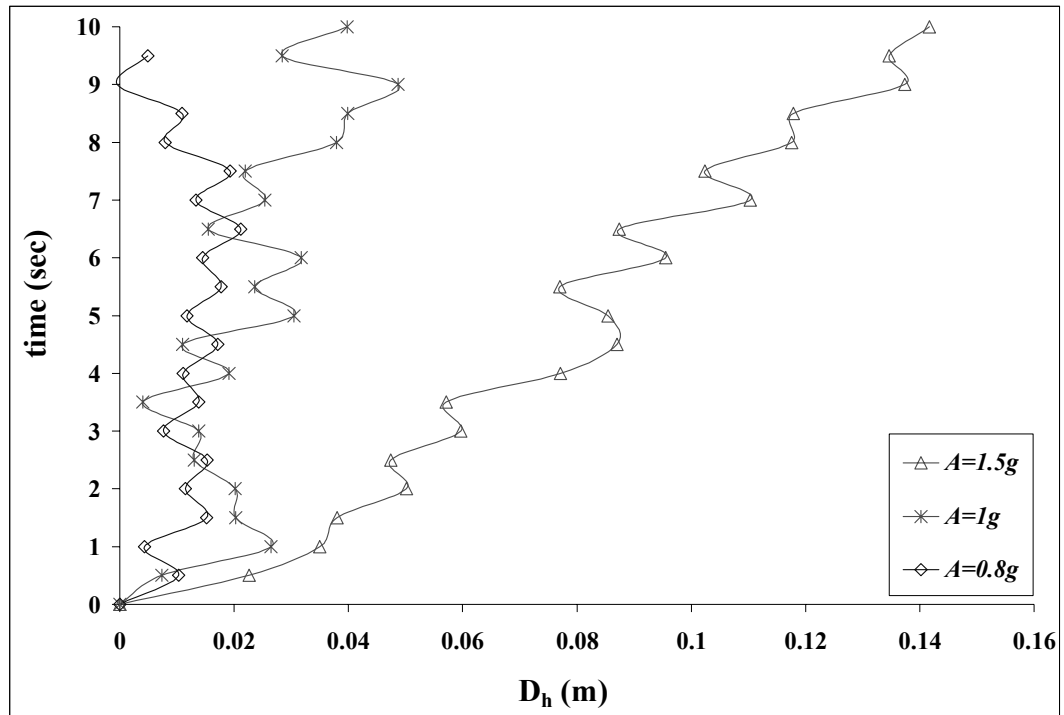


Figure 5.30. Average horizontal displacement ( $D_h$ ) of the five measurement points vs. time - influence of amplitude.  $f=5\text{Hz}$ .

Figure 5.29 and Figure 5.30 display the influence of the amplitude on the structure response, under two different frequencies. Figure 5.29 shows a logical behavior, in which larger amplitude causes larger displacement. In Figure 5.30, though, the two curves of  $A=0.8g$  and  $A=1g$  are erratic and intersect, and do not follow any anticipated behavior.

Following the pseudo-static analysis, the results of which suggested that very high horizontal accelerations will be needed to initiate movement, additional vertical accelerations were introduced to the analysis in phase with horizontal. The response of the structure to three levels of vertical accelerations is presented in Figure 5.31, showing that displacements increase with increasing vertical acceleration, as expected due to vertical load relaxation on frictional surfaces.

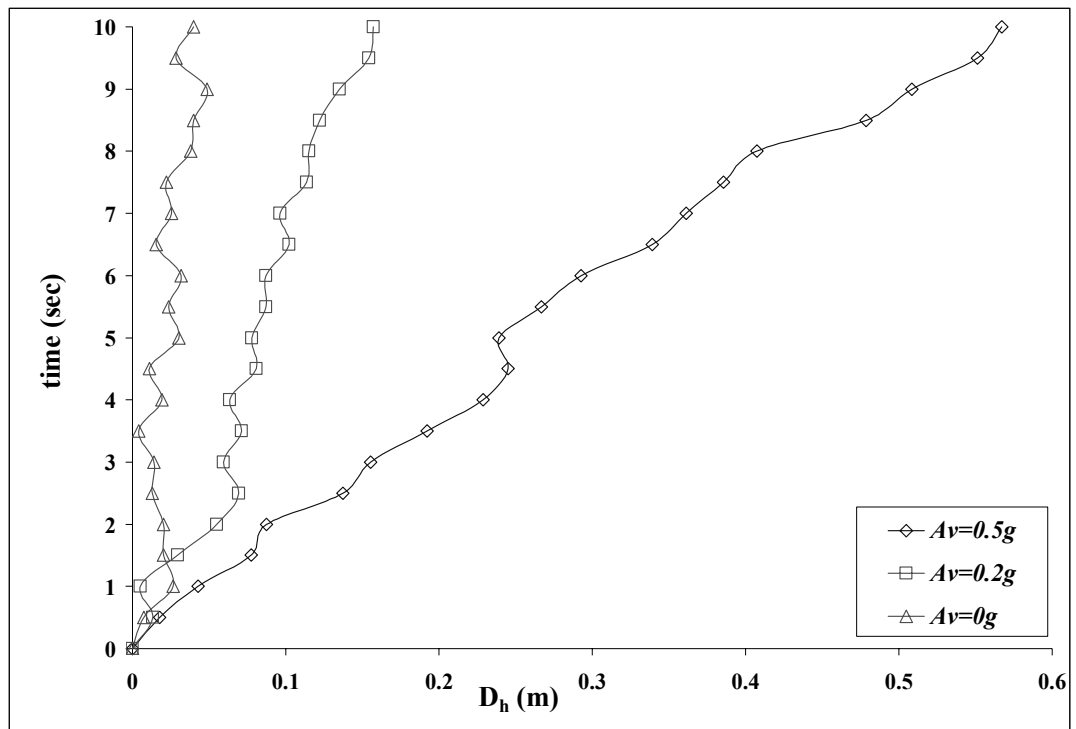


Figure 5.31. Average horizontal displacement ( $D_h$ ) of the five measurement points vs. time - influence of additional vertical acceleration.  $A_h=1g$ ,  $f=5\text{Hz}$ .

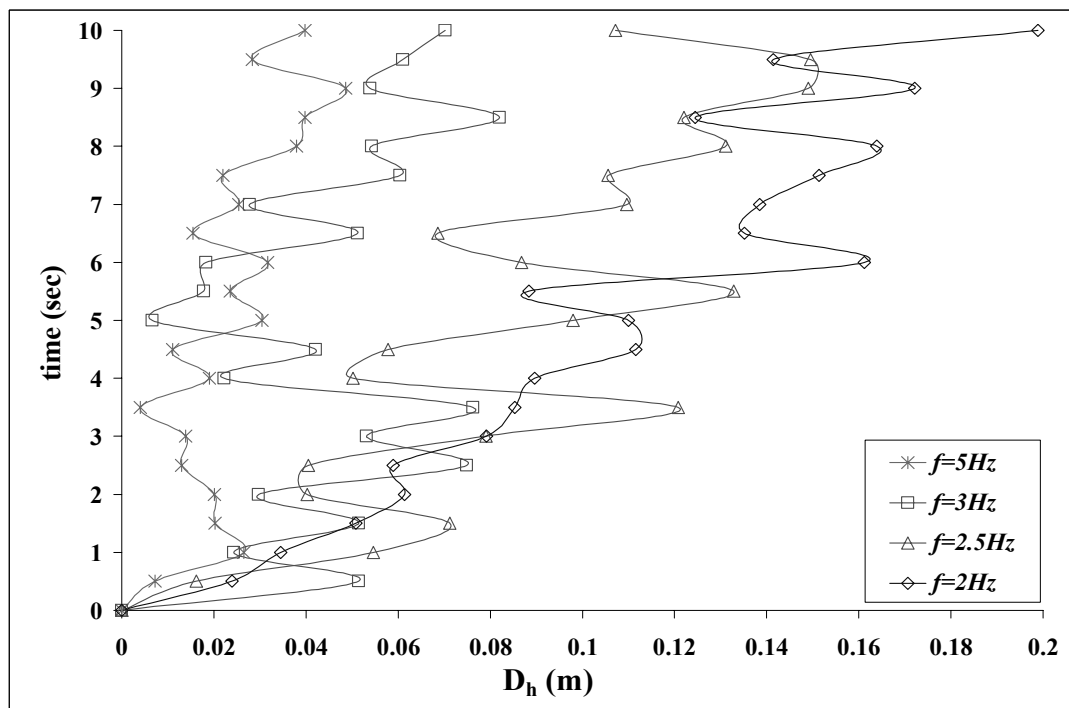


Figure 5.32. Average horizontal displacement ( $D_h$ ) of the five measurement points vs. time - influence of frequency.  $A = 1g$ .

Figure 5.32 displays the influence of frequency on structural response. There is no clear trend, though it seems that displacement increases with increasing period of motion (decreasing frequency), due to longer periods of high acceleration.

Searching for the best fit set of parameters for Avdat is not as straight forward as in the previous case of the arch at Mamshit. There is no merit in comparing total block displacements since the blocks move back and forth, and do not follow a consistent trend; their total displacement depends on the duration of motion, which is unknown. Furthermore, relative displacements between the blocks might obscure the observed total amount of displacement in the field and make the comparison meaningless.

Figure 5.33 and Figure 5.34 display the final result of two different runs, in which only the corner blocks are displaced while the rest of the structure remains intact. Both simulations were performed with no input vertical motions ( $A_v = 0$ ). In Figure 5.33 the horizontal PGA ( $A_h$ ) is 1g and frequency ( $f$ ) is 3Hz. The resulting horizontal displacement ( $D_{h\_avmax}$ ) is 8cm. In Figure 5.34  $A_h$  is 1.5g,  $f$  is 5Hz., and  $D_{h\_avmax}$  is 14cm. These two sets of parameters may represent the best approximation that can be reached with a 2-D, numerical, back analysis of the historical earthquake that caused the observed damage in Avdat. A determination of the single, best fit set of parameters to this case study is not attempted here because of the above mentioned limitations, although the graphical output in Figure 5.33 better fits field measurements.

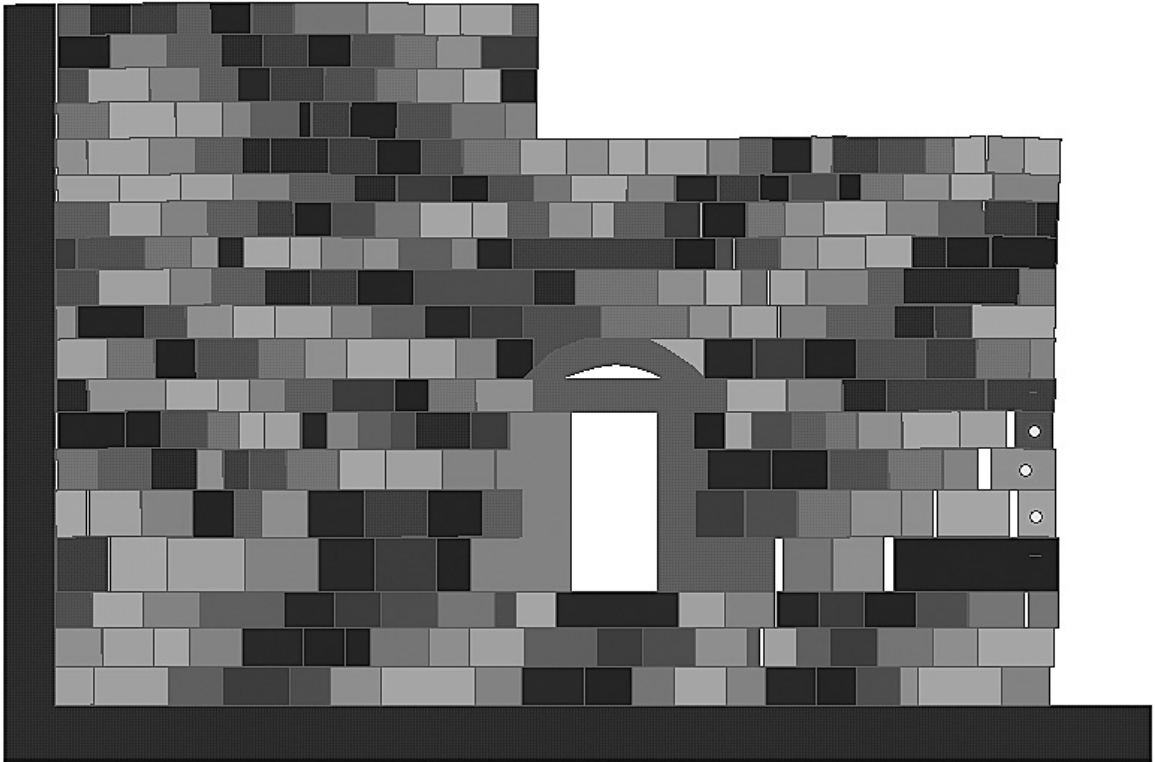


Figure 5.33. Graphical output of a simulation with  $A_h=1g$ ,  $A_v=0$ ,  $f=3\text{Hz}$ .  $D_{h\_av_{max}}=8\text{cm}$ .

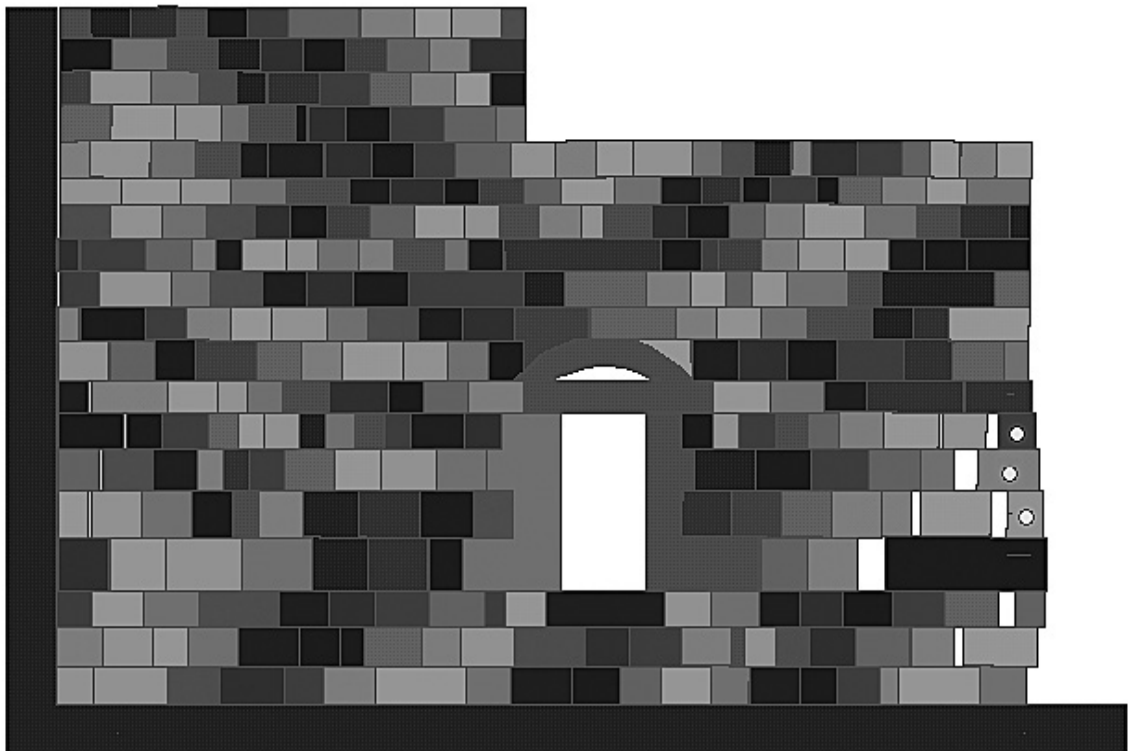


Figure 5.34. Graphical output of a simulation with  $A_h=1.5g$ ,  $A_v=0$ ,  $f=5\text{Hz}$ .  $D_{h\_av_{max}}=14\text{cm}$ .

#### 5.2.4 *Summary*

- The case of a square masonry building has been analyzed in both the analytical and the numerical approaches; both analyses are confined to a two-dimensional model of the problem. The case in which a group of blocks slides out of a corner of a masonry structure involves all three dimensions (westerly sliding out of a western wall), and therefore is not ideally treated with this kind of modeling.
- The very unique structural failure, in which mid-height blocks have been laterally displaced, is duplicated perfectly by dynamic DDA. The results provide an insight into the structural dynamic behavior, which could not have been achieved by a different analysis approach, certainly not by a pseudo-static approach.
- The best fit set of parameters is not determined conclusively since a finite comparison measure with a physical meaning, such as total displacement of a block for example, will not portray the failure mechanism properly for the following reasons:
  1. The blocks move back and forth, sometimes with no obvious trend, so total displacement is a matter of the capturing moment.
  2. The over-all response of the structure is as important as the localized measured displacement. For that matter, the graphical output of the deformed mesh configuration is as valuable as the quantitative data, since it enables us to understand the evolution of structural damage over time more clearly.

### 5.3 Masonry arch – results from Nimrod Fortress

#### 5.3.1 Background

##### Geography and Geology

Nimrod Fortress is built on an elongated spur descending from Mt. Hermon to Banias (Figure 1.2), comprised of middle Jurassic limestones (Hermon formation). At a height of 760m above sea level, and about 250m above its surroundings, the fortress is cut off by steep canyons from both north and the south and can be approached conveniently only from the east.

##### Archaeology and History

The fortress, also known as Qal'at Namrud or Al-Subayba, is the largest medieval fortress in Israel. It was built by al-Azîz 'Uthmân, the Ayyûbid governor of Banias, between 1228 and 1230 AD in order to protect the main road to Damascus from the crusaders. In 1260 it was conquered by the Mongols and partly destroyed. In the same year it passed into the hands of the Mamlûks and was rebuilt by the personal messenger of the Sultan Baybars, the Emir Badr al-dîn Bilik al-Khaznadâr (Ellenblum, 1989; Hartal, 2001).

Evidence of destruction caused by a severe earthquake can be seen throughout the fortress, and the damage is dated to be associated with one of the two large earthquakes of the year 1759 (Hartal, 2001). The main shock occurred on Nov 25, in the Beka'a Valley in Lebanon (33.7°N 35.9°E) and had a Magnitude of  $M_s=7.4$  (Ambraseys and Barazangi, 1989). It was preceded by a  $M_s=6.6$  foreshock on Oct 30, located between the Kineret and the Hula Valley (33.1° N 35.6° E) (Ambraseys and Barazangi, 1989). Both earthquakes caused great damage and loss of life to most of northern Israel and southern Lebanon (Ambraseys and Barazangi, 1989).

The most impressive evidence from the earthquake that has damaged the fortress can be observed in the gate tower (tower 11 in Figure 5.35), where three parallel arches and an arched passage-way, all display the same mode of failure, in which a single stone has slid downwards while the rest of the arch remained intact (Figure 5.37). The deformed arches are on the east-west plane

(i.e. facing north or south), while perpendicular arches have not suffered deformations (Figure 5.37.C).

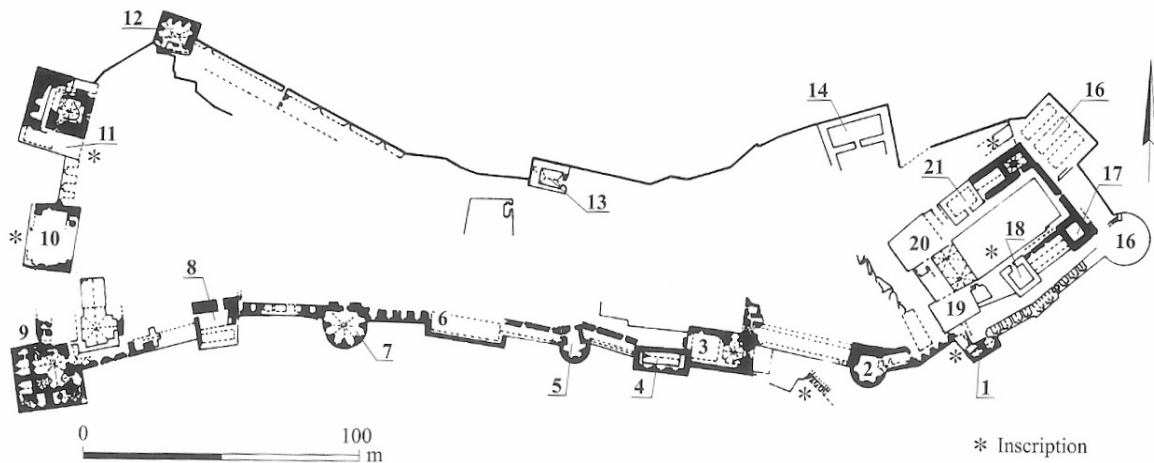


Figure 5.35. General plan of the Nimrod fortress (Hartal, 2001).

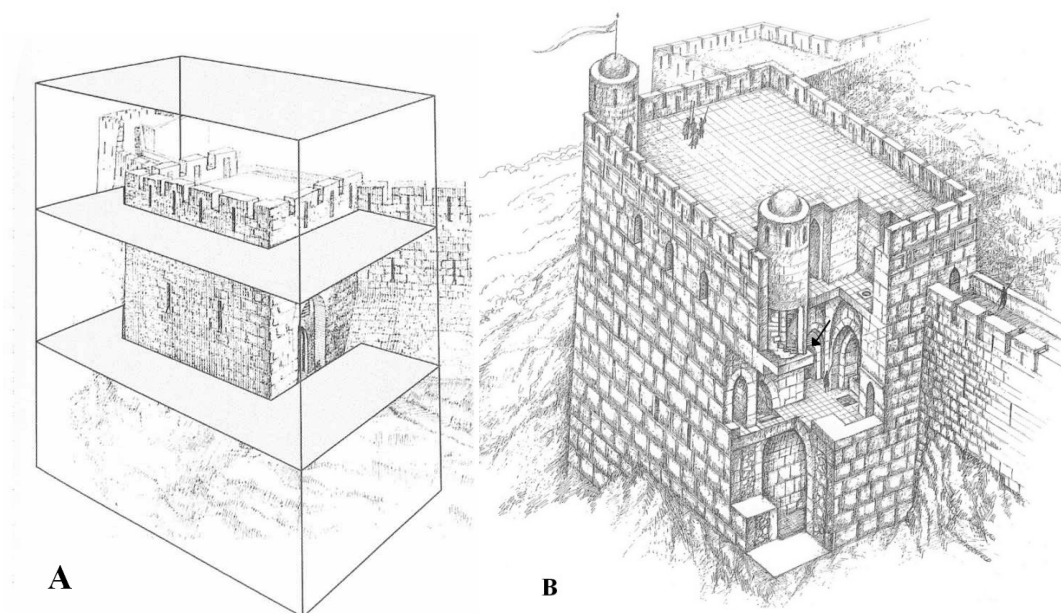


Figure 5.36. Schematic reconstruction of the gate tower (Hartal, 2001); **A.** Reconstruction outline of enlarged tower with original tower enclosed in it. **B.** Second phase of the tower. The black arrow points to the original gate.

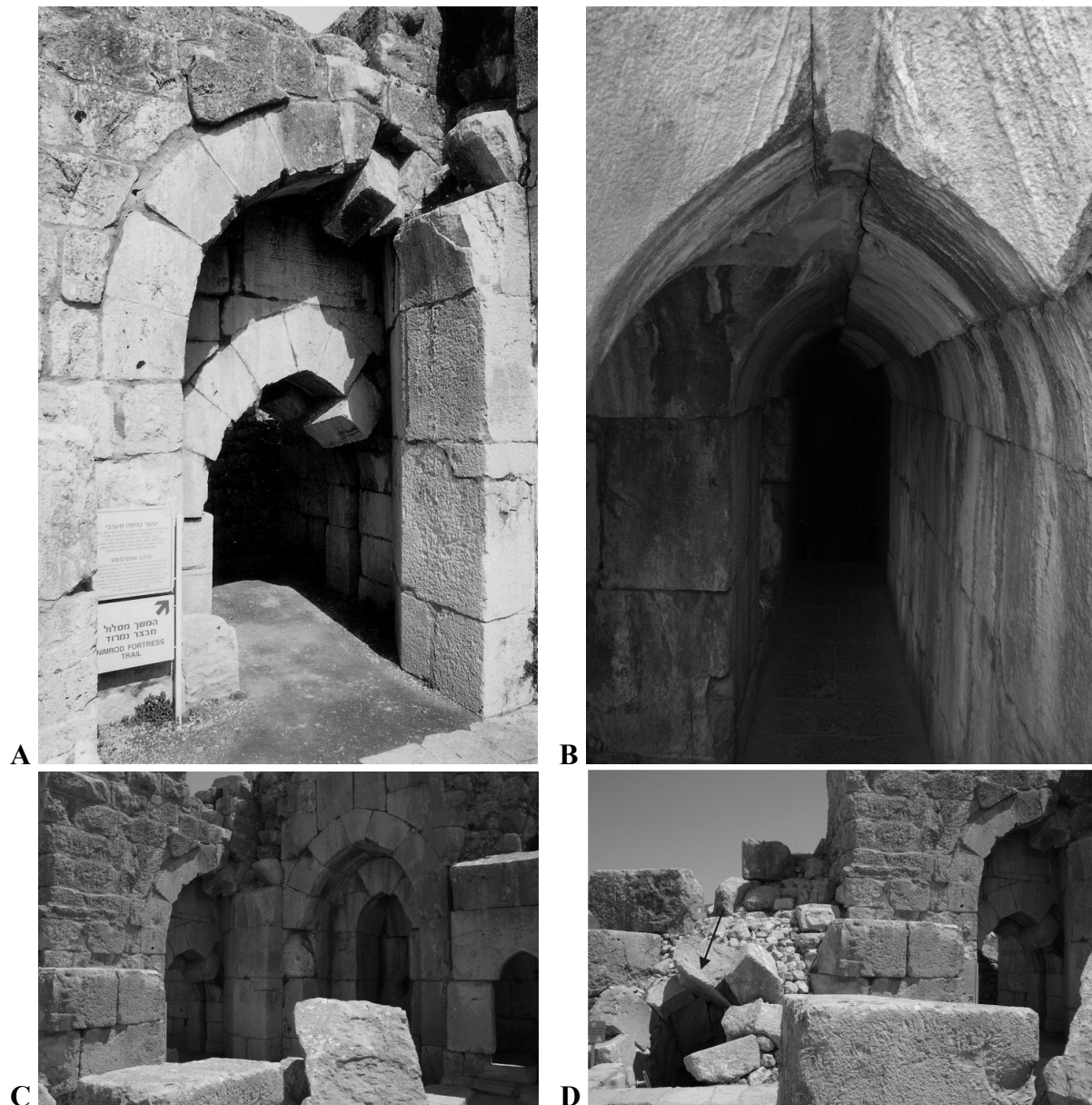


Figure 5.37. Evidence of the earthquake at the gate tower; **A**. The same stone has slid downwards out of three parallel arches at the main gate arch. **B**. A similar deformation is noticed at a passage-way parallel to the gate arch. **C**. The adjacent arch facing to the east was not deformed. **D**. Location of the passage-way, 10 meters west (left) of the main gate.

### The analyzed structure

The Ayyûbid phase of the tower is 14.30 x 14.30m in size, consisting of one chamber only and with 2.50-3.70m thick walls, built directly on bedrock, on the edge of a steep cliff.

The Mamlûk phase of the tower has completely altered its appearance. The gate tower was supported on three sides by retaining walls, thus enabling its extension to the north, west and south. The previous tower ceased functioning as a gate and served as an inner room in the

enlarged tower, which had three floors and has probably served as Bilik's palace (Hartal, 2001). The walls of the second phase of the tower completely differ from those of the first. They are built of huge ashlar, measuring 1.30 x 1.80 x 1.20m and more, and weighing between 5 and 37 tons. For the purpose of comparison, the stones of tower 11 are 14 times larger than the normalized stones from the same period elsewhere in the site. The stones used for both phases of the tower were quarried nearby. The western wall, which was the highest retaining wall, is 30m above the foot of the cliff (Hartal, 2001).

The large earthquake that destroyed the fortress triggered the collapse of the massive walls and of the entire second floor (Hartal, 2001).

Of the 3 parallel arches composing the gate to the tower, and the nearby arched passage-way, only the lower outer arch is analyzed as a representative case. A more extensive analysis for the structure as a whole is possible only in a three dimensional analysis.

A detailed map of the lower outer arch is presented in Appendix 2.

An analytical solution to this case is not attempted, since the analytical solution described in section 2.1.4 is valid only for semi-circular arches.

### 5.3.2 *Numerical solution*

The block system, displayed in Figure 5.38 was generated using program DC of DDA, and includes the arch confined by a block on its right. Material lines intersect the arch blocks in order to examine the influence of wall stiffness on structural response.

The confining block was added in order to simulate the geographical constraints at the site: the fortress is built on an elongated range, cut off by deep canyons from three sides. As a result, the gate tower is supported by a 30m high retaining wall on its western side, while the eastern side

rests directly on bedrock. This causes asymmetries in structural response, and possibly seismic wave amplifications in preferred orientations.

Figure 5.39 displays the sign convention for the five measurement blocks, used for reference later in this work.

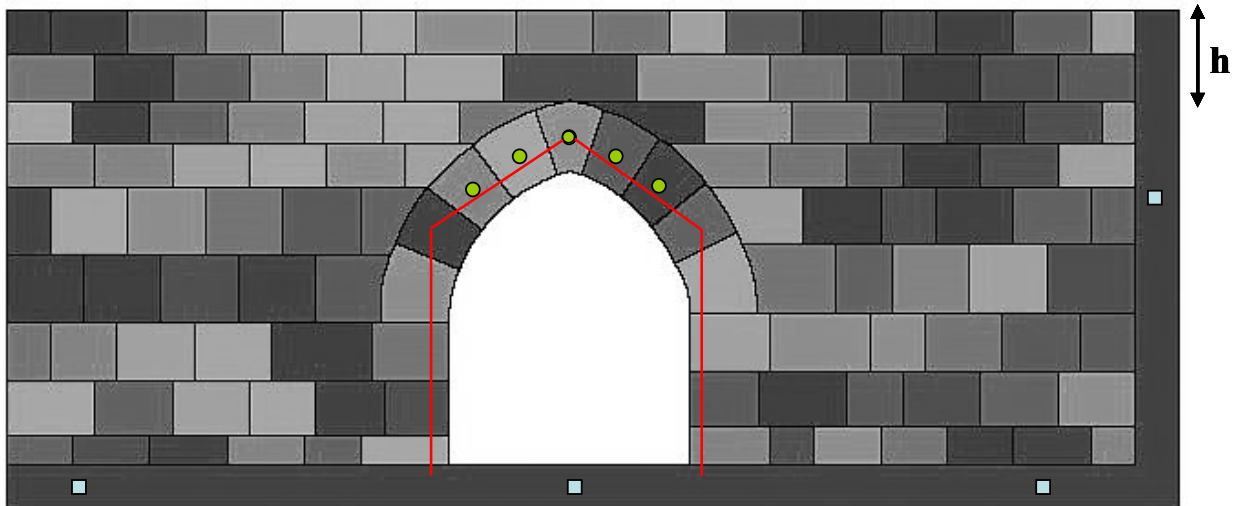


Figure 5.38. The final DDA block system for the arch at Nimrod Fortress. four fixed points (squares) are assigned to the confining block, and five measurement points (circles) are assigned to the top arch blocks. The height of the wall above the arch is  $h$ . the lines intersecting the arch blocks represent material lines.

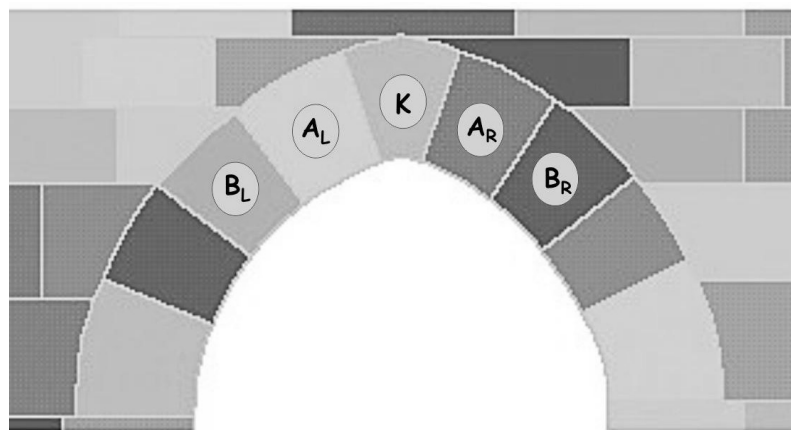


Figure 5.39. Convention for arch blocks – K for keystone, A and B for the first and second block from the keystone respectively, and R or L to indicate right or left.

A sensitivity analysis for the block system presented in Figure 5.38 was performed. Overburden, wall stiffness, and motion parameters (Amplitude and frequency) were examined, and results are presented in Figure 5.40 to Figure 5.49. All simulations were performed with 1% damping with a synthetic sinusoidal acceleration record as input (Figure 5.14) in qk. mode. The full list of DDA

runs is presented in Appendix 3.3. The mechanical parameters are specified in Table 3.1, and the stiffness of the surrounding wall is 5.4MPa unless mentioned otherwise.

As a result of the confining wall on the right side of the block system the whole structure is gradually displaced to the left. In order to display correctly the displacement of block  $A_r$ , which is of our interest, in relation to the displacements of the whole structure, the comparison parameter for the sensitivity analysis was taken as the relative displacement of  $A_r$  to the average displacement of the other 4 blocks, normalized to the keystone displacement.

The following equations present the derivation of the comparison parameter, in which horizontal inward displacement was considered to be positive (left for  $A_r$  and  $B_r$  and right for  $A_l$  and  $B_l$ ) and vertical displacement remains in usual convention (up is positive):

$$u_{iR}^* = -(u_{iR} - u_k), u_{iL}^* = u_{iL} - u_k, v_i^* = v_i - v_k \quad (5.4)$$

$$u^*_{AV} = \frac{\sum u_i^*}{4}, v^*_{AV} = \frac{\sum v_i^*}{4} \quad (5.5)$$

$$\bar{u} = u(A_R) - u^*_{AV}, \bar{v} = v(A_R) - v^*_{AV} \quad (5.6)$$

where  $u_i^*$  and  $v_i^*$  are normalized horizontal and vertical displacements respectively, and  $\bar{u}$  and  $\bar{v}$  are the relative displacements of block  $A_r$ , used as the comparison parameter in Figure 5.44 to Figure 5.47.

Figure 5.40 and Figure 5.41 show the displacement of all 5 blocks over 40 seconds. The first figure in each (A) displays measured displacements (horizontal vs. vertical) of the blocks, while the second figure (B) displays the normalized displacements. It can clearly be seen in both figures that the final inward displacement of  $A_r$  is much larger than that of the other blocks. It can also be seen in Figure 5.40.B that both inner blocks -  $A_l$  and  $A_r$  - are displaced inwards, while  $B_r$  and  $B_l$  are displaced outward, and in Figure 5.41.B that the final displacement of the right side –

$A_r$  and  $B_r$  – is larger than that of the left side. This behavior could not have been easily detected from the measured displacement plot (Figure 5.40.A), thus emphasizing the compatibility of the normalized displacement as the comparison parameter.

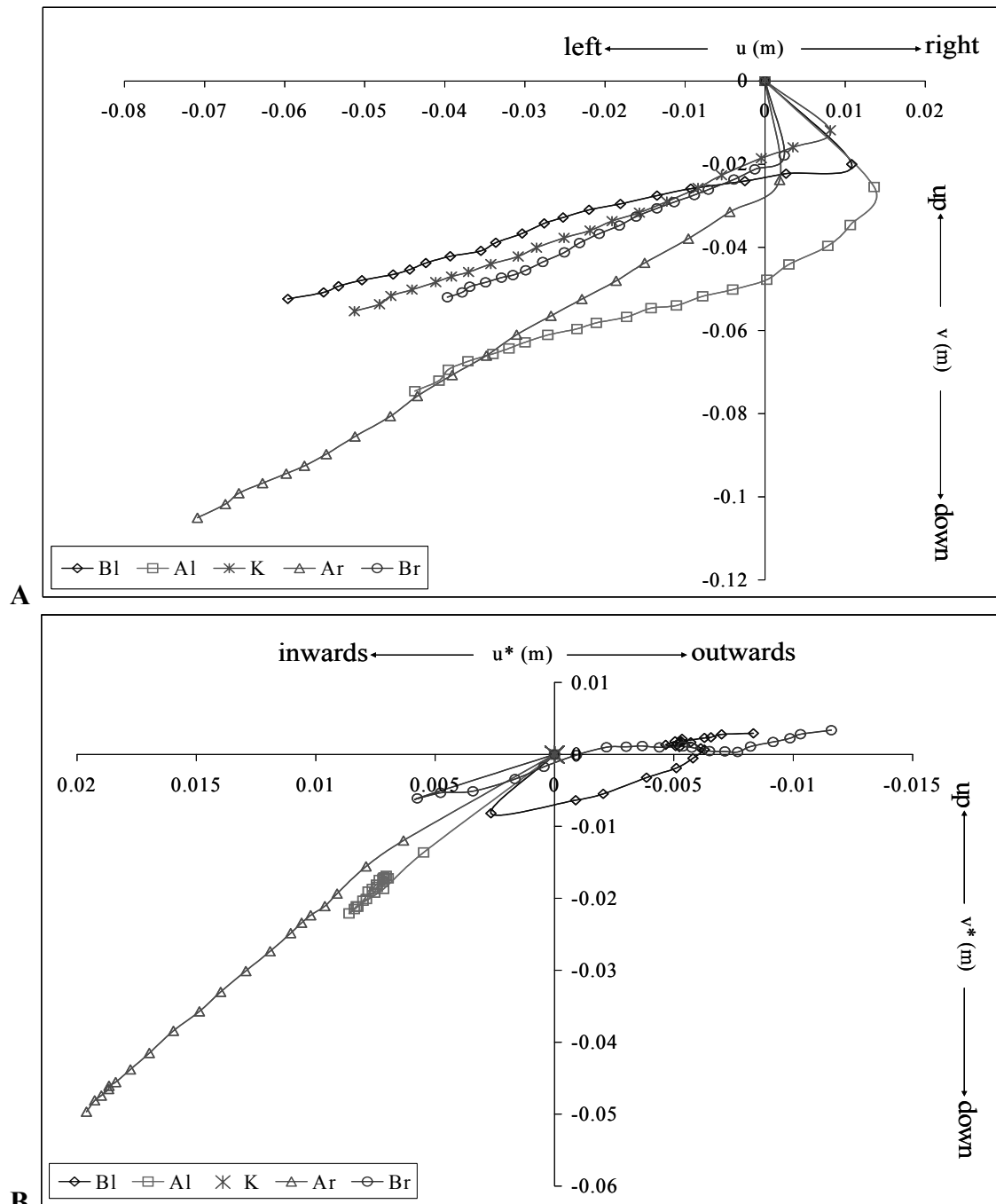


Figure 5.40. Spatial displacement of the 5 blocks over 40 seconds with  $A=1g, f=1\text{Hz}$ . Each symbol represents 2 seconds. **A**. measured displacements **B**. normalized displacements.

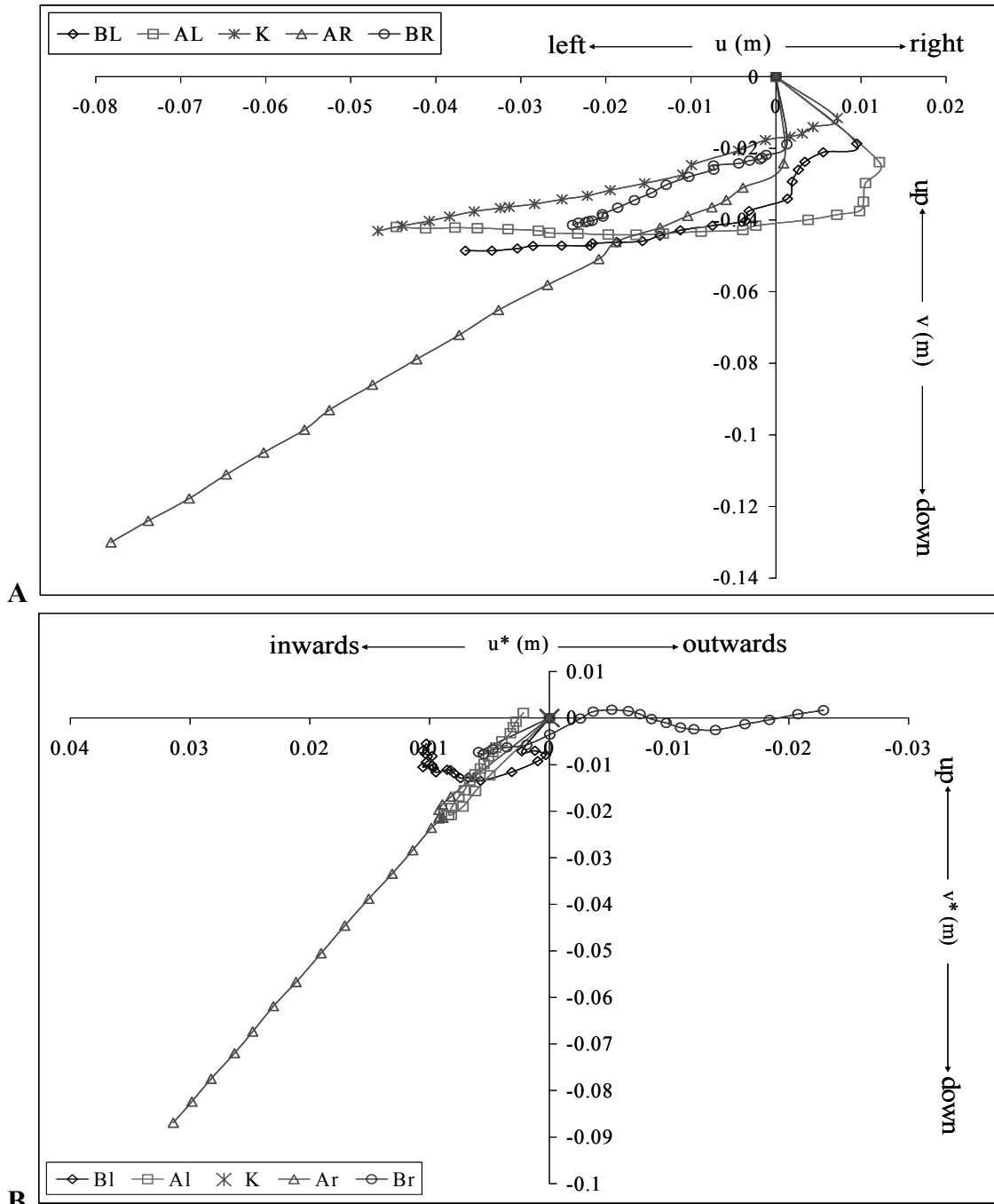


Figure 5.41. Spatial displacement of the 5 blocks over 40 seconds with  $A=1g$ ,  $f=2\text{Hz}$ . Each symbol represents 2 seconds. **A.** measured displacements **B.** normalized displacements.

Additionally, block velocity can be easily tracked: in the 40sec. runs the distance between two adjacent symbols represents two seconds. If the distance between the symbols is constant then the block maintains constant velocity. When the block stops there is superposition of symbols as the block stays in the same place over time. Examining the displacement curve of Block  $A_i$  in

Figure 5.40.A and B shows the difference between the two figures: in Figure 5.40.A it seems as if Block  $A_l$  moves in constant velocity, while in Figure 5.40.B it seems to have stopped after a while. This is because the block moves in the exact same velocity as Block  $K$ , and therefore its relative velocity to Block  $K$  is zero, and the symbols in Figure 5.40.B superimpose each other.

The final block position for the cases described in Figure 5.40 and Figure 5.41 is graphically displayed in Figure 5.42 and Figure 5.43, respectively.

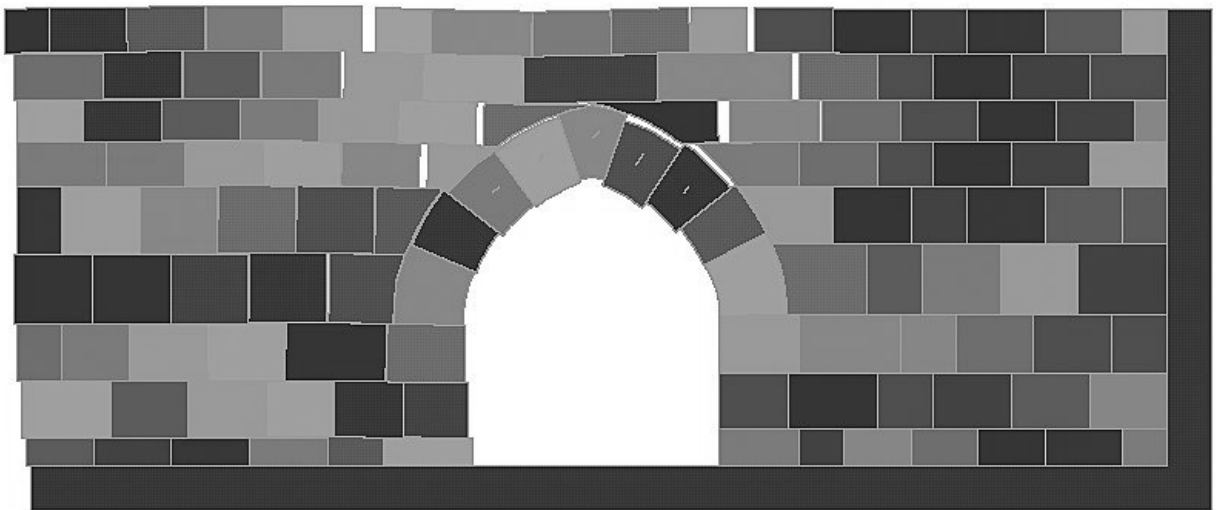


Figure 5.42. Graphical output of a simulation with  $A=1g$ ,  $f=1\text{Hz}$ .

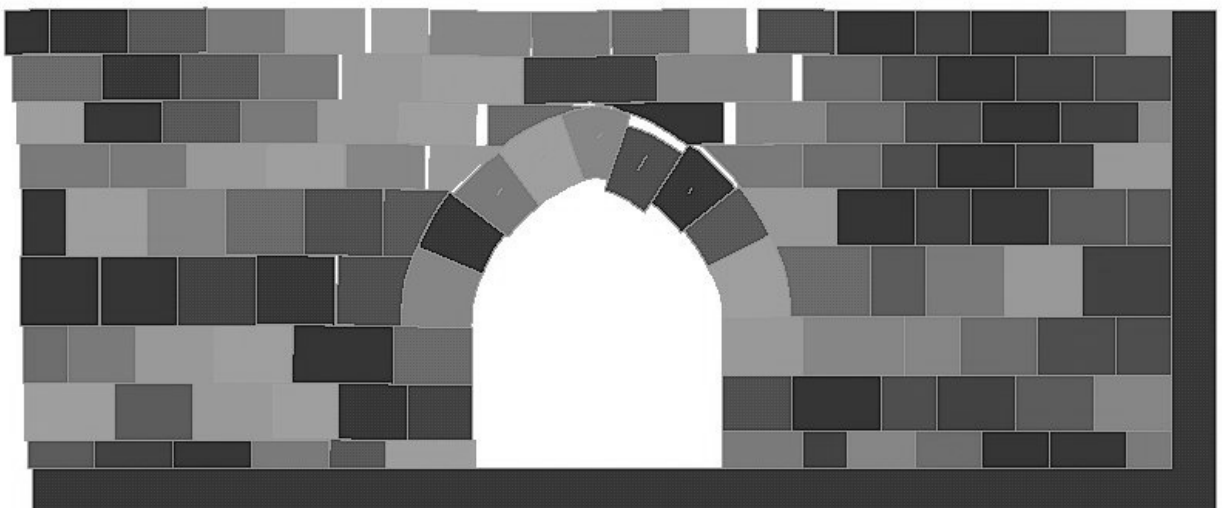


Figure 5.43. Graphical output of a simulation with  $A=1g$ ,  $f=2\text{Hz}$ .

Figure 5.42 shows the case of  $A=1g$ ,  $f=1\text{Hz}$ , the larger displacement of the inner blocks (A) is shown clearly. Figure 5.43 shows the case of  $A=1g$ ,  $f=2\text{Hz}$ . Both the graphical display and the data imply that this is the best fit for the structural failure displayed in the field, as shown in Figure 5.37.A.

Figure 5.44 displays the structural response to different amplitudes, under a constant frequency of  $f=2\text{Hz}$ , for 40sec. The measured displacements for the whole arch are much larger for the case of  $A=1.5g$ , resulting in a smaller normalized relative displacement for  $A=1.5g$  than for  $A=1g$ .

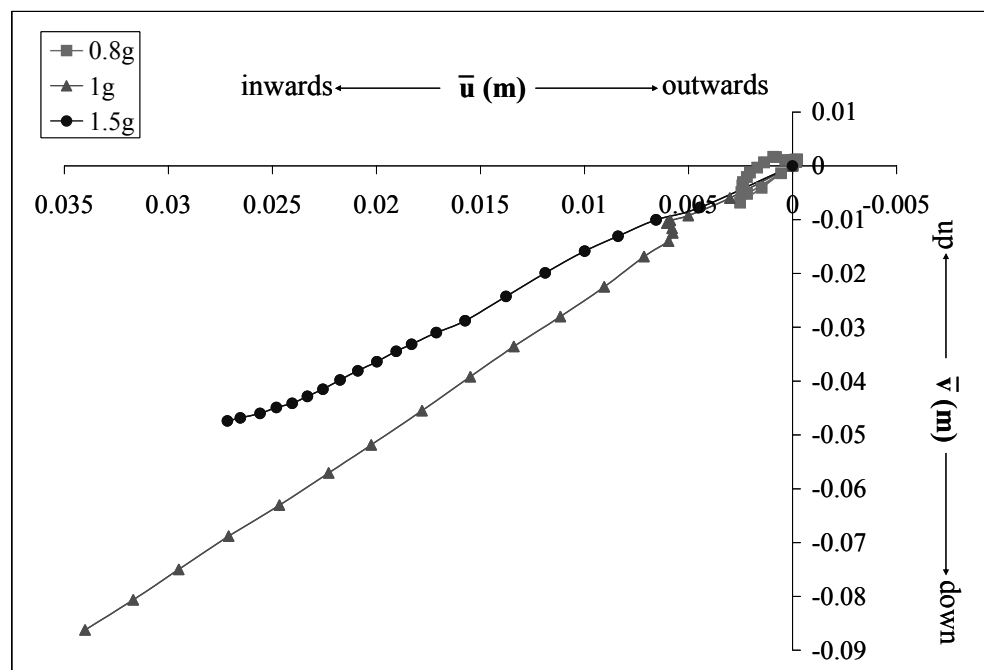


Figure 5.44. Relative normalized spatial displacement of Block  $A_r$  - influence of amplitude.  $f=2\text{Hz}$ .

Figure 5.45 displays the structural response to different frequencies, under a constant amplitude of  $A=1g$ , for 40sec. Block  $A_r$  is displaced in the same direction and trend in all frequencies, but the displacement rate (each symbol is 2 seconds), and consequently the total accumulating displacement are much larger for  $f=2\text{Hz}$ .

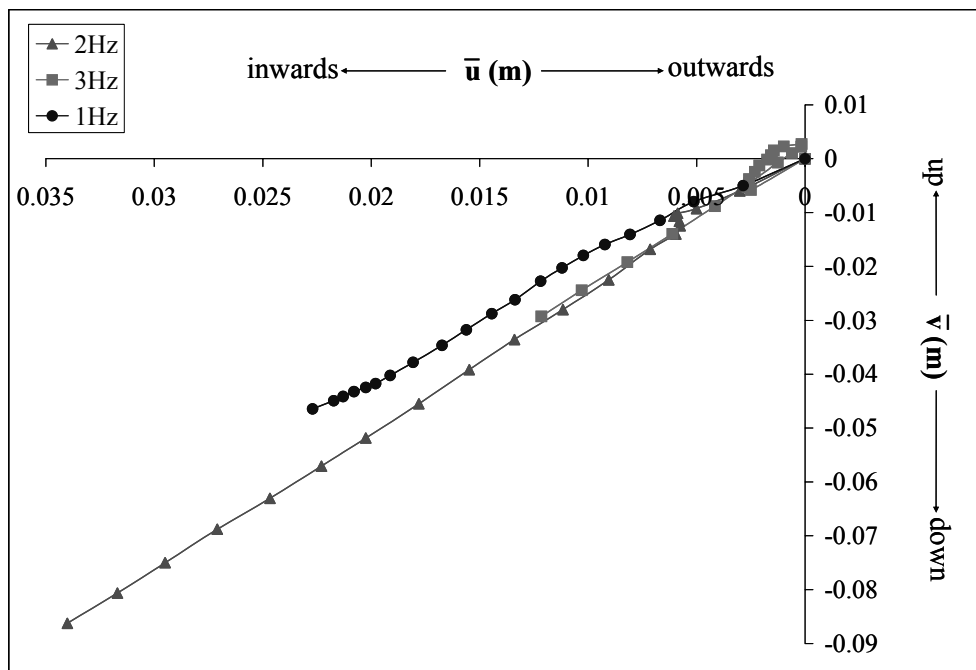


Figure 5.45. Relative normalized spatial displacement of Block  $A_r$  - influence of frequency.  $A = 1g$ .

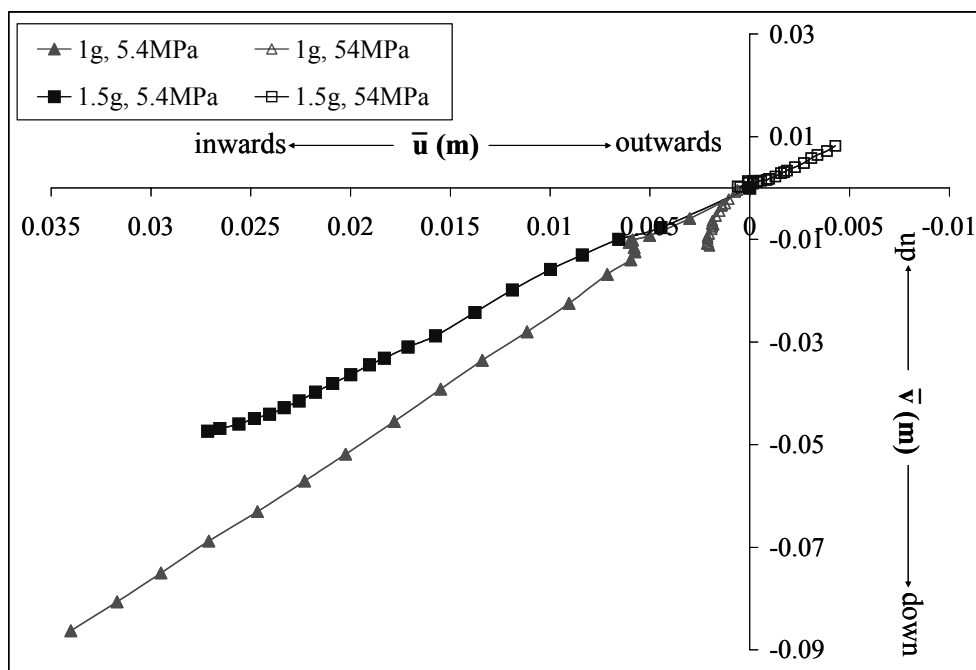


Figure 5.46. Relative normalized spatial displacement of Block  $A_r$  - influence of wall stiffness.

Figure 5.46 displays the structural response to different wall stiffness, under two sets of motion parameters, over 40sec. It can be seen that a soft wall allows the structure the flexibility it needs for Block  $A_r$  to move out considerably more than the other blocks. When the wall is stiffer, still 3

orders of magnitude softer than the arch stones, the blocks move together, and the unique mode of failure is not obtained.

Figure 5.47 displays the structural response to overburden. The difference between  $h=0$  and  $h=0.82\text{m}$  (two rows above the arch) is not evident, in both cases the relative normalized displacement of Block  $A_r$  seems to trend inwards almost by the same amount. Figure 5.48 and Figure 5.49 in which displacements of all blocks for  $h=0$  is displayed reveal that all the blocks are displaced inwards symmetrically and by the same amount with respect to their relative location in the arch.

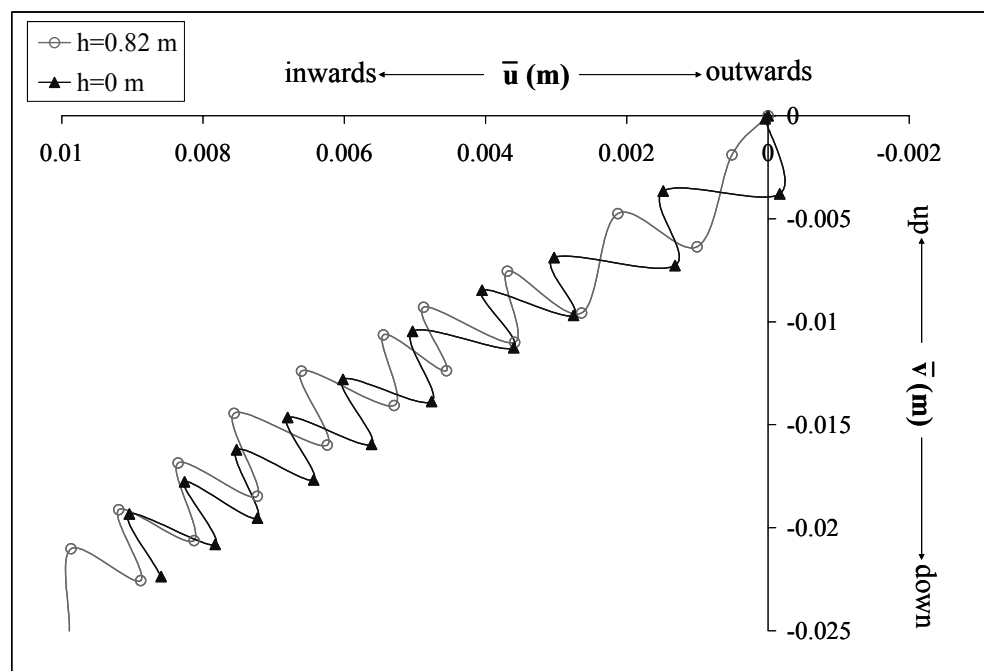


Figure 5.47. Relative normalized spatial displacement of Block  $A_r$  - influence of overburden.  $t=10$  sec,  $A=1.5g$ ,  $f=3\text{Hz}$ .

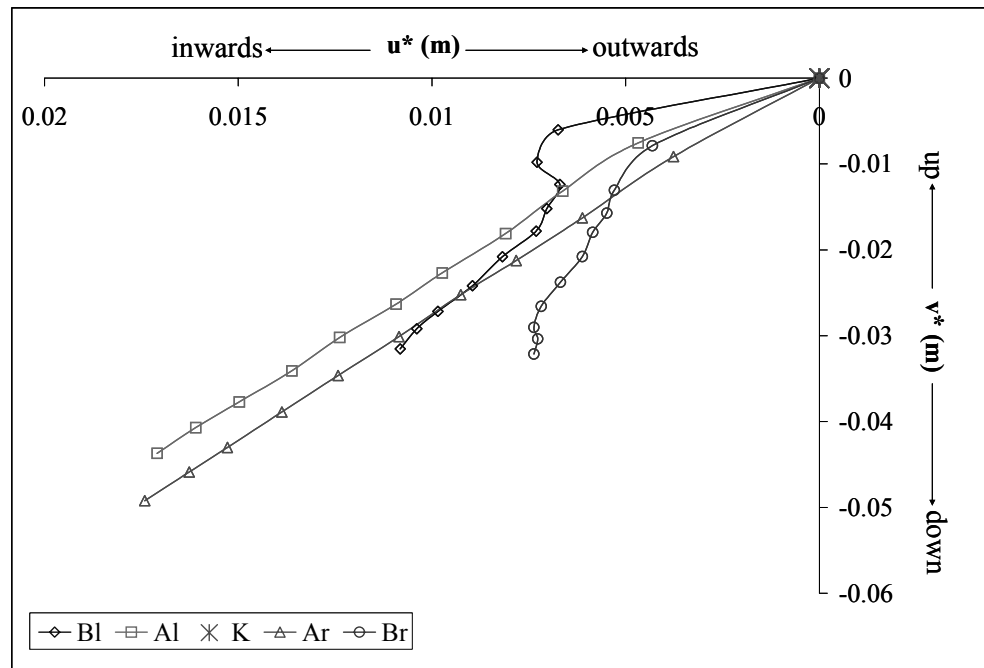


Figure 5.48. Normalized spatial displacement of the 5 blocks over 10 seconds with  $A=1.5g$ ,  $f=3\text{Hz}$  and  $h=0$ .

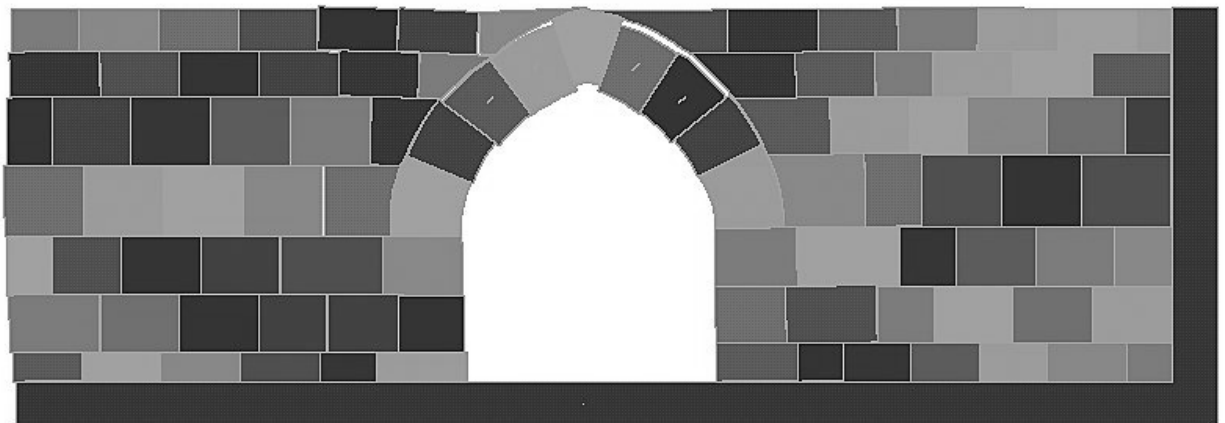


Figure 5.49. Graphical output of a simulation with  $A=1.5g$ ,  $f=3\text{Hz}$  and  $h=0$ .  $t=10$  sec.

In the case of Nimrod therefore, it seems that the relief of overburden stresses does not accelerate the observed failure pattern. Furthermore, field evidence shows different amounts of overburden for the four separate arches that present this failure mechanism (Figure 5.37); they have all experienced some relief of overburden but not up to  $h=0$ .

The sensitivity analysis has shown that the best fit parameters for the case of Nimrod Fortress are  $f=2\text{Hz}$  and  $A=1g$ . These parameters were used once more to examine the structural behavior of

block  $A_r$  with time. A two minute long input motion was applied to the structure in order to check if block displacement continues to accumulate at a constant rate (as obtained numerically up to 40 seconds of motion – Figure 5.44) or if it stops as obtained numerically in the case of the keystone at Mamshit.

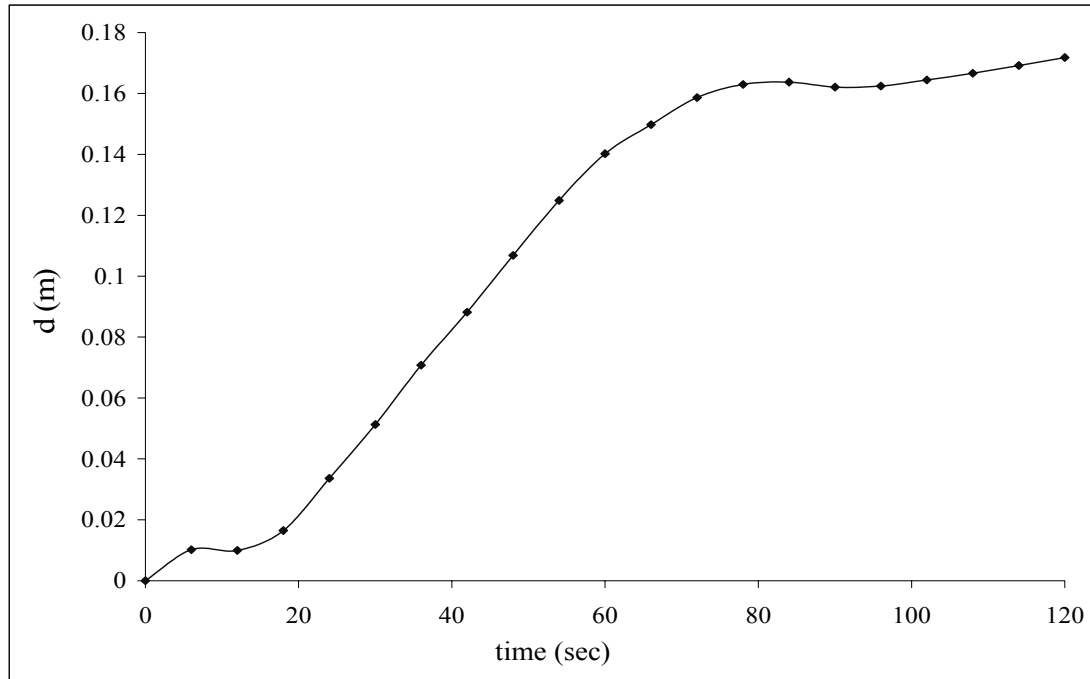


Figure 5.50. Normalized displacement of stone  $A_r$  in the direction of the displacement vector over time ( $d = \sqrt{u^2 + v^2}$ ). After approximately 70 seconds the displacement stops and the structural deformation is ‘locked’.

Figure 5.50 shows that the displacement of block  $A_r$  progresses at a constant velocity of about 3mm/sec between 20 and 70 seconds of the input motion; the displacement is later restrained by structural constraints and the deformation is ‘locked’ with approximately 17 cm of inward displacement. Note that the maximum block displacement prediction by DDA (17cm) is slightly smaller than the 23 cm observed in the field (Appendix 2.3).

The numerical analysis results may be used also to provide constraints on the duration of shaking. Recall that Ambraseys and Barazani (1989) estimated a duration of 50 seconds for the

$M_s=7.4$  earthquake, which occurred on Nov 25, 1759. This estimate seems reasonable in light of the numerical analysis results,

The results obtained for Nimrod by numerical analysis further demonstrate the deformation mechanism which was first detected in Mamshit, namely that the arch attains a kind of an equilibrium during shaking during which keystone displacement may be arrested, leading to “structural locking” of the arch. This “structural locking” mechanism, which seems to develop *during* shaking, can explain the ability of the studied masonry arches to withstand strong earthquakes in the past.

### 5.3.3 Summary

The gate tower at the Nimrod Fortress is an example case for an earthquake-damaged archaeological site, since the structural damage is both repetitive and preferably oriented, and the earthquake is dated accurately. Therefore, a quantitative structural analysis can provide further insight to an already well-studied problem.

Nevertheless, geographical and structural asymmetries complicate the analysis and limit it in the following ways:

- Boundary conditions for the DDA model must be defined accurately for best simulation of the geographical setting
- Failure asymmetry is harder to obtain numerically
- A non semi-circular arch can not be analyzed pseudo-statically

1. Under these limitations, the DDA model for the Nimrod fortress was modeled with a confining block on its right, which allowed simulation of an asymmetrical failure, as observed in the field. The sensitivity analysis suggests best fit input motion parameters of:  $f=2\text{Hz}$ ,  $A=1\text{g}$ .

2. The best fit was obtained with a wall stiffness of 5.4MPa – 4 orders of magnitude lower than the stiffness of intact block material. Since evidently the wall is not heterogeneous, the low stiffness in the DDA model must compensate for another energy dissipation mechanism, not taken into account in DDA. Such a mechanism may take place in “corner chipping” (Figure 5.51) observed throughout the site. Such a mechanism, which consumes energy, is not expressed in DDA’s “simply deformable” blocks.



Figure 5.51. Corner chipping is seen in many of the rocks at the gate tower – an energy dissipation mechanism which can not be imitated with DDA.

3. As in the Avdat case, the real displacements of the blocks are more complex than can be truly simulated with a 2-D model. Rotation, for example, is not treated in this analysis and its consideration may result in a slightly different set of ‘best fit’ parameters.

## 6 Discussion and Conclusions

This work presents a new method for seismic risk evaluation, in which historical, earthquake-induced, structural failures are analyzed quantitatively using analytical and numerical solutions. In the research presented in this thesis, both pseudo-static and fully dynamic analyses were performed after an accurate block system was generated with adequate boundary conditions and material properties. The generated block system was subjected to either pseudo-static inertia forces or dynamic loading functions as direct input.

Three archaeological sites in Israel were investigated using the new method and results were discussed in terms of displacement evolution of selected structural elements in the studied masonry structure. In all three sites the observed failure in the field was duplicated very successfully by 2-D DDA. While pseudo-static results were found irrelevant and highly unsatisfactory, sensitivity analyses of numerical results did provide quantitative constraints on historical ground-motion parameters in the studied sites. Furthermore, the block displacement data as well as the general deformed mesh configuration provided some insight into the response of masonry structure to earthquake-induced shaking.

### 6.1 Discussion - seismological implications of results

The two southern sites: Avdat and Mamshit, are dated back to the 3<sup>rd</sup> and 4<sup>th</sup> centuries AD, and may therefore have been subjected to more than one earthquake tremor in their history. Furthermore, since population in that area has always been scarce, accurate dating of events, determination of epicentral location, and resolution of earthquake magnitude are rare, if not non-existent for events that took place before the 20<sup>th</sup> century. Therefore, the results obtained from

the dynamic analysis for Avdat and Mamshit may only be compared with the values suggested in Israel building code #413 generated by the Geophysical Institute of Israel (GII) (Figure 1.1 and Table 6.1).

The damage at the Nimrod Fortress on the other hand is dated quite accurately and is associated with one of the two big earthquakes of 1759:

On Nov 25, 1759, an  $M_s=7.4$  earthquake produced surface faulting (at least 100 Km) along the Yammouneh fault in the Bekka Valley. It lasted about 50 seconds, caused heavy destruction and great loss of life in numerous villages and towns, including Safed, Damascus, and Beirut, and was felt as far as 1100 Km away (Ambraseys and Barazangi, 1989).

It was preceded by an  $M_s=6.6$  foreshock on Oct 30, 1759, which almost destroyed Safed and Qunaitra and killed 2000 people. The shock was felt as far as Jerusalem and Gaza and caused a seismic sea wave that flooded Acre and docks at Tripoli (Ambraseys and Barazangi, 1989).

The maximum damage zone of the Oct shock was located initially by Sieberg (1932) between the Sea of Galilee and the Hula Valley and was later associated with surface faulting found at the Ateret Crusader castle on the Jordan river gorge and in a palaeoseismic trench study in the Jordan fan–delta at the Bet-Zayda Valley, some 12 km south of Ateret, both of which show  $0.5\text{m} \pm 0.1\text{m}$  left-lateral slip (Ellenblum et al., 1998; Marco et al., 2005). Based on empirical relations, this shock may have ruptured 15-20 Km along the Jordan gorge (Ambraseys and Jackson, 1998; Marco et al., 2005).

To determine the PGA caused by these earthquakes at the Fortress of Nimrod, and possibly determine which of the two shocks might have caused larger damage at the site, the same attenuation relationship (Boore et al., 1997) used for seismic risk assessment by the GII (Shapira, 2002) is used here:

$$\ln A = -0.055 + 0.525(M-6) - 0.778 \ln r \quad (r^2 = R^2 + 31.02) \quad (6.1)$$

where  $A$  is the PGA,  $M$  is the Moment Magnitude ( $M_w$ ) and  $R$  is the distance to the fault plane.

In order to convert the surface-wave Magnitude provided by Ambraseys into moment-Magnitude as required for the attenuation relationship, two empirical relationships were used:

$$\log M_0 = 1.5M_s + 9.1 \quad (\text{Purcaru and Berckhemer, 1978}) \quad (6.2)$$

$$M_w = 0.67 * \log M_0 - 6 \quad (\text{Hanks and Kanamori, 1979}) \quad (6.3)$$

where  $M_0$  is the seismic moment in N\*m.

The attenuation law yields the following results with respect to the case of Nimrod (see also Table 6.1):

- For the October event:  $R=35 \pm 5$  Km,  $M_w=6.67$ ,  $A=0.084 \pm 0.01$  g.
- For the November event:  $R=60 \pm 5$  Km,  $M_w=7.47$ ,  $A=0.084 \pm 0.03$ g.

Table 6.1. Comparison between peak horizontal ground acceleration values obtained with different methods for the three case studies.

	Avdat	Mamshit	Nimrod Fortress
Israel Building Code #413 *	0.089g	0.11g	0.25g
Attenuation relationships **	-	-	0.08 $\pm$ 0.03g
DDA ***	1 $\pm$ 0.2g	0.5 $\pm$ 0.2g	1 $\pm$ 0.2g

\* Values are obtained through the GII web-site where errors are not indicated.

\*\* The error may results from distance measurements, the possible error in the Magnitude calculation is not indicated in the source.

\*\*\* Values are determined from the sensitivity analysis presented in chapter 5. It is shown that there is great sensitivity to frequency; therefore acceleration amplitude can not stand alone. The error might result from the large steps in the amplitude sensitivity analysis; larger accuracy can be examined in further research.

Table 6.1 shows great differences between the acceleration values obtained in this study and values that would be obtained by empirical attenuation relationships or suggested building standards. The discrepancy could result from a number of reasons:

1. The values suggested by Israel building code #413 are calculated for a return period of 475 years, whereas the analyzed structural failures might belong to a stronger event with a longer return period.
2. Building codes present bedrock peak ground acceleration, which may be amplified significantly at the structure itself due to rock – structure interactions. Figure 6.1 shows the suggested response spectrum in Israel building code #413 (1998). The three structures that were analyzed in this research are founded on bedrock, represented by the  $S_1$  curve. The largest predicted amplification is 2.5 times the bedrock PGA, at the natural periods of the structure. Although determination of the natural period of the studied structures was not attempted in this research it may be assumed nevertheless that structural amplifications may be responsible, in part, to the discrepancies between DDA "quake" mode results and the values suggested by the building code. That is because application of "quake" mode does not allow for wave propagation phenomena to take place when the motion is transferred from bedrock to the structure,

3. Topographical and other site-specific effects are not calculated, while all three archaeological sites are located on elevated hills above their surroundings, from a few tens of meters at Mamshit to 250m at Nimrod. Topographical effects of up to 4 were found in four sites in Israel in the frequency range of 1.3-4 Hz (Zaslavsky and Shapira, 2000), meaning that amplification of 5-10 at Mamshit and Nimrod for the frequencies that were obtained in the analyses are very reasonable.
4. The DDA values presented in Table 6.1 are of the required horizontal acceleration only. Additional vertical accelerations at Avdat may have reduced significantly the required horizontal accelerations obtained by DDA. Thus, a factor of over 10 between DDA results and the building code values is not unreasonable.

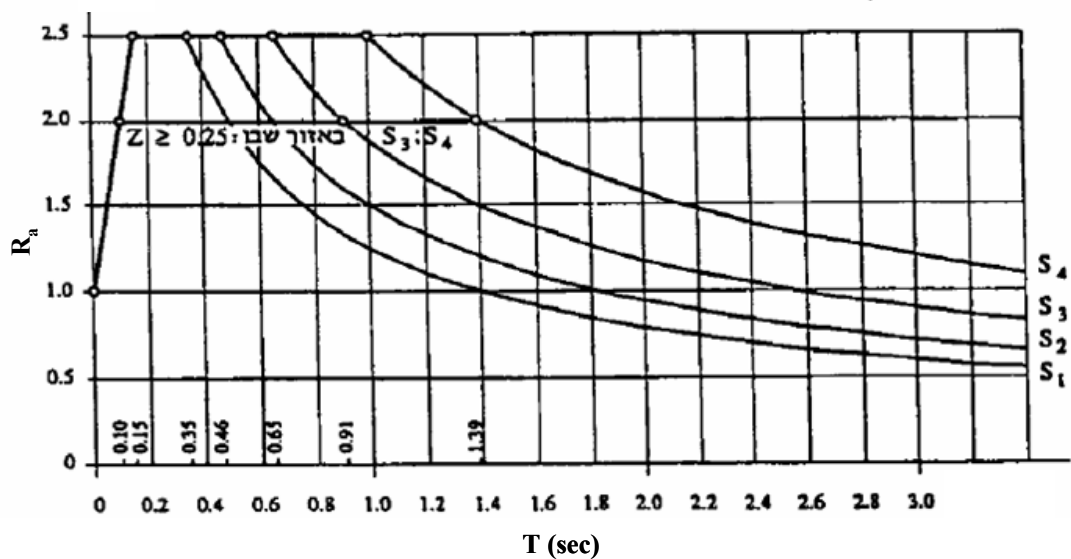


Figure 6.1 The suggested response spectrum in Israel building code #413 (1998). The spectral amplification coefficient ( $R_a$ ) is plotted against the natural period ( $T$ ) of the structure. All three structures in this study are founded on bedrock, thus behaving according to the  $S_1$  curve. The maximum structural amplification reaches 2.5 times the bedrock PGA.

## 6.2 Limitations and advantages of the new method

### 6.2.1 Limitations

- Boundary conditions, as well as numerical control parameters must be defined accurately for an adequate simulation of geographical and geometrical setting. Furthermore, the DDA numerical control parameters (e.g.  $g_0$ ,  $g_1$ ,  $g_2$ ) still must be optimized for each block system and dynamic loading function.
- Both pseudo-static and dynamic analyses were performed in 2D. In the case of the arch at Mamshit the observed displacement is one directional and a 2D model of the problem is quite representative. The other two cases however, involve plane rotations and therefore can not be modeled completely with a two-dimensional solution.
- Sensitivity analyses were performed with a synthetic sinusoidal loading function as direct input, consisting of a single amplitude and frequency value. This is obviously not the case of a real earthquake which is a train of various frequencies at different amplitudes. Nevertheless, the results presented in Figure 5.19 indicate that structural response does not vary all that much when inducing the structure with a real earthquake record.
- The ‘displacement’ mode, validated successfully in section 4.2 for a two block case, does not provide satisfactory results in a more complex block system. The best mode of input motion for structural analysis was found to be the ‘quake’ mode in which all block centroids are loaded with time dependent accelerations simultaneously. While this loading mechanism is reasonable for a jointed rock mass, it is less adequate for masonry structures that are founded on bedrock, because it does not allow for wave

propagation phenomena such as amplification, de-amplification, etc. to take place when the motion is transferred from bedrock to the structure.

- In both modeled cases of an arch embedded in a wall, the observed failure pattern in the field was only obtained when an extremely low stiffness value was used for the surrounding wall material, three to four orders of magnitude less than the stiffness value used for the arch elements. While this is justified for the Mamshit case, in the Nimrod case there does not seem to be such a great difference between arch and surrounding wall element-stiffness. The required softening of the surrounding wall in the numerical analysis may reflect the presence of other energy dissipation mechanisms which take place during deformation, such as block “chipping” and in-plane rotations which are not accounted for in the current version of DDA.

### 6.2.2 *Advantages*

- The DDA method was validated with respect to analytical solutions for various problems and was proven accurate. Three loading mechanisms were used: constant gravitation, time-dependant acceleration function, and time-dependant displacement function. DDA results were found to be sensitive mainly to interface friction and to the dynamic parameters of the loading function (amplitude and frequency).
- The observed structural damage to masonry structures in the field was duplicated very successfully with 2D-DDA.
- The obtained values for acceleration amplitude, although higher than expected, are within the order of 0.5 - 1g, well within reason for very strong earthquakes that destroyed the three ancient towns.

- Forward DDA modeling provides a graphical output of the deformed configuration of the original block system. This graphical output provides an over-all assessment of the structural response, found in this research to be as valuable as the quantitative measurement-point data, because it enables us to understand the evolution of structural damage with time, the relationship and interaction between adjacent blocks in the mesh, and the dominant failure mechanisms.
- A very important advantage of structural modeling with DDA is that the failure mode does not need to be assumed prior to analysis but is a product of it. This way the errors due to a wrong assumption of failure mechanism are avoided and analysis can focus on the relative significance of the various modeling variables.

### 6.3 Site – Specific conclusions:

#### 6.3.1 *Mamshit*

- Downward keystone displacement was only possible after the collapse of overlying layers, which must have caused relaxation of arching stresses.
- Most damage resulted from horizontal motions; the significance of vertical motions was negligible.
- Most of the keystone displacement took place in the first two seconds of the motion; therefore much longer runs are not necessary.
- Our best estimate for the horizontal acceleration amplitude and frequency of the motion that caused the damage in Mamshit is 0.5g, and 1 Hz respectively.

### 6.3.2 *Avdat*

- The very unique structural failure, in which mid-height blocks have been laterally displaced, is duplicated perfectly by dynamic DDA.
- The best fit set of parameters is not determined conclusively for two main reasons:
  - A finite comparison measure with a physical meaning, such as total displacement of a block for example, will not portray the failure mechanism properly.
  - Vertical accelerations were found to enhance structural response and block displacements by relief of normal stress. However, the number of combinations for a two-component loading function is infinite.

Nevertheless, two possible sets of horizontal dynamic input motions that could have generated the observed failure in the field were found: A)  $A_h = 1g, f = 3\text{Hz}$ ; B)  $A_h = 1.5g, f = 1.5\text{Hz}$ ,

### 6.3.3 *Nimrod Fortress*

- Very low wall stiffness was required to obtain the observed failure in the field with DDA. The required low wall stiffness must compensate for other failure processes that are not accounted for in the current version of DDA, such as in-plane block rotations, corner block ‘chipping’, etc.
- An extensive body of sensitivity analyses using DDA suggests that the best-fit set of dynamic parameters is:  $f = 2\text{Hz}, A = 1g$ .

#### 6.4 Pseudo-Static vs. Dynamic Analysis

Since the pseudo-static method is probably the most common approach for seismic engineering design of structures (Cai and Bathurst, 1996) it was applied, where possible, to the chosen case studies.

The pseudo-static analysis for a masonry arch presented in 2.1.4 was limited to a free-standing semi-circular arch, therefore the arch at the Nimrod-Fortress could not be analyzed, and the arch at Mamshit was analyzed assuming a free-standing arch.

The obtained threshold value for initiation of a failure mechanism at the Mamshit arch was 0.045g. This result is matched perfectly by the value obtained for the free-standing arch by DDA, 0.05g.

In the case of the masonry tower at Avdat, the pseudo-static analysis required unrealistically-high values of horizontal accelerations, 4-11g, to initiate displacement of the analyzed corner-blocks. Moreover, a pseudo-static analysis implies, by its nature, that the higher the block location in the masonry structure the 'easier' it would displace outwards under a given inertia force. This assumption was clearly contradicted by the output of the dynamic analysis, which produced the exact failure that was observed in the field, namely the outward displacement of the corner blocks at mid height. The dynamic analysis required only 1g for displacing mid-height corner blocks (while top-row blocks remained in place) in contrast to the required 4–11g by the pseudo-static approach.

The comparison between the two methods of analysis, as offered by the Avdat case, strongly suggests that a dynamic event such as an earthquake must be analyzed dynamically in order to model the evolution of structural response correctly. Furthermore, a dynamic analysis may be

possible in cases where an accurate pseudo-static analysis is not available, for example when complex failure modes such as vertical stress relief as in the tower at Avdat, take place during deformation.

The sensitivity analyses performed with DDA further demonstrate the importance of dynamic structural response, thus stressing the role of duration and frequency of motion. This is a strong proof for the partial representation of dynamic motion by the value of PGA, often used in the fields of seismic hazard assessment and engineering design.

### **6.5 Recommendations for further research**

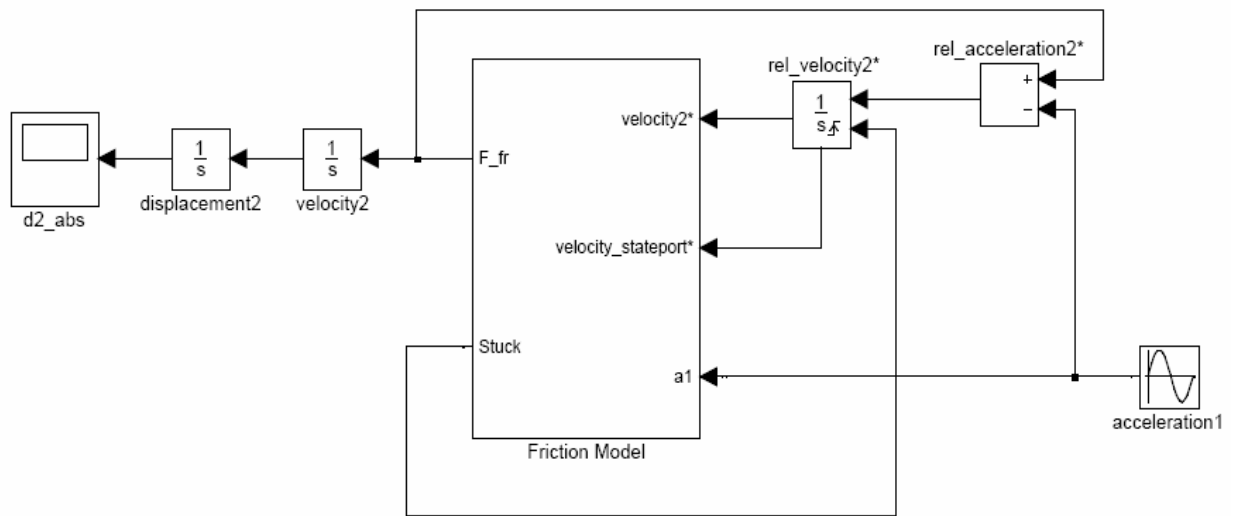
This research project represents a first attempt to derive quantitative, dynamic, paleo-earthquake parameters using back analysis of observed damage in archeological sites. Although a significant progress has been made here, inevitably some questions remain un-answered. To further investigate the structural response of a masonry structure to an earthquake, by means of DDA or any other distinct element methods, the following aspects should be examined further:

- More complex input functions should be modeled, such as a sum of sinuses or several real earthquake records.
- A Fourier analysis should be performed on the studied structures in order to find the resonant mode and determine whether the observed damage was driven by resonance.
- It would be interesting to survey the topographical site-response, at least in Nimrod, and compare PGA values again.

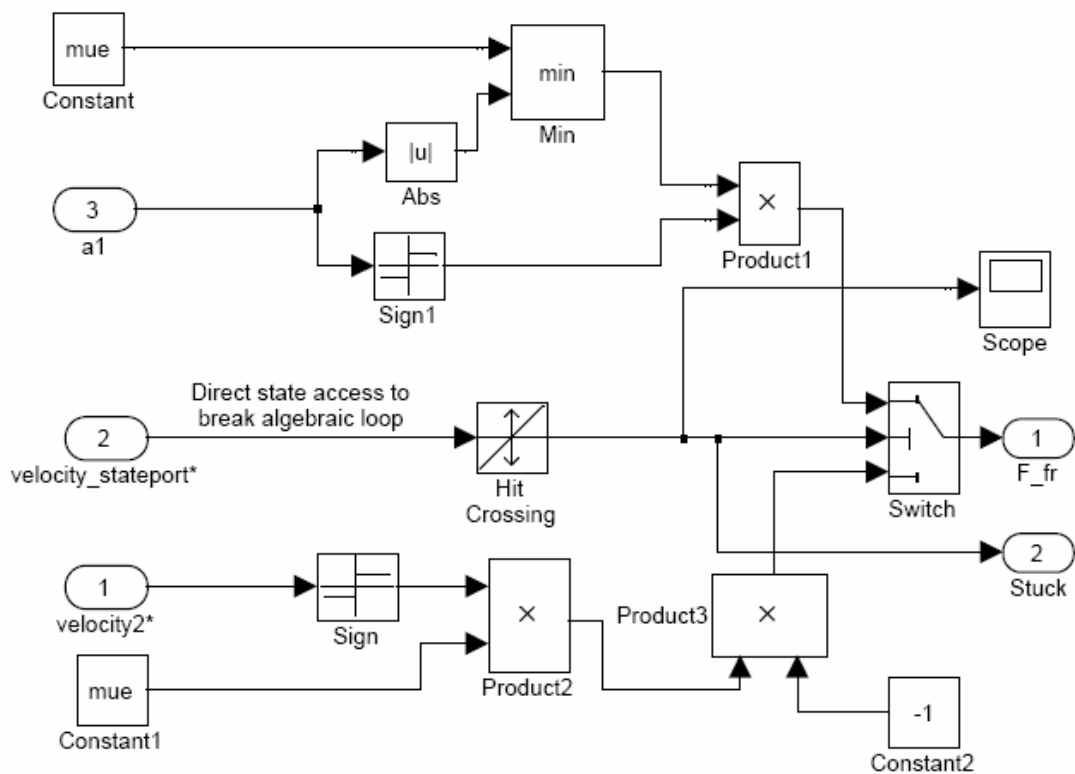
- The inadequate results of the "displacement" mode must be analyzed and researched further because in essence this is what happens in nature during shaking; the quake mode is merely an approximation.
- Ultimately this analysis should be repeated with 3D-DDA, although it is felt that for embedded arches the answers shouldn't be very different. The solution of corner stones, as attempted in Avdat, or the vault stone displacement in Nimrod which was not attempted here, certainly requires a three-dimensional formulation.

## Appendixes

### Appendix 1 – Matlab model for validation of induced displacement



A



B

Figure A.1. The Simulink model used for computation of the Matlab solution in the case of a block on a displaced block, as presented in Equation 2.17. (A) The model- the only input is a1, the output of the friction model is a2, which is double-integrated into d2 – the displacement of the upper block. (B) The sub system of the friction model.

Appendix 2.1 – Mapping of the structure at Mamshit

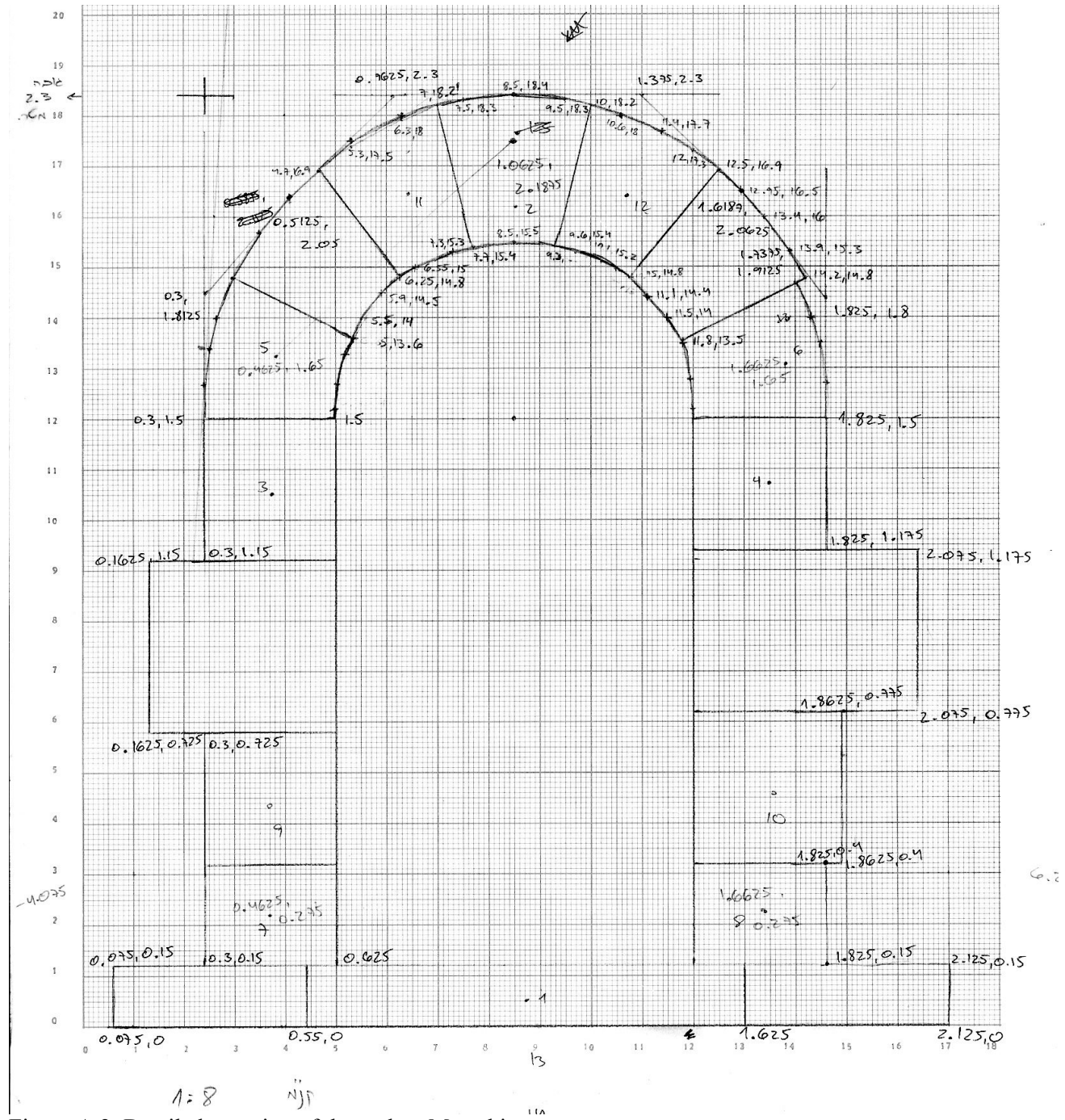


Figure A.2. Detailed mapping of the arch at Mamshit.

Appendix 2.2 – Mapping of the structure at Avdat

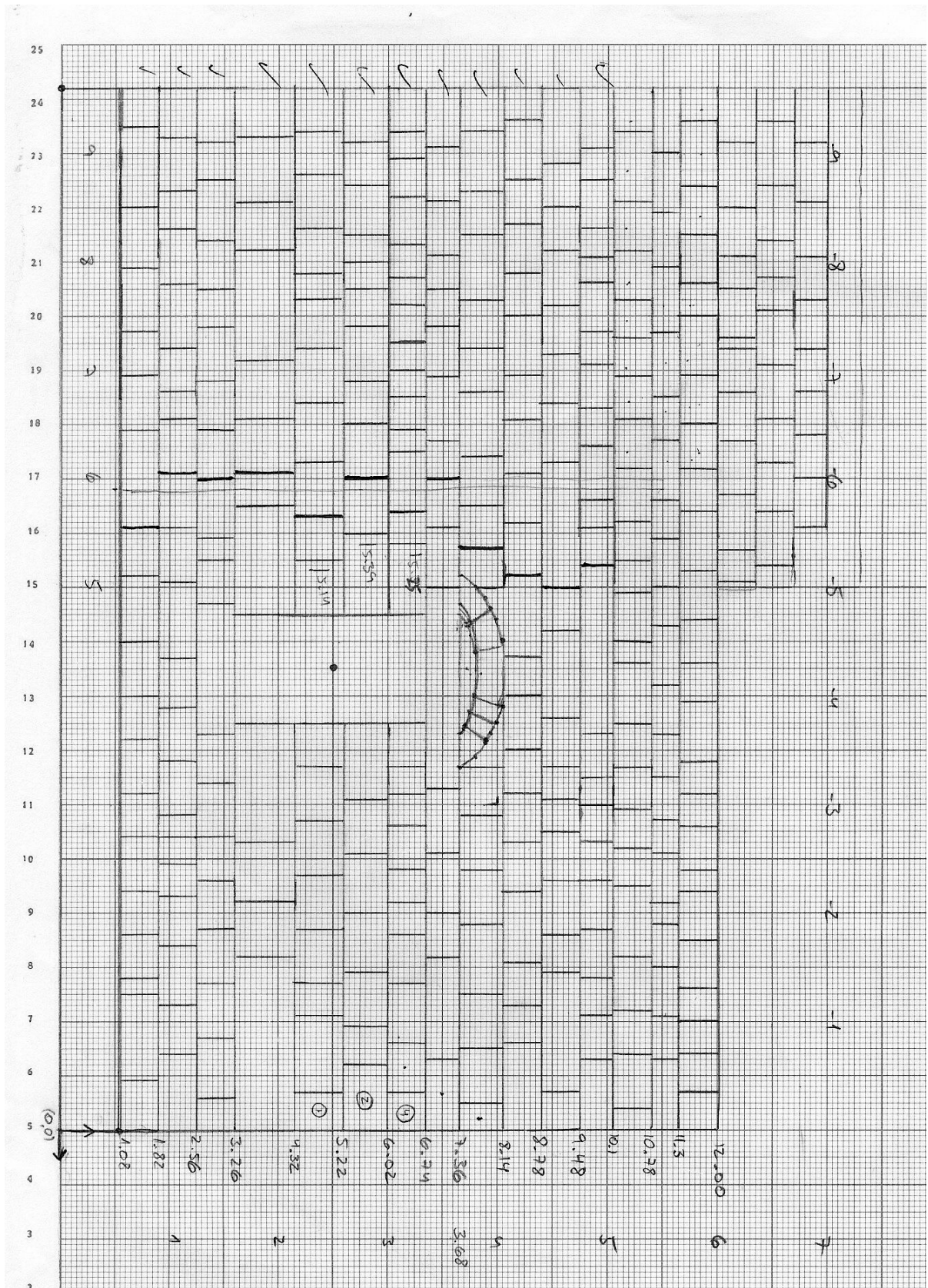


Figure A.3. Detailed mapping of the northern wall of the roman tower at Avdat.

Appendix 2.3 – Mapping of the structure at Nimrod Fortress

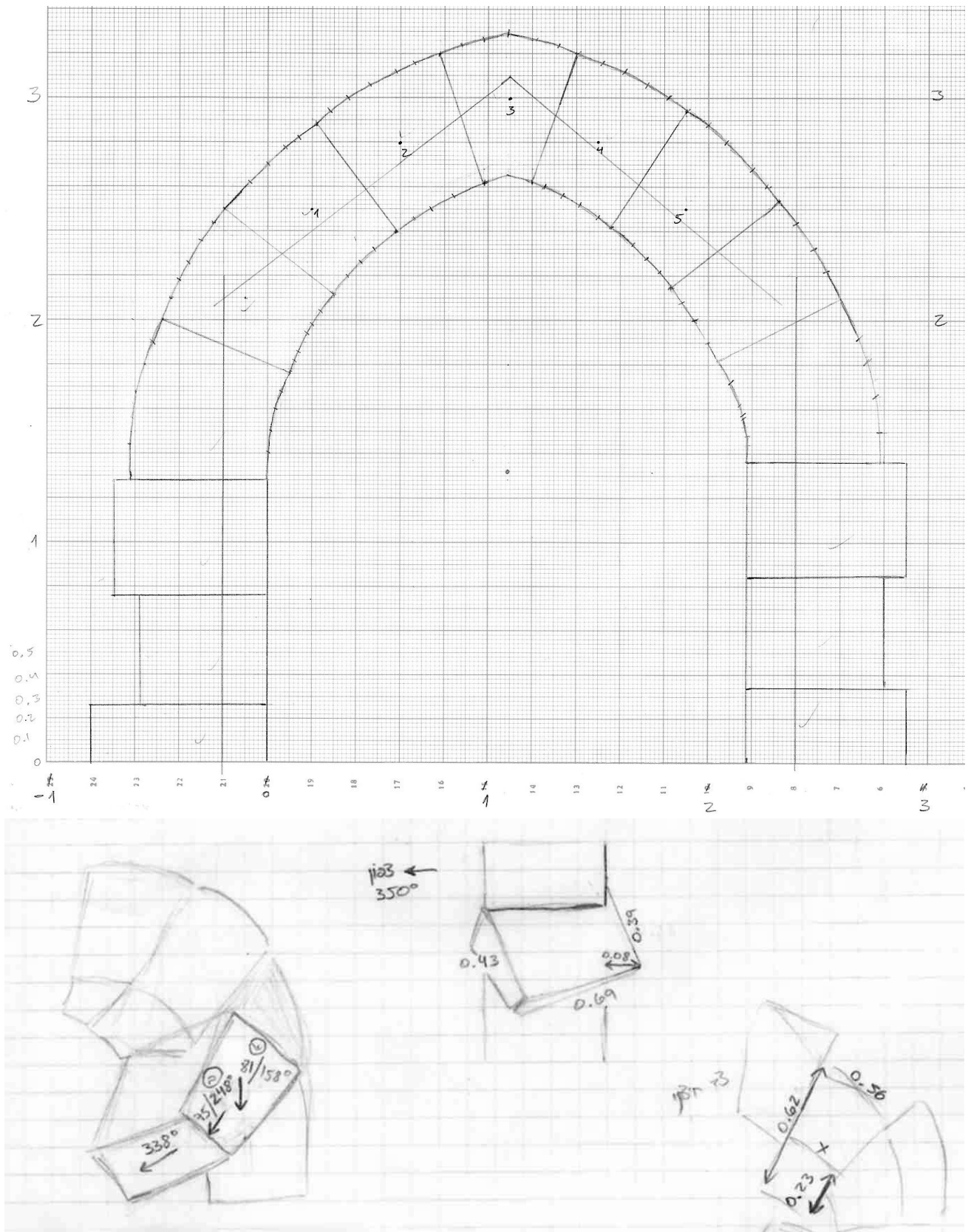


Figure A.4. Detailed mapping of the smaller outer arch at the Nimrod Fortress.

## Appendix 3.1 – DDA runs for Mamshit

data file no.	mode	blk file	$f$	A	$\phi_{wall}$	$\phi_{arch}$	$E_{wall}$	Damping	Comments
1	dis	3	1 Hz	1m	60	0	1MPa	2%	collapse
2	dis	3.5	1 Hz	1m	60	0	1MPa	2%	collapse
3	dis	3	1 Hz	0.5m	50	0	1MPa	2%	ascend and abutments collapse inside
4	dis	2.275	1 Hz	0.5m	50	0	1MPa	2%	keystone ascending
5	dis	2.275	1 Hz	0.5m	40	0	1MPa	2%	keystone descending
6	dis	3	1 Hz	0.5m	40	0	1MPa	2%	nothing happened
7	dis	2.275	1 Hz	0.5m	40	20	1MPa	2%	descend and then ascend
8	dis	2.275	1 Hz	1m	40	20	1MPa	2%	descend and then ascend
9	dis	2.275	1 Hz	0.5m	40	20	1MPa	1%	keystone ascending
10	dis	2.275	0.5 Hz	1m	40	20	1MPa	2%	nothing happened
11	dis	2.8	1 Hz	0.1	40	20	1MPa	2%	keystone ascending
12	dis	2.8	2 Hz	0.2	40	20	1MPa	2%	abutments collapse inside
13	dis	2.8	1 Hz	0.05	40	0	1MPa	2%	keystone descending
14	dis	2.82	0.7 Hz	0.1	40	35	1MPa	2%	keystone ascending
15	dis	2.82	0.5 Hz	0.1	40	35	1MPa	2%	keystone ascending
16	dis	2.82	2 Hz	0.05	40	35	1MPa	2%	keystone ascending
17	dis	2.83	1 Hz	0.15	40	35	1MPa	2%	descend and abutments collapse inside
18	dis	2.84	1 Hz	0.15	40	35	1MPa	2%	abutments distorted
19	dis	2.82	1Hz	0.08	40	35	1MPa	2%	keystone ascending
20	dis	2.83	1Hz	0.1	40	35	1MPa	2%	descend and abutments collapse inside
21	qk	2.82qk	1	0.2g	40	whole arch 0	1MPa	2%	descend 4cm
22	qk	2.8qk	1	0.2g	40	arched stones 0	1MPa	2%	descend 4.3cm
23	qk	2.82qk	1	0.32g	40	35	1MPa	2%	descend 1.7cm
24	qk	2.82qk	1	0.5g	40	35	1MPa	2%	descend 2cm

data file no.	mode	blk file	$f$	A	$\phi_{wall}$	$\phi_{arch}$	$E_{wall}$	Damping	Comments
25	qk	2.82qk	Nuweiba 15-25 sec	max0.04g	40	35	1MPa	2%	descend 7mm
26	qk	2.82qk	2	0.8g	40	35	1MPa	2%	descend 1.9cm
27	qk	2.82qk	10*Nuweiba	max 0.4g	40	35	1MPa	2%	descend 1.3cm
28	qk	2.82qk	1	0.5g	40	35	1MPa	1%	descend 3.11cm
29	qk	2.82qk	1	1g	40	35	1MPa	1%	descend 4mm
30	qk	2.82qk	15*Nuweiba	max 0.5g	40	35	1MPa	1%	descend 2.2cm
31	dis	2.82a	Dis- Nuweiba	0.05m	40	35	1MPa	2%	almost nothing happens, keystone slightly ascends
32	qk	2.82qk	0.5	0.1g	40	35	1MPa	2%	descend 9.5mm
33	qk	2.82qk	5	0.5g	40	35	1MPa	2%	descend 8mm
34	qk	2.82qk	1.5	0.5g	40	35	1MPa	2%	descend 1.9cm
35	qk	2.82qk	1.5	0.5g	40	35	1MPa	1%	descend 3cm
36	qk	2.82qk	1.5	0.5g	40	35	1MPa	0.5%	descend 2.6cm
37	qk	2.82qk	1	0.32g	40	35	1MPa	1%	descend 2.57cm
38	qk	2.82qk	5	0.5g	40	35	1MPa	1%	descend 1cm
39	qk	2.82qk	1.5	0.5g	40	35	100MPa	1%	acceded 2mm
40	qk	3qk	1.5	0.5g	40	35	1MPa	1%	descend 6mm
41	qk	2.82qk	1.5	0.5g	40	35	5MPa	1%	descend and then ascend 9.5mm
42	qk	2.82qk	1.5	2g	40	35	1MPa	1%	ascend 4.45cm
43	qk	2.82qk	0.7	0.5g	40	35	1MPa	1%	descend 3cm
44	qk	3.5 qk	1.5	0.5g	40	35	1MPa	1%	descend 6mm
45	qk	2.82qk	1	0.6g	40	35	1MPa	1%	descend 2.7cm
46	qk	2.82qk	1	0.1g	40	35	1MPa	1%	descend 1cm
47	qk	2.82qk	1	0.8g	40	35	1MPa	1%	descend 2cm
48	qk	2.82qk	2	0.5g	40	35	1MPa	1%	descend 2.7cm
49	qk	2.82qk	0.5	0.5g	40	35	1MPa	1%	descend 2cm
50	qk	2.82qk	10	0.5g	40	35	1MPa	1%	descend 1cm
51	qk	2.82qk	1.5	0.5g	40	35	1MPa	0%	collapse

blk file	description
2.275	height 2.275m, arch friction angle only to arched stones
3	height 3m, arch friction angle only to arched stones
2.8	height 2.275m, third block gone
2.82	like 2.8, arch friction angle to whole arch
2.83	upper beam added
2.84	block between arch abutments
2.82a	no basement block - vertical displacements

## Appendix 3.2 – DDA runs for Avdat

data file no.	mode	blck file	$f$	A	$A_{\text{vertical}}$	Comments
1	qk	blck1	15nueiba	0.6g	0	the arch is released, left wall opens
2	qk	blckwo	0	0g	0	no displacements - the structure is stable without the 3 blocks
3	qk	blck1	1	1g	0	total destruction-starts from left
4	qk	blck1	5	1.5g	0	left collapses, right- only some openings
5	qk	blck1	1	0.5g	0	second floor collapses, upper right corner-openings
6	qk	blck2	1	0.5g	0	Almost stable. Only second floor is destroyed
7	qk	blck3	1	0.5g	0	no deformations
8	dis	blck11	1	0.125m	0	Doesn't finish. $t=3.67\text{sec}$ . $g_2=0.0005$ , 2.32 Iterations/time step
9	dis	blck31	1	0.125m	0	Doesn't finish. $t=3.67\text{sec}$ . $g_2=0.0005$ , 2.26 Iterations/time step
8.1	dis	blck11	1	0.125m	0	$g_2=0.001$ , $I=3.17$
9.1	dis	blck31	1	0.125m	0	$g_2=0.0008$ , $I=2.87$
8.3	dis	blck11	1	0.125m	0	fail
10	dis	blck32	1	0.125m	0	??
11	qk	blck1	2	0.7g	0	left side opens, rows displaced into doorway
12	qk	blck2	2	0.7g	0	not much
13	qk	blck3	2	0.7g	0	block rows enter doorway on both sides
14	qk	blck1	1	0.8g	0	too strong, collapse
15	qk	blck4	1	0.6g	0	step failure on both sides
16	qk	blck4	2	0.7g	0	interesting - openings in doorway level
17	qk	blck4	5	1.5g	0	Excellent! - one block is pulled out on left
18	qk	blck4	5	0.5g	0	almost nothing
19	qk	blck1	1	0.8g	0	too strong, collapse
20	qk	blck4	5	-1.5g	0	Like 17, stronger, not opposite.
21	qk	blck4	5	1g	0	like 17, more subtle
20.1	qk	blck4*	5	-1.5g	0	Strong openings on both sides. No preference to right
20.2	qk	blck4*	5	-1.5g	0	2 sec. from doorway base- 7 rows on left and 3 on right
22	qk	blck4*	5	1.5g	0.5	the whole mesh is displaced to the right
23	qk	blck4*	5	1.5g	0.2	openings on both sides
24	qk	blck4*	5	1g	0.5	bulge shape on right, steps from top to bottom
25	qk	blck4*	5	1g	0.2	Openings on left. Blocks 0 and 4 are pulled out
26	qk	blck4*	3	1g	0.5	bulge shape, more on left
27	qk	blck4*	3	1g	0.2	similar but milder
28	qk	blck5	5	1.5g	0	Excellent! - up to 20cm displacements
29	qk	blck5	1	0.6g	0	too strong, the whole structures shakes
30	qk	blck5	2	0.7g	0	almost nothing
31	qk	blck5	1	0.5g	0	not much
32	qk	blck5	5	1g	0	3-5 cm displacements. Also on left
33	qk	blck5	3	1g	0	Excellent. 4-10 cm.

<b>data file no.</b>	<b>mode</b>	<b>blk file</b>	<b><i>f</i></b>	<b>A</b>	<b>A<sub>vertical</sub></b>	<b>Comments</b>
34	qk	blk5	2	1g	0	too strong
35	qk	blk5	2	0.8g	0	alittle too strong, better than 34
36	qk	blk5	2.5	1g	0	not bad, blocks are displaced
37	qk	blk5	5	0.8g	0	almost no displacement, only upper left corner

<b>blk</b>	<b>description</b>
1	northern wall
wo	without the three analyzed blocks
2	fixed line 1m left of doorway, where later structure begins
3	part of the left side is one big block (where the later structure is)
11	like blk1, displacement mode
31	like blk3, displacement mode
32	like blk31, some of the blocks of lower row are connected to foundation block as spikes
4	the arch is one block and so are the doorway abutments to avoid blocks sliding in
4*	left side has bigger blocks
5	final model- confining wall on left

## Appendix 3.3 – DDA runs for Nimrod Fortress

blk	data	Amplitude	frequency	E <sub>1</sub>	E <sub>2</sub>	f	Time (sec)	damping	result
1	1	1	1	54GPa	54GPa	35	10	1%	keystone ascends a little, the rest descend, like steps
2	2	1	1	54GPa	54GPa	35	10	1%	the same
3	3	1	1	54GPa	54 Mpa	35	10	1%	very similar, keystone ascends
4	4	1	1	54GPa	54 Mpa	35	10	1%	same, right side a little more than left
3	5	1	1	54GPa	5.4 Mpa	35	10	1%	Ar displaced more than others, keystone ascends
4	6	1	1	54GPa	5.4 Mpa	35	10	1%	like 5
3	7	-1-0.2	1	54GPa	5.4 Mpa	35	10	1%	not bad. The whole left side slides to left, blocks Ar and Br pulled out
4	8	-1-0.2	1	54GPa	5.4 Mpa	35	10	1%	similar, less displacements
3	9	1-0.5	3	54GPa	5.4 Mpa	35	10	1%	too much to the left, everything deforms
4	10	1-0.5	3	54GPa	5.4 Mpa	35	10	1%	not good. Wall drawn away from fixation, no need.
3	11	1-0.5	1	54GPa	5.4 Mpa	20	10	1%	collapse left, too strong
3	12	1-0.5	1	54GPa	54 Mpa	20	10	1%	collapse left, too strong
3	13	-1.5-0.5	1.5	54GPa	5.4 Mpa	20	10	1%	not bad, too much to the left, but Ar and Br pulled out
3	14	-1.5-0.5	1.5	54GPa	54 Mpa	20	10	1%	keystone ascends, right side displaced in steps
3	15	-1-0.2	3	54GPa	5.4 Mpa	20	10	1%	Quite mild, Ar begins displacement.
3	16	-1-0.2	3	54GPa	54 Mpa	20	10	1%	not bad, keystone ascends, Al, Ar and Br pulled out
1	17	-0.8-0.2	1.5	54GPa	54GPa	20	10	1%	Not good. keystone ascends
3	18	-0.8-0.2	1.5	54GPa	5.4 Mpa	20	10	1%	Much better. Only right side pulled out
3	19	-0.8-0.2	1.5	54GPa	54 Mpa	20	10	1%	like 18 but Bl also displaced
3	20	-0.8-0.2	1.5	54GPa	5.4 Mpa	20	20	1%	not bad
5	21	-0.8-0.2	1.5	54GPa	54 Mpa	20	10	1%	not much
5	22	-0.8-0.2	1.5	54GPa	5.4 Mpa	20	10	1%	like 22, but keystone starts to descend
5	23	-1-0.2	1	54GPa	5.4 Mpa	20	10	1%	Not much, but Ar leads.
6	24	1	1	54GPa	5.4 Mpa	35	10	1%	Ar begins to pull out
6	25	1	5	54GPa	5.4 M	35	10	1%	nothing, runs only 9sec

blk	data	Amplitude	frequency	E <sub>1</sub>	E <sub>2</sub>	f	Time (sec)	damping	result
6	26	1.5	1	54GPa	5.4 Mpa	35	10	1%	Ar and Al displaced. Too symmetrical
6	27	1	1	54GPa	5.4 Mpa	35	20	1%	A little better. Al also displaced but less
7	28	1	1	54GPa	5.4 Mpa	35	10	1%	too symmetrical, keystone almost doesn't move
6	29	1	1.5	54GPa	5.4 Mpa	35	10	1%	Ar more than Al
6	30	1.5	1.5	54GPa	5.4 Mpa	35	10	1%	too symmetrical
7	31	1	3	54GPa	5.4 Mpa	35	10	1%	very little displacements
7	32	1.5	3	54GPa	5.4 Mpa	35	10	1%	too symmetrical - more than 31
6	33	1.5	3	54GPa	5.4 Mpa	35	10	1%	a little better, Al still displaced
6	34	1	1	54GPa	5.4 Mpa	35	40	1%	Excellent! Ar more than others. Too many structural deformations
6	35	1	3	54GPa	5.4 Mpa	35	40	1%	Very good. Like 34, more mild
6	36	1	2	54GPa	5.4 Mpa	35	40	1%	The best!
6	37	1	2	54GPa	5.4 Mpa	35	40	1%	all of the arch blocks move a little
6	38	0.8	2	54GPa	5.4 Mpa	35	40	1%	very little happening
6	39	1.5	2	54GPa	5.4 Mpa	35	40	1%	too many displacements
6	40	1.5	2	54GPa	5.4 Mpa	35	40	1%	the whole arch slides inwards

blk	description
1	regular, hight 3.28m
2	with fixed line on right side, smaller width
3	different material, 1
4	different material, 2
5	like 3, with two rows of blocks above arch 4.1m
6	like 5, with log on right
7	like 3, with log on right

## References

- Ambraseys, N. N. and Barazangi, M. (1989). The 1759 Earthquake in the Bekka Valley: Implications for Earthquake Hazard Assessment in the Eastern Mediterranean Region. *J. Geophys. Res.*, 94(B4), 4007-4013.
- Ambraseys, N. N. and Jackson, J. A. (1998). Faulting associated with historical and recent earthquakes in the Eastern Mediterranean region. *Geophysical Journal International*, 133(2), 390-406.
- Amiran, D., Arieh, E. and Turcotte, T. (1994). Earthquakes in Israel and Adjacent Areas: Macroseismic Observations since 100 B.C.E. *Isr. Explor. J.*, 44(3-4), 260-305.
- Anderson, J. G., Brune, J. N., Anooshehpour, R. and Ni, S. D. (2000). New ground motion data and concepts in seismic hazard analysis. *Current Sci.*, 79(9), 1278-1290.
- Anooshehpour, A. and Brune, J. N. (2002). Verification of precarious rock methodology using shake table tests of rock models. *Soil Dyn. Earthquake Eng.*, 22(9-12), 917-922.
- Arieh, E. and Rabinowitz, N. (1989). Probabilistic assessment of earthquake hazard in Israel. *Tectonophysics*, 167, 223-233.
- Avni, R., Bowman, D. and Nur, A. (2002). Erroneous interpretation of historical documents related to the epicenter of the 1927 Jericho earthquake in the Holy Land. *J. Seism.*, 6, 469-476.
- Ben-Menahem, A. (1991). Four thousand years of seismicity along the dead sea rift. *J. Geophys. Res.*, 96(B12), 20,195-20,216.
- Bicanic, N., Stirling, C. and Pearce, C. J. (2003). Discontinuous modelling of masonry bridges. *Computational Mechanics*, 31(1 - 2), 60-68.
- Blasi, C. and Foraboschi, P. (1994). Analytical approach to Collapse Mechanisms of Circular Masonry Arch. *J. Struct. Eng.*, 120(8), 2288-2309.
- Boore, D. M., Joyner, W. B. and Fumal, T. E. (1997). Equations for estimating horizontal response spectra and peak acceleration from western North American earthquakes: A summary of recent work. *Seis. Res. Lett.*, 68, 127-153.
- Boothby, T. E. (1996). Analytical approach to collapse mechanisms of circular masonry arch, Discussion. *J. Struct. Eng. ASCE*, 122(8), 978-980.
- Boothby, T. E., Domalik, D. E. and Dalal, V. A. (1998). Service load response of masonry arch bridges. *J. Struct. Eng. ASCE*, 124(1), 17-23.
- Brune, J. N. (2002). Precarious-rock constraints on ground motion from historic and recent earthquakes in southern California. *Bull. Seismol. Soc. Am*, 92(7), 2602-2611.
- Cai, Z. and Bathurst, R. J. (1996). Deterministic sliding block methods for estimating seismic displacement of earth structures. *Soil Dyn. Earthquake Eng.*, 15(255-268).
- Clemente, P. (1998). Introduction to dynamics of stone arches. *Earthquake Eng. Struct. Dyn.*, 27, 513-522.
- De Luca, A., Giordano, A. and Mele, E. (2004). A simplified procedure for assessing the seismic capacity of masonry arches. *Engineering Structures*, 26(13), 1915-1929.
- Ellenblum, R. (1989). Who Built Qalat Al-Subayba? *Dumbarton Oaks Papers*, 41, 103-112.
- Ellenblum, R., Marco, S., Agnon, A., Rockwell, T. and Boas, A. (1998). Crusader castle torn apart by earthquake at dawn, 20 May, 1202. *Geology*, 26(4), 303-306.
- Enzel, Y., Kadan, G. and Eyal, Y. (2000). Holocene Earthquakes Inferred from a Fan-Delta Sequence in the Dead Sea Graben. *Quat. Res.*, 53, 34-48.
- Fabian, P. (1998). Evidence of earthquake destruction in the archaeological record - the case of ancient Avedat. *IGS Ann. Meeting*, Mizpe Ramon.
- Galli, P. and Galadini, F. (2001). Surface faulting of archaeological relics. A review of case histories from the Dead Sea to the Alps. *Tectonophysics*, 335(3-4), 291-312.

- Goodman, R. E. and Seed, H. B. (1966). Earthquake-induced displacements in sand embankments. *J. Soil Mech. Foundation Div, ASCE*, 90(SM2), 125-146.
- Hall, J. K. (1994). Digital shaded-relief map of Israel and environs 1:500,000, I. G. Survey.
- Hanks, T. C. and Kanamori, H. (1979). A Moment Magnitude Scale. *journal of geophysical research*, 84(2348-2350).
- Hartal, M. (2001). The Al-Subayba (Nimrod) Fortress , towers 11 and 9. *11*, Israel Antiquities Authority, Jerusalem
- Hatzor, Y. H. and Feintuch, A. (2001). The validity of dynamic block displacement prediction using DDA. *Int. J. Rock Mech. Min. Sci.*, 38, 599-606.
- Hatzor, Y. H., Arzi, A. A., Zaslavsky, Y. and Shapira, A. (2004). Dynamic stability analysis of jointed rock slopes using the DDA method: King Herod's Palace, Masada, Israel. *Int. J. Rock Mech. Min. Sci.*, (in press).
- Heyman, J. (1982). *The Masonry Arch*, Ellis Horwood Limited, Chichester
- Israel Building Code #413. (1998). Design provisions for earthquake resistance of structures. The Standards Institution of Israel.
- ISRM. (1978). suggested methods for determining sound velocity. *Int. J. Rock Mech. Min. Sci. & Geomech. Abstr.*, 15, 53-58.
- ISRM. (1985). suggested method for determining point load strength. *Int. J. Rock Mech. Min. Sci.*, 22, 53-60.
- Jaeger, J. C. and Cook, N. G. W. (1979). *Fundamentals of rock mechanics*, Chapman and Hall Ltd.
- Jing, L. (2003). A review of techniques, advances and outstanding issues in numerical modelling for rock mechanics and rock engineering. *Int. J. Rock Mech. Min. Sci.*, 40, 283-353.
- Kagan, E. J., Bar-Matthews, M., Ayalon, A. and Agnon, A. (2002). A wiggle-matching technique applied to the dating of damaged cave deposits and compilation of a longterm paleoseismic record, Soreq Cave, Israel. *Geochimica et Cosmochimica Acta*, 66(15A), A377-A377 Suppl.1.
- Ken-Tor, R., Agnon, A., Enzel, Y., Stein, M., Marco, S. and Negendank, J. F. W. (2001). High-resolution geological record of historic earthquakes in the Dead Sea basin. *J. Geophys. Res.*, 106(B2), 2221-2234.
- MacLaughlin, M. M. and Doolin, D. M. (2005). Review of validation of the Discontinuous Deformation Analysis (DDA) method. *Int. J. Numer. Anal. Meth. Geomech.*, 29.
- Marco, S., Stein, M., Agnon, A. and Ron, H. (1996). Long-term earthquake clustering: A 50,000 year paleoseismic record in the Dead Sea Graben. *J. Geophys. Res.*, 101(B3), 6179-6191.
- Marco, S., Rockwell, T., Heimann, A., Agnon, A. and Ellenblum, R. (2000). Historical earthquake deformation revealed by 3D trenching on Dead Sea Transform. *HOKUDAN International Symposium and School on Active Faulting*, 261-263.
- Marco, S., Hartal, M., Hazan, N., Lev, L. and Stein, M. (2003). Archaeology, history, and geology of the A.D. 749 earthquake, Dead Sea transform. *Geology*, 31(8), 665-668.
- Marco, S., Rockwell, T. K., Heimann, A., Frieslander, U. and Agnon, A. (2005). Late Holocene activity of the Dead Sea Transform revealed in 3D palaeoseismic trenches on the Jordan Gorge segment. *Earth and Planetary Science Letters*, 234(1-2), 189-205.
- Mazor, E. and Korjenkov, A. (2001). Applied Archeoseismology. In E. Mazor and B. Krasnov ed., The Makhteshim Country Laboratory of Nature, Pensoft, Moscow, 123-136.
- Migowski, C., Agnon, A., Bookman, R., Negendank, J. and Stein, M. (2004). Recurrence pattern of Holocene earthquakes along the Dead Sea transform revealed by varve-counting and radiocarbon dating of lacustrine sediments. *Earth Plan. Sci. Lett.*, 222(1), 301-314.
- Negev, A. (1988a). The Architecture of Mamphis. 26, The Hebrew University of Jerusalem, Jerusalem
- Negev, A. (1988b). The Nabatean cities in the Negev. 62-63.(in hebrew).
- Negev, A. (1997). The Architecture of Oboda. 36, The Hebrew University of Jerusalem, Jerusalem

- Newmark, N. (1965). Effects of earthquakes on dams and embankments. *Geotechnique*, 15(2), 139-160.
- Purcaru, G. and Berckhemer, H. (1978). A magnitude scale for very large earthquakes. *Tectonophysics*, 49, 189-198.
- Shapira, A. (1983). Potential earthquake risk estimation by application of a simulation process. *Tectonophysics*, 95, 75-89.
- Shapira, A. and Fernandez, L. M. (1989). Probabilities of exceedance for prescribed peak ground accelerations (PGA) at selected southern african locations. *Tectonophysics*, 167, 253-260.
- Shapira, A. (2002). Explanations to the PGA map for the Israeli buiding code 413 <http://www.gii.co.il/>.(in hebrew).
- Shi, G.-h. and Goodman, R. E. (1989). The key blocks of unrolled joint traces in developed maps of tunnel walls. *Int. J. Numer. Anal. Meth. Geomech.*, 13, 131-158.
- Shi, G.-H. (1993). *Block System Modeling by Discontinuous Deformation Analysis*, Computational Mechanics Publication, Southhampton, UK
- Shi, G.-h. (1999). Applications of Discontinuous Deformation Analysis and Manifold method. *Third International Conference on Analysis of Discontinuous Deformation*, Vail, Colorado, 3-16.
- Sieberg, A. (1932). Erbebengeographie. In Band ed., *Handbuch der Geophysik*, Borntraeger, Berlin, 527-1005.
- Sinopoli, A., Corradi, M. and Foce, F. (1997). Modern formulation for preelastic theories on masonry arches. *J. Engrg. Mech, ASCE*, 123(3), 204.
- Tsesarsky, M., Hatzor, Y. H. and Sitar, N. (2005). Dynamic displacement of a block on an inclined plane: Analytical, experimental and DDA results. Technical note. *Rock Mechanics and Rock Emgineering*, 38(2), 153-167.
- Vilnay, O. and Cheung, S.-S. (1986). Stability of Masonry Arches. *J. Struct. Eng, ASCE*, 112(10), 2185-2199.
- Vilnay, O. (1988). Dynamic behavior of three-voussoir arch. *J. Struct. Eng, ASCE*, 114(5), 1173-1186.
- Young, R. M.-C. (1996). *Discontinuous Deformation Analysis Programs, version 96, User's manual*.
- Zaslavsky, Y. and Shapira, A. (2000). Experimental study of topographic amplification using the Israel seismic network. *Jouranl of Earthquake Engineering*, 4(1), 43-65.
- Zilberman, E., Amit, R., Heimann, A. and Porat, N. (2000). Changes in Holocene PAleoseismic activity in the Hula pull-apart basin, Dead Sea Rift, northern Israel. *Tectonophysics*, 321, 237-252.